Development of a cutter ladder vibration model

Supervisors
Prof. Dr. A. Metrikine
Dr. Ir. J.M. de Oliveira Barbosa
Ir. G. Grundlehner
Dr. E. Lourens

Author
Thijmen P. Bartstra

Royal Boskalis Westminster N.V

Delft University of Technology
Faculty of Civil Engineering and Geosciences
Master Offshore and Dredging Engineering

July 1, 2016

Abstract

Structural vibrations are a known cause of damage to offshore structures and equipment. A Cutter Suction Dredger (CSD) is a dredge vessel known to vibrate heavily during operation. Primary cause of these vibrations is the cutting process, performed to cut and excavate soil from the seabed. A component prone to damage is the cutter ladder, a component of the CSD used to position the cutter head at the seabed. Cutter ladders are known to suffer from failures including large cracks in the structural members, of which the cause is sometimes unclear.

Current methods for developing a cutter ladder involve detailed quasi-static finite element modeling for strength analysis and sometimes modal analysis to identify natural frequencies and mode shapes. Structural vibrations due to dynamic loading are usually not taken into account. In 2015 Boskalis performed extensive vibration measurements on its Taurus II CSD, hereby setting the stage for research into the dynamics of cutter ladders. By taking a closer look at dynamics of the cutter ladder, a cause for structural damage might be identified. This thesis therefore aims to investigate the vibrations of a cutter ladder as a possible cause for damage.

In order to obtain knowledge about the dynamic behavior of the cutter ladder in operation, data obtained during the vibration measurements were investigated using operational modal analysis. This investigation gave further insight in how to approach the development and validation of a vibration model. A vibration model using finite beam elements was developed to take a closer look at the characteristics of the cutter ladder structure. This vibration model was obtained through simplification of a detailed plate-element model, which was developed in an earlier project. The dynamic characteristics of the obtained vibration model where validated to the detailed plate element model by comparison of modal analysis results. It was chosen to update the vibration model using the measurements obtained on the cutter ladder, as it was hereby possible to investigate the influence of dynamic parameters on which uncertainties exist, such as the water added mass surrounding the structure, the damping and the stiffness parameters at the boundary conditions. Use was made of the transmissibility of vibrations between the locations where measurements were obtained. Measured transmissibility was compared to modeled transmissibility, as in this manner it was possible to look into dynamic behavior of the cutter ladder, apart from the external loading. The model was updated by varying various dynamic parameters on which uncertainties existed, including water added mass, damping and stiffness parameters at the boundary conditions.

Investigating the data obtained during measurements showed that the forced vibrations caused by the cutting process dominate the dynamic behavior in the cutter ladder. Natural vibrations of the cutter ladder were found to be minor. Updating the model revealed that the water surrounding the structure has a significant influence on the dynamic behavior. In vertical direction, a quantity of water close to the weight of the cutter ladder itself had to be added to have the vibration model meet the design parameters. Quite an amount of structural damping had to be added too, for which the cause is again sought for in the water surrounding the structure. Using transmissibility functions as design parameters was found to yield accurate results, especially at the sections

where no external loading was introduced.
It is recommended to continue investigating the influence of the forced vibrations on the fatigue life of the cutter ladder on a more local scale, as this might provide new insights for future cutter ladder designs.

Acknowledgements

This project has been assigned for by the R & D department of Royal Boskalis Westminster N.V. to investigate vibrations occurring in a cutter ladder in operation. The methods and results presented in this thesis are used to graduate for the MSc. degree in Offshore and Dredging Engineering at the TU Delft.

Prior to my graduation, I already took part in multiple projects which involved the development of mechanical systems for offshore environments. Though, non of them involved investigating the actual behavior of machinery in their working environment. The large quantity of available information, models and measurements on an existing structure, gave in my opinion a good opportunity to gain knowledge and valuable experience for my future career. The large amount of factors to be taken into account and the complexity of the physics behind the modeling, made this a challenging project from beginning till end.

This project of course could not have come about without the support of few people, whom I like to thank for that. Many thanks to my supervisors from Boskalis, Gertjan Grundlehner, Roeland Neelissen and Chris van den Berg who supported me through the project, supplied me with their knowledge and insight, and told me not to complicate my life too much for myself. Rik Kesteloo and Willem Janse from Vuyk Engineering B.V. who were so kind to let me use their finite element model and gave technical support with it. My supervisors from the TU Delft, Joao De Oliviera Barbosa, Eliz-Mari Lourens and Andrej Metrikine, I enjoyed the constructive meetings we had. Many thanks to all my fellow students at Boskalis for our shared times and sorrow, I wish them all the best with their own graduation.

Last I would like to thank my family and friends for being supportive through all my years of studying.

Thijmen

Contents

List of Figures

List of Tables

Nomenclature

$\dot{\varphi}_c$	Rotational speed cutter head	$[RPM]$
ϵ	Error function	$[-]$
$\mathbf{\Omega}$	Eigen frequency matrix	$[{}^{rad}/_{s}]$
$\mathbf{\Phi}$	mode shape vector matrix	$[-]$
$\mathbf{C}$	Vibration model damping matrix	$[{}^{Ns}/_{m}]$
$\mathbf{d}_m(\omega)$	Frequency domain column vector	$[Hz]$
$\mathbf{d}_m(t)$	Time domain column vector	$[s]$
$\mathbf{H}_{ME}(\omega)$	Measured transmissibility function	$[-]$
$\mathbf{H}_{MO}(\omega)$	Modeled transmissibility function	$[-]$
$\mathbf{K}$	Vibration model stiffness matrix	$[{}^{N}/_{m}]$
$\mathbf{M}$	Vibration model mass matrix	$[kg]$
$\mathbf{P}(\omega)^{[1]}$	Power spectral density matrix containing multiple frequency domain vectors superscript number between brackets indicates the used dataset.	$[Hz]$
$\mathbf{Q}(\omega)_n^{[1]}$	Outer product matrix of index n	$[Hz]$
$\mathbf{S}(\omega)_n^{[1]}$	Spectral density matrix of index n	$[Hz]$
$\mathbf{T_a}(\omega)$	frequency dependent transfer matrix	
$\mathbf{T}(t)^{[1]}$	Time domain matrix containing multiple time domain column vectors, superscript number between brackets indicates the used dataset.	$[s]$
ρ_s	Steel density	$[{}^{kg}/_{m^3}]$
ρ_w	Water density	$[{}^{kg}/_{m^3}]$
Σ	Singular value matrix	$[Hz]$
ξ	Damping factor	$[-]$
A_m	Mass corrected cross sectional area	$[m^2]$
A_w	Cross sectional area wires	$[m^2]$

A_{MH}	Cross sectional area main hinge beams	$[m^2]$
A_m	Mass corrected cross sectional area	$[m^2]$
E	Youngs' modulus	$[{}^{N}/{}_{m^2}]$
E_w	Youngs' modulus wires	$[{}^{N}/{}_{m^2}]$
F	General load used in multiple occasions	$[N]$
f_b	Blade frequency	$[Hz]$
f_s	Sample frequency	$[Hz]$
G	Shear modulus.	$[{}^{N}/{}_{m^2}]$
I_c	Mass moment of inertia of the components	$[kgm^2]$
I_y	Area moment of inertia around y-direction	$[m^4]$
I_z	Area moment of inertia around z-direction	$[m^4]$
$I_{y,MH}$	Area moment of inertia around the z-axis of the main hinge beams	$[m^4]$
$I_{z,MH}$	Area moment of inertia around the z-axis of the main hinge beams	$[m^4]$
J	Rotational stiffness constant	$[m^4]$
$k_{\psi 1}$	Rotational stiffness around z-axis of node 1	$[{}^{Nm}/{}_{rad}]$
k_{hw}	Hoist wire stiffness	$[{}^{N}/{}_{m}]$
k_{sw}	Swing wire stiffness	$[{}^{N}/{}_{m}]$
k_{y1}	Horizontal stiffness at node 1	$[{}^{N}/{}_{m}]$
k_{z1}	Vertical stiffness at node 1	$[{}^{N}/{}_{m}]$
L_s	Model section length	$[m]$
L_{CL}	Cutter ladder length	$[m]$
L_{MH}	Main hinge beam length	$[m]$
m	Matrix column-index used in various designations.	$[-]$
M_s	Mass steelwork	$[mT]$
$M_{s,c,wi}$	Combined mass of steelwork, components, and internal water added mass	$[mT]$
$M_{we,y}$	External water added mass in horizontal direction	$[mT]$
$M_{we,y}$	External water added mass in vertical direction	$[mT]$
M_{wi}	Internal water added mass	$[mT]$
N	Sample length Fourier transform	$[-]$
n	Matrix row-index used in various designations	$[-]$

N_b	Number of blades on a cutter head	$[-]$
T_s	Sample period	$[s]$
u_b	Generalized beam bending deflection	$[{}^{m}/{}_{N}]$
u_d, y, z	Generalized beam deflection in both vertical and horizontal direction	$[m]$
u_s	Generalized beam shear deflection	$[{}^{m}/{}_{N}]$
v_s	CSD swing speed	$[{}^{m}/{}_{min}]$

Part I

Thesis report

Chapter 1

Introduction

As a large dredging company, Royal Boskalis owns a big fleet of Cutter Suction Dredgers (CSDs), which are used all over the world. One of the critical parts in a CSD is the cutter ladder, used to position the cutter head at the seabed where material is dredged. A cutter ladder is a large structural member which comprises of various components critical to the dredge process, including a dredge pump and the full cutter head drive and power train.

Operating these cutter suction dredgers, Royal Boskalis faces the challenge of finding a balance between obtaining the highest possible production and prevent damage of equipment due to overloading. Cutter ladders are known to suffer from failures, including large cracks in the structural members of which the cause sometimes is unclear. In appendix D, pictures are given of the cracks found on the cutter ladder. Design and verification of the cutter ladder strength in the design phase is currently performed using FEM modeling in a quasi-static manner, in which maximum dynamic loads are applied statically. Resonance of the structure at natural frequencies is currently not taken into account in cutter ladder designs. Royal Boskalis is therefore interested whether dynamic behavior could be identified as a cause for the structural damage.

1.1 Problem definition

An identification of the available literature and models is performed during the start up phase of this project, a short outline is given.

A vibration study is performed on the CSD Taurus II in operation at the "Base Project" in Qatar. The "The Base" location was of interest for vibration measurements due to its challenging character, extremely hard material had to be processed. Measurements using acceleration sensors were performed all over the CSD, including the cutter ladder. Thirteen accelerometers were mounted on the cutter ladder skin and a torque sensor was mounted on the cutter shaft. Data from measurements taken during operating the CSD is made available for this project, as well as the reporting on the measurements which can be found in [3] and [22].

Simultaneously to this thesis project, Royal Boskalis was in the process of analyzing the structural strength of the cutter ladder to possibly identify a cause for the structural damage. A very detailed finite plate-element model of the cutter ladder has therefore been developed in collaboration with Vuyk Engineering B.V. This model was found to be too detailed for use in a dynamic analysis, but is still used for obtaining dimensions, stiffness and mass parameters of the cutter ladder. The plate-element model is also used for performing modal analysis in dry-conditions of which use is made in chapter 4.

As dynamic behavior of the cutter ladder is not accounted for in the finite plate-element model, it is proposed to develop a vibration model to predict vibrations, which can be used to investigate dynamic aspects of the cutter ladder such as the influence of the water on the added mass and damping of the cutter ladder. A validation of the vibration model could be performed using the data from the measurements. The model could eventually be used as an input for fatigue analysis, though this is out of the scope of the thesis. The goal of this study is to develop a vibration model of the cutter ladder. The research question proposed is: Could resonance be a cause for structural damage to the cutter ladder?

1.2 Approach

Multiple times during this project it was discovered that a chosen path would not yield viable information for further progress. A short outline is given of the path followed.

An initial plan followed was to develop a load model which would translate the cutter shaft torque into dynamic loads at the cutter ladder tip, as these are more or less impossible to measure. A study has been performed to identify whether it is possible to link the measured torque to the measured vibrations on the cutter ladder using by comparing the amplitude in the time domain, this can be found in appendix E. It was identified that no clear link could be established between the measured torque and the vibrations on the cutter ladder. A reason can be found in the fact that the cutter shaft is known to resonate at its first natural frequency. The topic was discussed during a progress meeting and it was decided that it was more convenient to develop a vibration model and validate it only using the vibration measurements from the accelerometers. The use of a load model would have introduced uncertainties and is unnecessary because of the large amount of sensors that were placed on the cutter ladder.

The proposed approach then was to perform operational modal analysis (OMA) on the data to find natural frequencies of the cutter ladder, which could then be used to verify the vibration model. After a quite extensive investigation of the data, it was discovered that the path chosen was not viable as the spectrum of vibrations on the cutter ladder is dominated by forced harmonic vibrations caused by the cutting process, this is elaborated in chapter 3. The chapter on OMA is kept in the thesis as it gives a lot of insight in the dominant vibrations during operating the cutter ladder.

A different approach has been followed afterwards. It was suggested to make use of a load independent method for updating the vibration model. It was therefore chosen to use the transmissibility of vibrations between the locations where vibration sensors were placed on the cutter ladder, and verify these using the vibration model. Using this approach it was possible to identify dynamic characteristics of the cutter ladder itself.

Uncertainties existed whether the water surrounding the structure would influence the dynamic behavior through its added mass and damping. The stiffness of the clamping of the cutter ladder at the main hinge was also found to be unknown. A model updating method has been followed where measured and modeled transmissibility functions are compared to each other, and the added mass, damping and stiffness parameters are varied to obtain a best fit.

The exact path followed is given in figure 1.1.

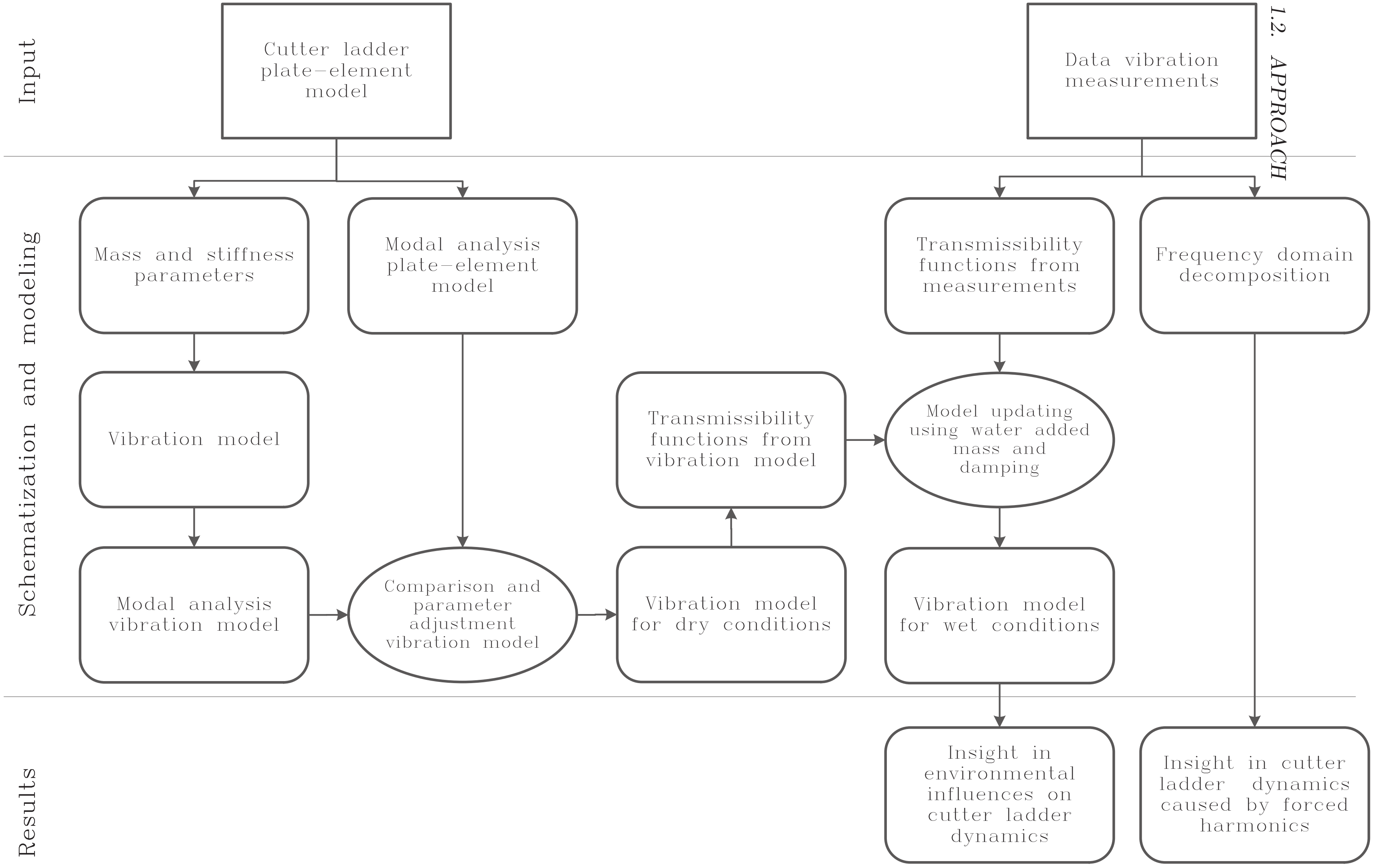

Figure 1.1: *Flow diagram of the approach used*

Chapter 2

Introduction to cutter suction dredgers

This chapter provides an introduction into the use and working principle of cutter suction dredgers (CSDs) in general and about the component of interest for this study, the cutter ladder. For the readers convenience pictures of both the dredger and the cutter ladder are given in figure 2.1. The pictures used are taken from the Taurus II, the self-propelled CSD used within this thesis project. The Taurus II was built for Boskalis by the De Merwede shipyard in 1983, properties of interest are given in table 2.1.

2.1 The cutter suction dredger

A cutter suction dredger is a stationary operating dredge vessel, mainly used for excavating tough materials such as dense sand, clay or rock. CSDs are used for deepening channels and harbors to create pass ways for vessels. Operating depths are currently established up to $\sim 50\,\mathrm{m}$ for the latest CSD, the Taurus II has a maximum operating depth of $\sim 30\,\mathrm{m}$. A side view of the Taurus II is given in figure 2.2 where its main components are listed. The CSD pontoon is supporting the cutter ladder, which is used to position and keep the cutter head at the seabed. Material is excavated by the rotating cutter head and transported to sea level using an internal piping system. Using the pumps present in both the CSD and the cutter ladder, the dredged material can be pumped to a dumping site through a discharge line connected at the bow of the CSD. The spud pole located at the bow constrains the CSD in translation directions, but allows it to

Taurus II properties	
Gross tonnage	$4,375\,\mathrm{mT}$
Overall length	$112.6\,\mathrm{m}$
Breadth	$24\,\mathrm{m}$
Draft	$7.5\,\mathrm{m}$
Max dredging depth	$30\,\mathrm{m}$
Total installed power	$24.6\,\mathrm{MW}$
Cutter power	$4\,\mathrm{MW}$

Table 2.1: *Properties of the Taurus II CSD obtained from [19]*

(a) *The Taurus II cutter suction dredger*

(b) *The Taurus II cutter ladder*

Figure 2.1: *Pictures of the Taurus II*

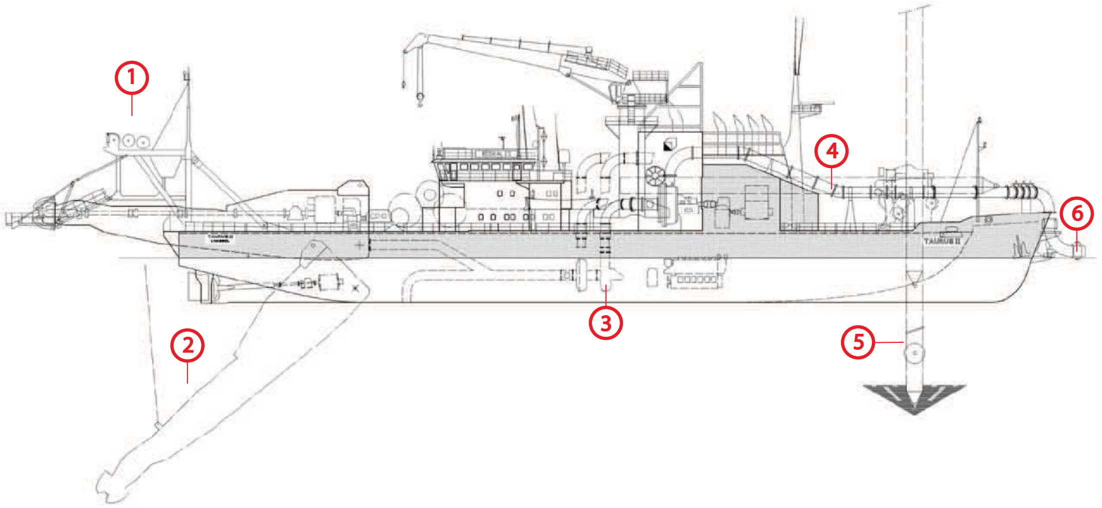

Figure 2.2: *Side view of the Taurus II CSD with the following components listed: 1. Inspection platform, 2. Cutter ladder, 3. Main dredge pump, 4. Discharge pipe, 5. Spud pole, 6. Discharge line connection.*

pivot. The inspection platform above the cutter ladder allows the crew to access the cutter head for example for changing the cutter teeth - also shown in figure 2.1b.

2.2 The CSD dredge process

An overview of the motions made by the CSD during operation is given In figure 2.3. As shown, two swing wires and the spud pole constrain the CSD to the seabed. By pulling in one of the swing wires at a time, the CSD rotates around the spud pole between the two anchors. Whenever a swing is finished, the CSD makes a step forward by moving the spud pole in longitudinal direction of the vessel. Withing the dredge process, several parameters can be varied to obtain the highest possible production. A list of variables relevant within this thesis with a short explanation is given below:

- The **Swing speed** is the speed at which the cutter head moves through the soil in lateral direction.
- The **Rotational speed** of the cutter head can be varied, usually between $23 - 37\,\mathrm{RPM}$.
- The **Step size** is the size of step forward made by the cutter after a swing is finished.
- The **Cutting face** is the thickness of the material layer removed during a swing. The step size combined with the cutting depth determine the amount of material removed in a swing.
- The **Blade number** is the amount of blades on the cutter head. Usually cutter heads have between $5 - 8$ blades. The blade number greatly influences the excitation frequencies of the cutter drive train, as will be elaborated in chapter 3.
- The type of **Pick points** is varied dependent on the soil type to be excavated.

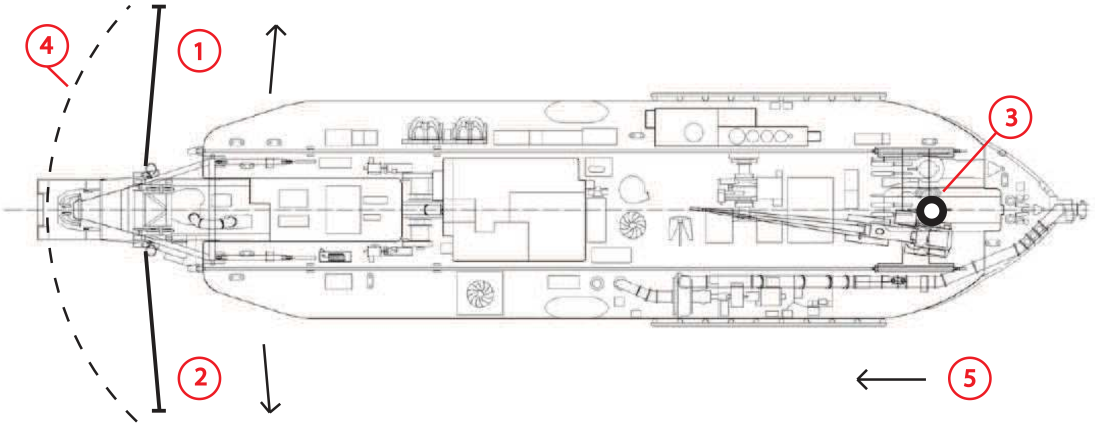

Figure 2.3: *Working principle of a CSD: by pulling in one of the swing wires (1,2) at a time the CSD, pivots around the spud pole (3), moving the cutter head trough the soil in the described path (4). When a "swing" is finished, the spud pole is moved in longitudinal direction, such that the CSD makes a "step" forward (5).*

Other parameters can be varied within the CSD dredging process, though these are not found to be relevant to mention within this thesis work. A study on the influence of these parameters on vibration levels is performed in Van den Berg and Neelissen [22]. The reader is redirected to Vlasblom [23] for further reading on cutter suction dredgers.

2.3 The cutter ladder

The cutter ladder is a large structural member bearing various components critical to the dredging process including the full cutter head drive train and a slurry line with a dredge pump. The Taurus II cutter ladder is shown in figure 2.4, it has a length of $\sim 35\,\mathrm{m}$ and weights $\sim 900\,\mathrm{mT}$. The drive train consist of two electric motors connected to a gearbox with a gear ratio of 31.5 which reduces the rotational speed of the motors and increases the torque at the cutter head. At the output side of the gearbox, a $24\,\mathrm{m}$ long cutter shaft with a diameter of $0.5\,\mathrm{m}$ connects the gearbox with the cutter head. Due to its length, the cutter shaft acts as a torsional spring. A thrust bearing is located before the gearbox preventing damage due to loading in the longitudinal direction.

The cutter ladder has an open structure allowing the water to flow in freely for easy submerging. The engine room in which the E-motors, gearbox and thrust bearing are located is water proof. The dredge pump line is not shown in this figure. The ladder is supported by the vessel through main hinge and hoist wires, and provides support to the sheaves guiding the anchor lines. The swing wire sheaves are not shown in the figure but are located close to the Hoist wire hinges.

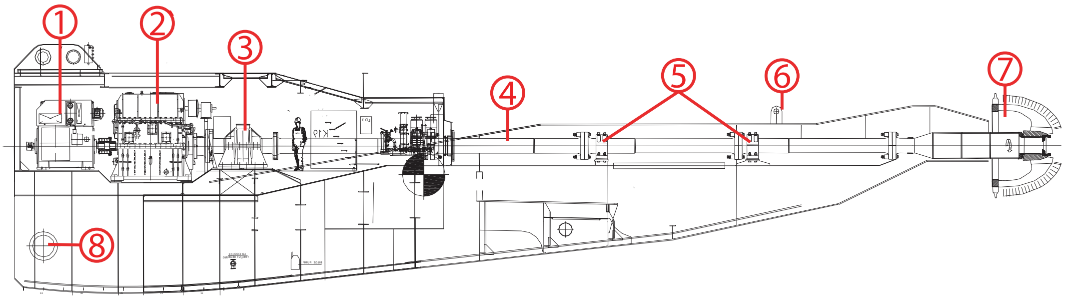

Figure 2.4: *Overview of the components of the cutter ladder including: 1. Electric motors, 2. Gearbox, 3. Thrust bearing, 4. Cutter axle, 5. Radial bearings, 6. Lifting wire hinges, 7. Cutter head, 8. Main hinge.*

Chapter 3

Operational modal analysis

Within this chapter Operational Modal Analysis (OMA) is performed using a technique called Frequency Domain Decomposition (FDD) which uses vibration measurements obtained during the operation of the Taurus II to identify natural frequencies of the cutter ladder. "By performing a decomposition of a spectral density function matrix, the response spectra of multiple signals can be represented by a set of single degree of freedom systems, each corresponding to an individual mode" Brincker et al. [2]. A description of the working principle is given in section 3.2 using an example that includes two datasets each consisting of four artificial vibration signals. The FDD is then performed on six individual datasets to show the influence of known parameters on the results. Next, the FDD is performed on a quite extensive amount of datasets in order to get insight in vibrations of the cutter ladder under various conditions. The results are interpreted and a short discussion is given.

3.1 Measurements

In 2015, a measurement campaign has been performed on the Taurus II cutter suction dredger focused on investigating its dynamic behavior under operational conditions. A test program was executed to identify the influence of various parameters including cutter head type, cutting speed, swing speed and step size. A large amount of measurement sets was obtained, of which 22 were made available for this project. Information regarding the individual measurement sets is listed in table A.1. One measurement set consists of 44 signals logged from 30 accelerometers, 12 displacement sensors mounted on the cutter shaft bearings, a torque sensor mounted on the cutter shaft close to the gearbox and a sensor to measure the cutter ladder angle. Thirteen of the accelerometers were mounted on the cutter ladder. Within this chapter, datasets are assembled only containing measurement from these thirteen sensors. The location and measured direction of the accelerometers can be found in Appendix A.1. A representation of a time trace is given in figure 3.1 where the data of a vertically mounted accelerometer is shown for both the full dataset, and a zoomed section. A full registration of the measurement campaign can be found in [3].

3.2 Frequency domain decomposition example

In this section, the Frequency Domain Decomposition method is explained using two test datasets each consisting of four artificial signals to show its working principle and to verify that the developed algorithm is working correctly. The test datasets will be referred to as the testsets

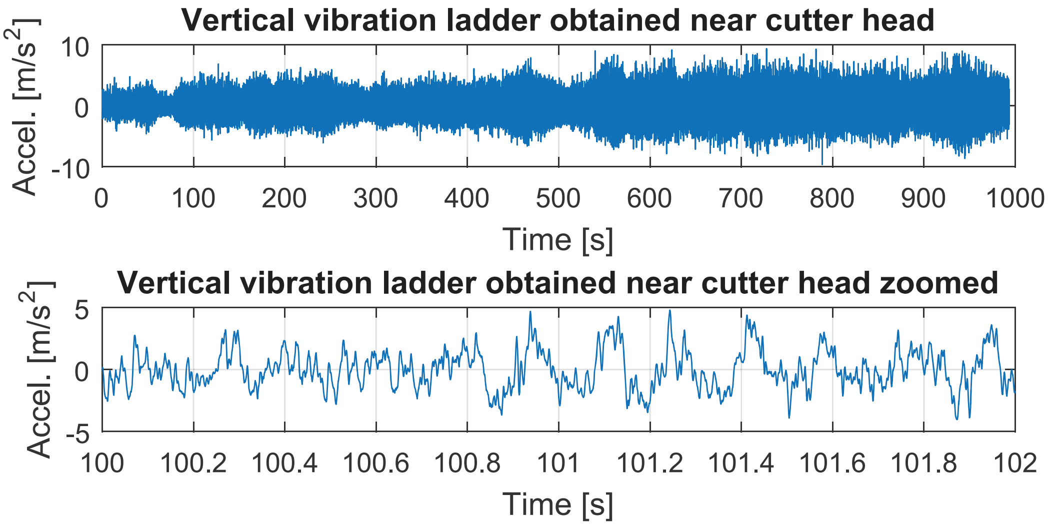

Figure 3.1: *Visual representation of vibrations on the ladder close to the cutter head full dataset and zoomed, (sensor 29)*

and consist of $N = 2^{19}$ datapoints and a sample frequency of $f_s = 4096\,\text{Hz}$ is used similar to the datasets in section 3.3, a sample period of $T_s = 128\,\text{s}$ is hereby created. Reason for taking this sample length is that a Fourier transform is to be performed using MATLABs' Fast Fourier Transform (FFT) algorithm which should have an amount of datapoints equal to a power of 2 (Kamen and Heck [16]) in order to execute it efficient.

The FDD method is used three times in this chapter, where the method is the same but the used datasets differ. It has been chosen to present the method in a step wise approach such that similar steps can be easily identified. For the reader's understanding of the method, all matrices will be fully written out within this section but not in the subsequent sections due to the size of the matrices required there.

It should be noted that in the matrices, a notation $d_{m,n}$ is used, where index m is the column-index and n the row-index. This notation is convenient within MATLAB. Whenever a bold $\mathbf{d}$ is used in combination with m or n it means that a column or row vector is used respectively. Matrices are defined using bold capitals, a superscript number between square brackets indicates' whether the matrix is defined for a certain dataset. Whenever multiple numbers in between the brackets are given, separated by a comma it means that the operation is performed on all matrices defined by the numbers. The steps for the FDD example are outlined below.

Step 1: The time domain matrices are assembled as in equation 3.1, Where $\mathbf{T}(t)^{[1]}$ describes the first dataset and $\mathbf{T}(t)^{[2]}$ describes the second dataset.

$$\mathbf{T}(t)^{[1,2]} = \begin{bmatrix} d(t)_{1,1} & d(t)_{2,1} & d(t)_{3,1} & d(t)_{4,1} \\ d(t)_{1,n} & d(t)_{2,n} & d(t)_{3,n} & d(t)_{4,n} \\ \vdots & \vdots & \vdots & \vdots \\ d(t)_{1,N} & d(t)_{2,N} & d(t)_{3,N} & d(t)_{4,N} \end{bmatrix} \tag{3.1}$$

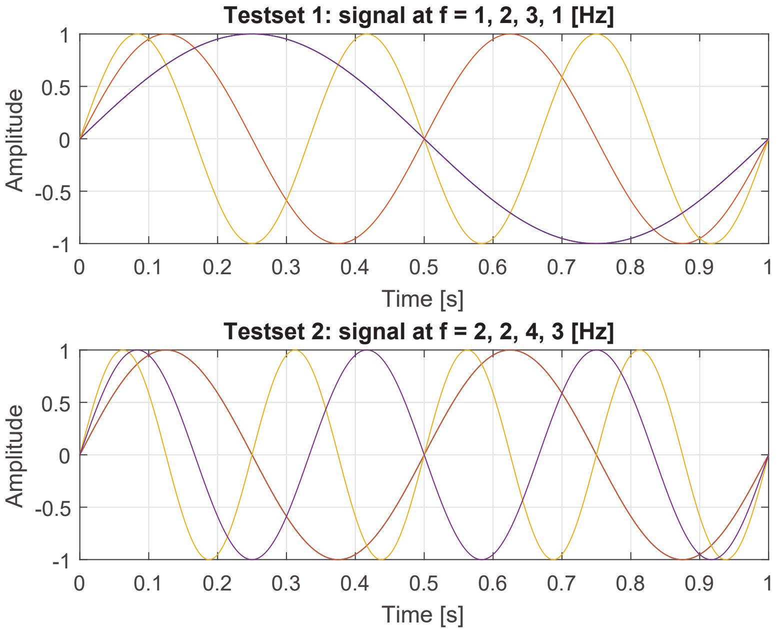

Figure 3.2: *Time domain representation of the example datasets as defined in 3.1*

In both datasets, four discrete time signals $\mathbf{d}_1(t) \rightarrow \mathbf{d}_4(t)$ are created using equation 3.2. The frequency used for each signal is given in table 3.1 and a representation in the time domain is shown in figure 3.2, the amount of signals is arbitrarily chosen.

$$\mathbf{d}_m(t) = \sin(2\pi f_m t) \tag{3.2}$$

For correct understanding of the working principle, one should pay attention to the chosen frequencies in the signals distributed over the datasets.

	f_1[Hz]	f_2[Hz]	f_3[Hz]	f_4[Hz]
Dataset 1	1	2	3	1
Dataset 2	2	2	4	3

Table 3.1: *Frequencies used in the two test datasets*

Step 2: The power spectral density of each of the signals is determined using equation 3.3, where Matlabs' built-in Fast Fourier Transform (FFT) is used and denoted by $\mathfrak{F}$.

$$\mathbf{d}_m(\omega) = |\mathfrak{F}(\mathbf{d}_m(t))|^2 \tag{3.3}$$

Two matrices $\mathbf{P}(\omega)^{[1,2]}$ are hereby created as per equation 3.4, containing the spectral information of the two time domain matrices $\mathbf{T}(t)^{[1,2]}$. Both matrices have a length of $N = 2^{19}$ datapoints. One should note that the integer index n now corresponds to a frequency $\omega = n \cdot \Delta\omega$, where the frequency interval is dependent on the number of datapoints N and the sample frequency f_s, hence $\Delta\omega = {}^{f_s}\!/_{N}$.

$$\mathbf{P}(\omega)^{[1,2]} = \begin{bmatrix} d(\omega)_{1,1} & d(\omega)_{2,1} & d(\omega)_{3,1} & d(\omega)_{4,1} \\ d(\omega)_{1,n} & d(\omega)_{2,n} & d(\omega)_{3,n} & d(\omega)_{4,n} \\ \vdots & \vdots & \vdots & \vdots \\ d(\omega)_{1,N} & d(\omega)_{2,N} & d(\omega)_{3,N} & d(\omega)_{4,N} \end{bmatrix} \tag{3.4}$$

Step 3: For each row n of both matrices $\mathbf{P}(\omega)^{[1,2]}$, the cross product is determined as per equation 3.5, by multiplying vector $\mathbf{d}(\omega)_n$ with its' Hermitian transpose $\mathbf{d}(\omega)_n^H$ such that $\mathbf{Q}(\omega)_n^{[1]}$ is the outer product matrix of dataset 1 at row n, and $\mathbf{Q}(\omega)_n^{[2]}$ is the outer product matrix of dataset 2 at row n.

$$\mathbf{Q}(\omega)_n^{[1,2]} = \mathbf{d}(\omega)_n \mathbf{d}(\omega)_n^H = \begin{bmatrix} d(\omega)_{1,n} \\ d(\omega)_{2,n} \\ d(\omega)_{3,n} \\ d(\omega)_{4,n} \end{bmatrix} \begin{bmatrix} d(\omega)_{1,n} & d(\omega)_{2,n} & d(\omega)_{3,n} & d(\omega)_{4,n} \end{bmatrix} =$$

$$\begin{bmatrix} d(\omega)_{1,n}^2 & d(\omega)_{1,n}d(\omega)_{2,n} & d(\omega)_{1,n}d(\omega)_{3,n} & d(\omega)_{1,n}d(\omega)_{4,n} \\ d(\omega)_{2,n}d(\omega)_{1,n} & d(\omega)_{2,n}^2 & d(\omega)_{2,n}d(\omega)_{3,n} & d(\omega)_{2,n}d(\omega)_{4,n} \\ d(\omega)_{3,n}d(\omega)_{1,n} & d(\omega)_{3,n}d(\omega)_{2,n} & d(\omega)_{3,n}^2 & d(\omega)_{3,n}d(\omega)_{4,n} \\ d(\omega)_{4,n}d(\omega)_1, n & d(\omega)_{4,n}d(\omega)_{2,n} & d(\omega)_{4,n}d(\omega)_{3,n} & d(\omega)_{4,n}^2 \end{bmatrix}^{[1,2]} \tag{3.5}$$

Step 4: A summation of $\mathbf{Q}(\omega)_n^{[1]}$ and $\mathbf{Q}(\omega)_n^{[2]}$ is performed as in equation 3.6. Hereby the information present in the different datasets is represented by one spectral density matrix $\mathbf{S}(\omega)_n$.

$$\mathbf{S}(\omega)_n = \sum \mathbf{Q}(\omega)_n^{[1,2]} = \mathbf{Q}(\omega)_n^{[1]} + \mathbf{Q}(\omega)_n^{[2]} =$$

$$\begin{bmatrix} d(\omega)_{1,n}^2 & d(\omega)_{1,n}d(\omega)_{2,n} & d(\omega)_{1,n}d(\omega)_{3,n} & d(\omega)_{1,n}d(\omega)_{4,n} \\ d(\omega)_{2,n}d(\omega)_{1,n} & d(\omega)_{2,n}^2 & d(\omega)_{2,n}d(\omega)_3 & d(\omega)_{2,n}d(\omega)_{4,n} \\ d(\omega)_{3,n}d(\omega)_{1,n} & d(\omega)_{3,n}d(\omega)_{2,n} & d(\omega)_3^2 & d(\omega)_3 d(\omega)_{4,n} \\ d(\omega)_{4,n}d(\omega)_{1,n} & d(\omega)_{4,n}d(\omega)_{2,n} & d(\omega)_{4,n}d(\omega)_{3,n} & d(\omega)_{4,n}^2 \end{bmatrix}^{[1]} +$$

$$\begin{bmatrix} d(\omega)_{1,n}^2 & d(\omega)_{1,n}d(\omega)_{2,n} & d(\omega)_{1,n}d(\omega)_{3,n} & d(\omega)_{1,n}d(\omega)_{4,n} \\ d(\omega)_{2,n}d(\omega)_{1,n} & d(\omega)_{2,n}^2 & d(\omega)_{2,n}d(\omega)_3 & d(\omega)_{2,n}d(\omega)_{4,n} \\ d(\omega)_{3,n}d(\omega)_{1,n} & d(\omega)_{3,n}d(\omega)_{2,n} & d(\omega)_3^2 & d(\omega)_3 d(\omega)_{4,n} \\ d(\omega)_{4,n}d(\omega)_{1,n} & d(\omega)_{4,n}d(\omega)_{2,n} & d(\omega)_{4,n}d(\omega)_{3,n} & d(\omega)_{4,n}^2 \end{bmatrix}^{[2]} \tag{3.6}$$

Step 5: Singular value decomposition of the spectral density matrix $\mathbf{S}(\omega)_n$ is performed as per equation 3.7 (Lay [17]). A singular value matrix Σ_n is obtained with the singular values on the main diagonal. The eigen vector matrices U and V^T are not of interest for this application. The Matlab built-in SVD command is used to perform the calculation.

$$\mathbf{S}(\omega)_n = (U_n, \Sigma_n, V_n^H) = \begin{bmatrix} U_{1,n} & U_{2,n} & U_{3,n} & U_{4,n} \end{bmatrix} \begin{bmatrix} \sigma_{1,n} & 0 & 0 & 0 \\ 0 & \sigma_{2,n} & 0 & 0 \\ 0 & 0 & \sigma_{3,n} & 0 \\ 0 & 0 & 0 & \sigma_{4,n} \end{bmatrix} \begin{bmatrix} V_{1,n}^T \\ V_{2,n}^T \\ V_{3,n}^T \\ V_{4,n}^T \end{bmatrix} \tag{3.7}$$

Step 6: For each value of n, the singular values located on the main diagonal in Σ_n are saved to matrix Σ as in equation 3.8 by the obtained algorithm. In section 3.2.1 The matrix Σ is shown

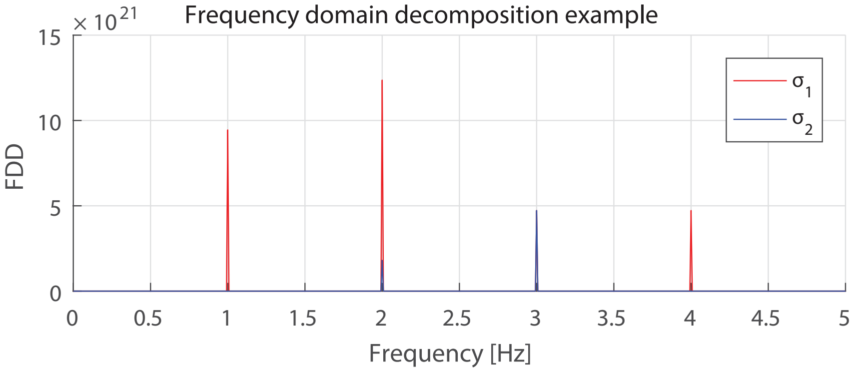

Figure 3.3: *Result of the frequency domain decomposition on the test dataset.*

for its' frequency domain.

$$\Sigma = \begin{bmatrix} \sigma_{1,1} & \sigma_{2,1} & \sigma_{3,1} & \sigma_{4,1} \\ \sigma_{1,n} & \sigma_{2,n} & \sigma_{3,n} & \sigma_{4,n} \\ \vdots & \vdots & \vdots & \vdots \\ \sigma_{1,N} & \sigma_{2,N} & \sigma_{3,N} & \sigma_{4,N} \end{bmatrix} \tag{3.8}$$

3.2.1 Results

The results of the frequency domain decomposition example is shown in figure 3.3 where Σ from equation 3.8 is shown. Spikes show up at the defined signal frequencies. As can be seen in the graph only singular values σ_1 and σ_2 show up, this is because only two datasets are used.

3.2.2 Interpretation

The result of the performed frequency domain decomposition is visualized in figure 3.3. An interpretation of the results is listed below per frequency.

- It can be seen that the frequency at $f = 1\,\mathrm{Hz}$, is represented twice as strong as as the ones at $f = 3, 4\,\mathrm{Hz}$, this is due to the fact that two signals in dataset 1 have this frequency.
- Vibrations found at $f = 2\,\mathrm{Hz}$ in singular value σ_1 are represented three times stronger than the rest of the frequency peaks, and singular value σ_2 is represented too. The sum of the strength of σ_1 and σ_2 is equal to three times the strength of the peaks at $f = 3\,\mathrm{Hz}$ This phenomenon is caused by a combination of mechanisms, the summation is due to the three available signals in both datasets at this frequency. Singular value σ_2 is present because the frequency $f = 2\,\mathrm{Hz}$ is present in both dataset 1 and 2, in different signals.
- At a frequency of $f = 3\,\mathrm{Hz}$ both singular values σ_1 and σ_2 are present, this is caused by the effect of having an excitation at this frequency in two different signals in two different datasets.
- As shown in figure 3.3, the individual harmonics at $f = 4\,\mathrm{Hz}$ are only represented by the first singular value σ_1, despite the fact that this frequency is found in dataset 2. The guiding working principle here is that the spectral information is summed in equation 3.6,

such that the spectral density matrix $\mathbf{S}_n$ contains information of all datasets used. By performing the singular value decomposition from equation 3.7, the spectral density matrix is decomposed into multiple single degree of freedom systems of which the strongest found value is represented by σ_1.

The method is used to identify vibrations that exist in multiple datasets, and are measured by multiple sensors mounted on a structure. When a frequency is strongly present, it could be identified as a natural frequency or a harmonically forced frequency. In a quite late stage of the project it was discussed that presenting the results using resonance peaks might be more insightful, but because of the already obtained structure of the report this has not been included here. The approach is however presented in appendix A.2.

3.3 FDD on individual datasets

The Frequency domain decomposition is performed on six individual datasets that are cut into seven sections to gain insight regarding the influence of the cutting speed and on possible other parameters. A description is given of the used datasets, the method is explained, results are presented followed by an interpretation.

3.3.1 Used data

In this section, six datasets containing measurements of approximately $1000s$ sampled at $f_s = 4096\,\text{Hz}$ are used, hence, every signal set contains approximately $4 \cdot 10^6$ samples. The datasets are obtained during investigating the influence of the cutting speed on the vibrations in the cutter ladder. Within the six datasets, three different cutting speeds are tested and an 8-blade cutter head is used. When identifying vibrations of the ladder, the so-called blade frequency is well present and is determined per equation 3.9, where $N_b = 8$ is the number of blades and $\dot{\phi}_c$ is the cutting speed. The three cutting speeds and their matching blade frequencies are given in table 3.2.

$$f_b\,[\text{Hz}] = \frac{N_b \dot{\phi}_c}{60} \tag{3.9}$$

$\dot{\phi}_c$ [RPM]	27	29	34
f_b [Hz]	3.60	3.87	4.53

Table 3.2: *In the table the rotational speeds of the cutter shaft are given for the different datasets. The associating blade frequency f_b is given following equation 3.9.*

To investigate the similarity of the vibrations in a dataset it is decided to cut the time domain matrix into sections. A length of $N = 2^{19}$ datapoints is chosen, which gives seven sections per dataset. A visual representation of the sectioning is shown for one time trace of an accelerometer in figure 3.4. The remaining data at the end of the time trace is not used (Note: in dataset 2, only six sections are obtained due to the length of the measurement).

3.3.2 Method

For ease of explanation, the FDD procedure is explained for one dataset, results presented in section 3.3.3 are for the six datasets which are numbered as dataset 1 → 6. The method is performed in the six steps as outlined in section 3.2, though the explanation here focuses on the

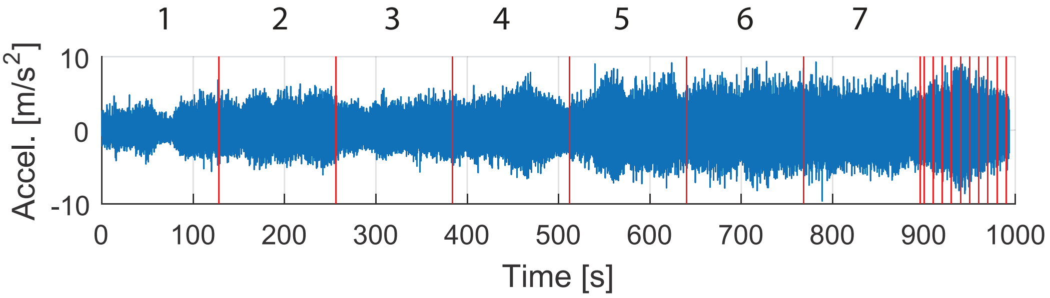

[H]

Figure 3.4: *Each dataset is cut into seven sections with a sample period of* $T_s = 128\,\mathrm{s}$. *A time domain matrix* $\mathbf{T}(t)$ *is obtained from each section. The information left at the end of one dataset is not used in the frequency domain decomposition.*

dimensions of the matrices.

Step 1: Seven time domain matrices $\mathbf{T}(t)^{[1\rightarrow7]}$ are assembled as given in equation 3.10 based on the sectioning performed as shown in figure 3.4 each containing thirteen columns with the data obtained from the thirteen individual sensors as mentioned in section 3.3.1. The superscript index for matrices is used as in section 3.2, to indicate which matrix matches a section.

$$\mathbf{T}(t)^{[1\rightarrow7]} = \begin{bmatrix} d(t)_{1,1} & \dots & d(t)_{13,1} \\ d(t)_{1,n} & \dots & d(t)_{13,n} \\ \vdots & & \vdots \\ d(t)_{1,N} & \dots & d(t)_{13,N} \end{bmatrix} \tag{3.10}$$

Step 2: Seven equally sized power spectral density matrices are determined using equation 3.3 and saved in a spectral density matrix as given in equation 3.11.

$$\mathbf{D}(\omega)^{[1\rightarrow7]} = \begin{bmatrix} d(\omega)_{1,1} & \dots & d(\omega)_{13,1} \\ d(\omega)_{1,n} & \dots & d(\omega)_{13,n} \\ \vdots & & \vdots \\ d(\omega)_{1,N} & \dots & d(\omega)_{13,N} \end{bmatrix} \tag{3.11}$$

Step 3: Seven spectral density matrices $\mathbf{Q}_n^{[1\rightarrow7]}$ are determined at each index n using equation 3.12, where $\mathbf{d}(\omega)_n$ is the column vector of 13 elements at index n and $\mathbf{d}(\omega)_n^H$ is its' Hermitian transpose.

$$\mathbf{Q}(\omega)_n^{[1\rightarrow7]} = \mathbf{d}(\omega)_n \mathbf{d}^H(\omega)_n = \begin{bmatrix} d(\omega)_{1,n} \\ \vdots \\ d(\omega)_{13,n} \end{bmatrix} \begin{bmatrix} d(\omega)_{1,n} & \dots & d(\omega)_{13,n} \end{bmatrix} \tag{3.12}$$

Step 4: A summation of the seven $\mathbf{Q}_n^{[1\rightarrow7]}$ matrices is performed such that one 13×13 matrix $\mathbf{S}_n$ is obtained for every index n as in equation 3.13.

$$\mathbf{S}(\omega)_n = \sum_{1}^{7} \mathbf{Q}(\omega)^{[1\rightarrow7]} = \mathbf{Q}(\omega)_n^{[1]} + \dots + \mathbf{Q}(\omega)_n^{[7]} \tag{3.13}$$

Step 5: Singular value decomposition of each spectral density matrix $\mathbf{S}(\omega)_n$ is performed such that $\mathbf{S}(\omega)_n = U_n \Sigma_n V_n^T$. Hereby one obtains the eigenvalue and eigenvector matrices as in 3.14 at each index n. As seven datasets are used, only seven singular values will be found, just as in section 3.2. Hence, rank $r = 7$ and matrix Σ_r of equation 3.14 has dimension 7×7.

$$\mathbf{S}(\omega)_n = \begin{bmatrix} U_r & \dots & U_0 \end{bmatrix} \begin{bmatrix} \Sigma_r & \dots & 0 \\ \vdots & \ddots & \vdots \\ 0 & \dots & 0 \end{bmatrix} \begin{bmatrix} V_r^H \\ \dots \\ V_0^H \end{bmatrix} \tag{3.14}$$

In equation 3.15 the singular value matrix Σ_n is given. As the matrix $\mathbf{S}_n$ is a summation of seven unique matrices, the SVD method decomposes $\mathbf{S}_n$ into seven singular values.

$$\Sigma(\omega)_n = \begin{bmatrix} \sigma_{1,n} & 0 & \cdots & 0 \\ 0 & \sigma_{2,n} & \cdots & 0 \\ \vdots & \vdots & \ddots & \vdots \\ 0 & 0 & 0 & \sigma_{7,n} \end{bmatrix} \tag{3.15}$$

Step 6: For each value of n, the singular values located on the main diagonal in Σ_n are saved to matrix Σ as in equation 3.16.

$$\Sigma(\omega) = \begin{bmatrix} \sigma_{1,1} & \sigma_{2,1} & \cdots & \sigma_{7,1} \\ \sigma_{1,n} & \sigma_{2,n} & \cdots & \sigma_{7,n} \\ \vdots & \vdots & & \vdots \\ \sigma_{1,N} & \sigma_{2,N} & \cdots & \sigma_{7,N} \end{bmatrix} \tag{3.16}$$

3.3.3 Results

Results of the FDD of each of the six mentioned datasets are given in figures 3.5 →3.7. The singular values $\sigma_1 \rightarrow \sigma_7$ from equation 3.16 are shown for a frequency domain of $f = 0 \rightarrow 10\,\text{Hz}$. Each peak showing up till a frequency of $f = 20\,\text{Hz}$ is listed in table 3.3. The results are shown on a semi logarithmic scale as otherwise the results of the six lowest singular values cannot be visualized.

3.3.4 Interpretation

During listing of the peaks in table 3.3 it is identified that nearly all of the peaks are at fractions of the blade frequency (peak nr. 8). A relation between the peak frequencies and the blade frequency per equation 3.17 is found, where $q = 1 \rightarrow 16$. In the last column of table 3.3, the fraction of the blade frequency of the listed peak is given. As listed in the table, the relation is found at least up to $2 \cdot f_b$. The mechanism behind the relation is not well understood but is not the scope of this project. It does help to identify that most of peaks are not natural frequencies of the cutter ladder.

$$f_p = \frac{q}{N_b} \cdot f_b \tag{3.17}$$

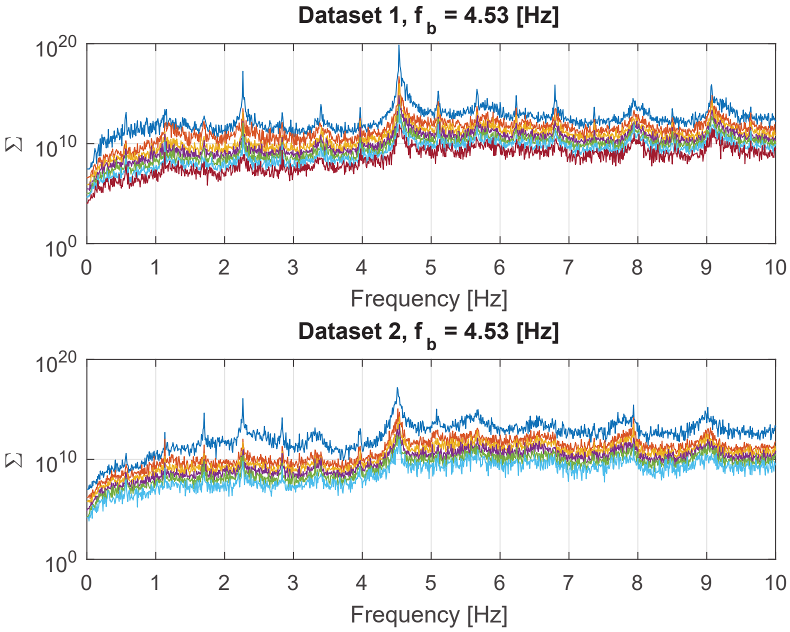

Figure 3.5: *Results of the frequency domain decomposition for datasets with a blade frequency* $f_b = 4.53\,\mathrm{Hz}$.

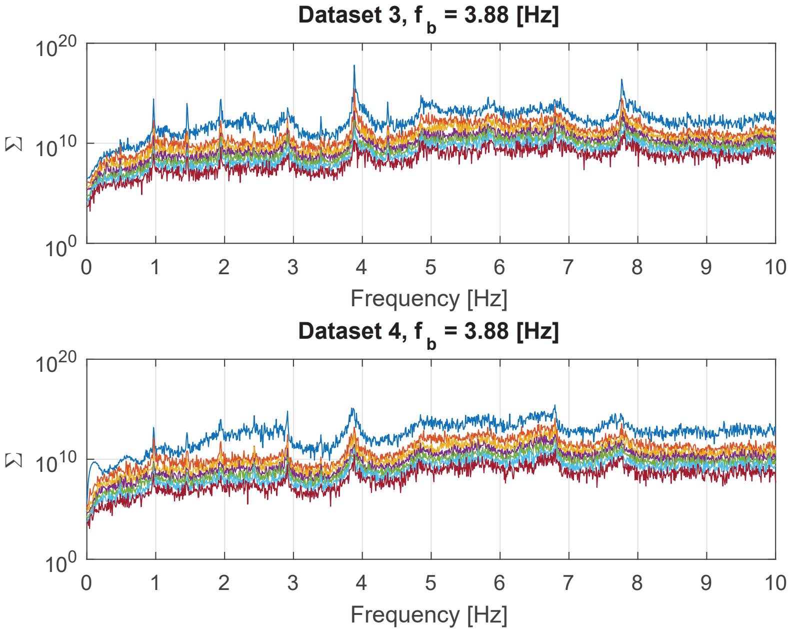

Figure 3.6: *Results of the frequency domain decomposition for datasets with a blade frequency* $f_b = 3.88\,\mathrm{Hz}$.

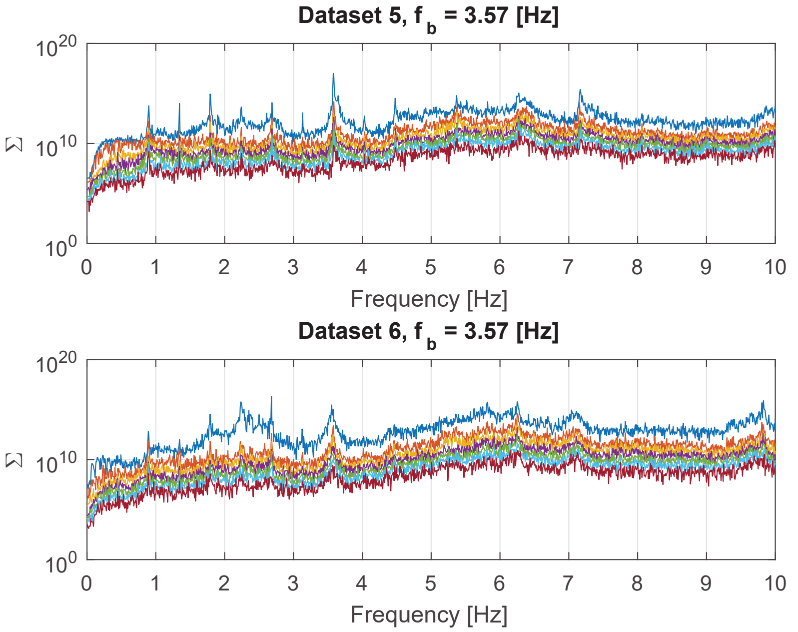

Figure 3.7: *Results of the frequency domain decomposition for datasets with a blade frequency* $f_b = 3.57\,\mathrm{Hz}$*.*

Peak	Set 1	Set 2	Set 3	Set 4	Set 5	Set 6	Fraction
1	0.57	0.57	0.47				${}^{1}/_{8}f_b$
2	1.13	1.13	0.96	0.96	0.90	0.89	${}^{2}/_{8}f_b$
3	1.70	1.70	1.45	1.45	1.34	1.34	${}^{3}/_{8}f_b$
4	2.27	2.27	1.95	1.95	1.78	1.77	${}^{4}/_{8}f_b$
5	2.84	2.84	2.43	2.43	2.24	2.23	${}^{5}/_{8}f_b$
6	3.40	3.40	2.91	2.91	2.69	2.68	${}^{6}/_{8}f_b$
7	3.97	3.97	3.40	3.40	3.13	3.13	${}^{7}/_{8}f_b$
8	4.53	4.51	3.88	3.87	3.58	3.55	f_b
9	5.10	5.10	4.36				${}^{9}/_{8}f_b$
10	5.66	5.68	4.84	4.84	4.47	4.47	${}^{10}/_{8}f_b$
11	6.23	6.50					${}^{11}/_{8}f_b$
12	6.80		5.82	5.83	5.37	5.35	${}^{12}/_{8}f_b$
13	7.36						${}^{13}/_{8}f_b$
14	7.93	7.90	6.88	6.79	6.27	6.25	${}^{14}/_{8}f_b$
15	8.50						${}^{15}/_{8}f_b$
16	9.07	9.00	7.76	7.76	7.16	7.04	$2f_b$
17	11.33						
18	12.48	12.40	10.90	10.50	9.86	9.83	
19	13.60	13.60	11.65	11.50	10.74	10.55	
20	17.20	16.78	14.80	14.40	13.73	13.24	

Table 3.3: *Frequencies [Hz] where peaks are found in the six datasets are listed in the columns Set* $1 \rightarrow 6$ *of this table. The blade frequency as calculated using equation 3.9 can be found at peak 8. Other peaks are found at fractions of the blade frequency* f_b *as defined in equation 3.17 as listed in the last column.*

3.4 FDD on multiple datasets

Based on the results found in section 3.3.4 the idea is raised that it should be possible to obtain more information on the vibrations of the cutter ladder by selecting multiple datasets each containing a different blade frequency and performing the FDD again. As measured vibrations on a structure are a combination of system response and excitation, the conception is that once the structure is excited at a variety of frequencies, there is more chance that it is excited in one or more of its natural frequencies.

3.4.1 Used data

For this section, 22 datasets are used, of which 16 involve measurements taken using a 6-blade cutter head and at a swing speed of $v_s = 15\,{}^{m}\!/_{\min}$. The measurements were also obtained during an investigation of the influence of the cutting speed, which varies over the datasets between $\dot{\phi}_c = 23 \rightarrow 37\,\text{RPM}$. The other six datasets are the same as used in section 3.3, where an 8-blade cutter head is used and a swing speed of $v_s = 5\,{}^{m}\!/_{\min}$. Due to the higher swing speed of the 6-blade datasets, the length of the measurements is approximately one-third of the length of the measurements used in section 3.3, approximately 300 s. Information regarding the individual datasets is listed in table A.1. Note: A short check has been performed to be sure that the relation of equation 3.17 is valid for the 6-blade datasets. The results are not presented but the relation holds.

3.4.2 Method

The reader is redirected to section 3.3.2 for the used method, as the operations performed are exactly the same, though the following should be noted:

- Due to the length of the 16 extra datasets, it is decided to take a section length of $N = 2^{20}$ datapoints per dataset, hence, this is the length of the time domain and spectral density matrix as defined by equations 3.10 and 3.11. The sample length hereby becomes $T_s = 256\,\text{s}$.
- Based on the amount of datasets, now 22 instead of 7 time domain and spectral density matrices are created.
- The matrices as created in equation 3.12 still have a size of 13×13, because of the amount of accelerometers used.
- The summation as performed in equation 3.13 is now performed on 22 matrices instead of 7.

3.4.3 Results

Results are presented in figure 3.8 where all thirteen singular values are shown, both on a linear and a semi-logarithmic scale. Visualization in this manner is done because otherwise only spikes are shown, as can be seen in the top graph.

3.4.4 Interpretation

As shown in the results, the vibrations in the cutter ladder are dominated by forced excitations, much more than by natural frequencies of the system. In the two top singular value lines, the forced excitation is clearly visualized by the spikes. When looking into the linearly scaled graph, the blade frequencies can be identified, between $f = 2.3$ and $4.5\,\text{Hz}$.

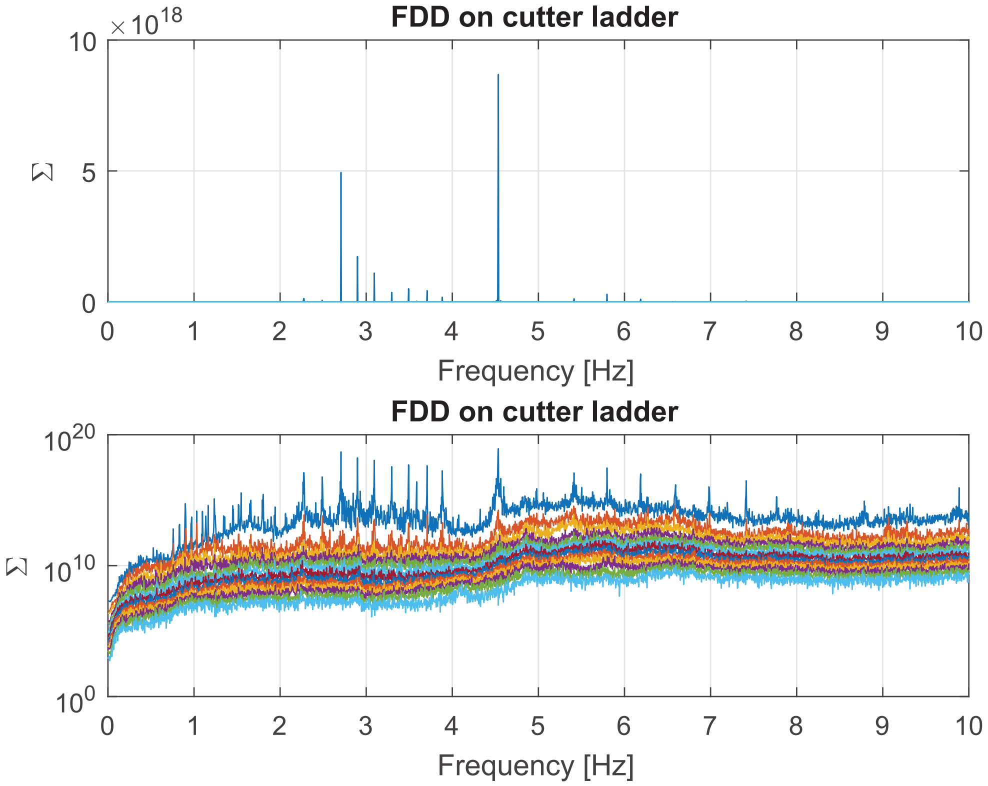

Figure 3.8: *Results of the frequency domain decomposition using 22 datasets. In the upper graph the results are shown on a linear scale, it can be seen that only the spikes of the blade frequencies of the different datasets are shown. The results are presented on a semilogarithmic scale in the lower graph, so that all results obtained using the FDD can be visualized.*

3.5 Discussion

Based on the results presented in this chapter it has to be concluded that the vibrations of the cutter ladder are dominated by the forced harmonic vibrations created by the cutting process. This makes it not possible to use this method for finding natural frequencies of the cutter ladder. Several variations of this approach have been tried, from which a method where the spectrum was corrected by the input power was the most viable approach. The cutter torque and speed is used to obtain the input power. This approach is elaborated in Appendix A.4. The power corrected approach shows that the method is capable of predicting natural frequencies, and thereby also raises the question till what extent dynamic amplification plays a role in the vibrations of the cutter ladder. A different approach for validating the model will be elaborated in chapter 5.

Chapter 4

Vibration model

A vibration model is developed to be able to simulate the behavior of the cutter ladder. A schematization is performed using a finite element model developed by Vuyk Engineering. The finite element model is built up of plate-elements and was initially used for strength calculations, but has been made available for this thesis project. The plate element model is transformed into a CAD model, hereby sectional stiffness and mass parameters of the cutter ladder can be easily obtained. The parameters are used to build a simplified beam-model which can be easily used in dynamic analaysis, as the plate-element model was found to be too detailed to perform dynamic calculations efficiently. A schematization of the cutter ladder is performed in section 4.1.

It has been chosen to use MATLAB as software package for this occasion for multiple reasons, mostly because the author is much more familiar with it than with any other package, and also because it will be easy to implement data from the measurements within the simplified model. The beam model obtained is referred to as the vibration model through this report. Implementation of the obtained parameters is performed in section 4.2 where also an explanation is given of the MATLAB toolbox used.

A comparison is made between the results of modal analysis on both the vibration model and the plate-element model to validate whether they show comparable behavior. This is elaborated in section 4.3

4.1 Schematization of the cutter ladder

A schematization is performed of the cutter ladder. It has been decided to use two sets of beam elements, one to describe the cutter ladder and one to describe the cutter shaft. Reasoning behind taking two sets is that the cutter shaft can rotate freely around its axis, but is constrained in the ladder in translational directions by the radial bearings and in rotational direction at the gearbox. An overview of the schematization is given in figure 4.1, The nodes are indicated by $n_1 \rightarrow n_{17}$ and sections are given by $s_1 \rightarrow s_{10}$. A reference system is introduced with x_0 at the rear plate of the ladder, y_0 is defined in the middle of the ladder, and z_0 is defined at the axis of the main hinge.

4.1.1 Node locations

The node locations in the x-direction have been chosen based on the bearing locations, as these are the locations of the constraints between the cutter ladder and the cutter shaft. All nodes are located in the middle because the cutter ladder is close to symmetric in the vertical plane,

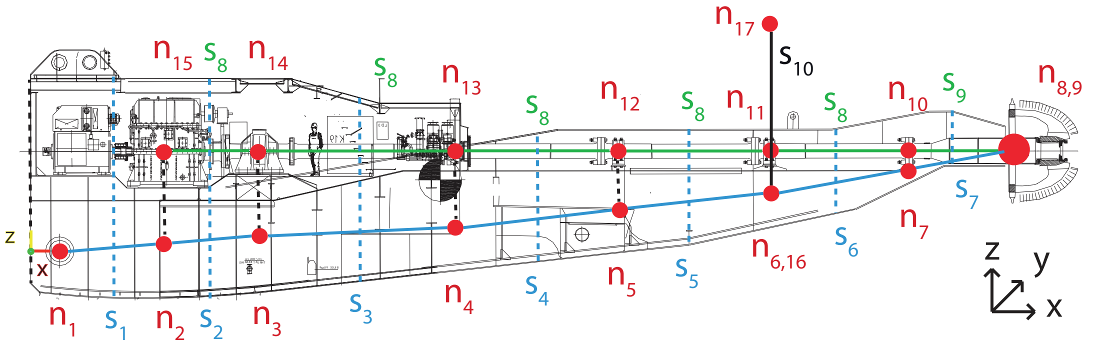

Figure 4.1: *Overview of the introduced cutter ladder schematization, with the reference system located left of node one, the coordinate system is shown right.*

hence $y = 0\,\mathrm{m}$ for each individual node. The vertical location of the nodes has been determined simultaneously with the determination of the sectional parameters, and will therefore be explained in section 4.1.2. The following should be noted regarding the individual nodes:

- Node 1 is located at the main hinge and is clamped in the in multiple directions with a certain stiffness, it can however rotate free around the y-axis.
- Node 2 is located such that it matches the gearbox location on the ladder.
- Node 3 describes the location of the thrust bearing, where the shaft is constrained to the ladder in vertical, horizontal and longitudinal direction.
- Node 4, 5, 6, 7 and 8 describe the locations of the bearings by which the cutter shaft is constrained to the ladder in horizontal and vertical direction.
- The second beam set describes the cutter shaft displacements and is represented by nodes $9 \rightarrow 15$.

4.1.2 Cross sectional parameters

In figure 4.1, sections are given by the dotted blue lines, and indicated using $s_1 \rightarrow s_{10}$. Sections related to the cutter ladder are located midway between two nodes. Autodesk Inventors' sectional properties tool is used to determine the cross sectional parameters for each section. All obtained sectional properties are registered, and a graphical overview of each cross section is given in Appendix B.1. Relevant parameters are listed in table 4.2, including the cross sectional area $A\,[\mathrm{m}^2]$ and area moments of inertia $I_y, I_z\,[\mathrm{m}^4]$.

Area moment of inertia

The principal axes are determined using Autocad for both the area moment of inertia I_y and I_z and can also be found in Appendix B.1, a method on how to obtain the principal axis can be found in Hibbeler [15]. As the ladder is symmetric in y-direction, the principal y-axis is for most sections located close to the reference y-axis, and taken zero for ease of modeling. As the height of the principal z-axis is different for each section, it is chosen to locate the nodes midway

Node	X [m]	Y [m]	Z [m]
1	1	0	0
2	4.8	0	1.1
3	8	0	1.4
4	13	0	1.5
5	21.5	0	1.8
6	25.8	0	2.2
7	30	0	3.1
8	35	0	3.5
9	35	0	3.5
10	30	0	3.5
11	25.8	0	3.5
12	21.5	0	3.5
13	14	0	3.5
14	8	0	3.5
15	4.8	0	3.5
16	2	0	3.5
17	25.8	0	7.2
18	25.8	0	2.2

Table 4.1: *Nodal coordinates as determined based on figure 4.1. Nodes* $1 \rightarrow 7$ *describes the cutter ladder, Nodes* $8 \rightarrow 15$ *describe the cutter shaft, Nodes* $8 \rightarrow 15$ *describe the boundary conditions from the hoist and swing wires.*

between two sections as given in the schematic of figure 4.2 where $i = 1 \rightarrow 7$. The z-location of a node is determined using equation 4.1. The obtained nodal height can be found in table 4.1.

$$n(z)_{i+1} = \frac{s(z)_{i+1} - s(z)_i}{2} + s(z)_i \tag{4.1}$$

The sectional properties s_8 and s_9, belonging to the cutter shaft, are determined using equation 4.2 where $D_8 = 0.5\,\mathrm{m}$ is the diameter of the main cutter axle and $D_9 = 0.67\,\mathrm{m}$ is the diameter of the section known as the cutter head hub, this is where the cutter head is mounted to the shaft.

$$I_y, I_z = {}^{\pi D_i^4}/_{64} \tag{4.2}$$

Torsion constant

The rotational stiffness determined using CAD is not representative, as the method Autocad uses to determine it only applies to solid cross-sections. The cutter ladder structure is quite complex, therefore simplifications have to be made regarding the rotational stiffness. It is therefore chosen to schematize the cross sections as hollow rectangles as given in Young and Budynas [26] to obtain more accurate properties. The stiffness is determined using equation 4.3 for which figure 4.3 applies. The calculations are made based on sections defined by the red rectangles drawn in figures B.1 - B.7. The used dimensions and obtained stiffness are given in table B.8.

$$J = \frac{2tt_1(a-t)^2(b-t_1)^2}{at + bt_1 - t^2 - t_1^2} \tag{4.3}$$

When looking into Cross-sections B.1 - B.7 it is noticed that the structure does not always have a closed cross section. It should therefore be mentioned that the rotational stiffness might still deviate from the determined values.

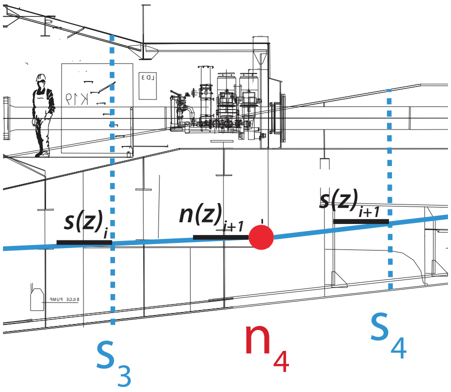

Figure 4.2: *Schematic on how the node height is determined based on the principal z-axes of the individual sections, the definition is used in equation 4.1*

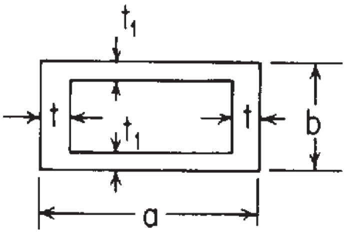

Figure 4.3: *Schematic of rectangular hollow section for determining torsion stiffness constant J using equation 4.3.*

Section	Δ_x [m]	A [m^2]	J [m^4]	I_y [m^4]	I_z [m^4]
1	2.9	4.7	1.73	4.1	7.2
2	6.8	5.8	1.71	3.6	6.3
3	11	2.6	1.8	3.2	6.2
4	17.5	1.7	1.57	1.2	3.9
5	23.2	2.2	0.98	1.1	3.9
6	25.2	1.9	0.85	0.9	3.5
7	27.5	2.6	0.46	0.5	0.3
8	-	0.2	0.006	0.003	0.003
9	-	0.4	0.020	0.010	0.010

Table 4.2: *Sectional properties of the cutter ladder and shaft as obtained in section 4.1.2.*

4.1.3 Mass estimation

An investigation of both the mass of the steelwork and the water added mass is performed. For the steelwork, both the mass of structure and components are taken into account. Water added mass is estimated as it is assumed to influence the dynamics of the cutter ladder, this is performed in chapter 5.

Using Autodesk Inventor and the earlier mentioned CAD model, the mass can be determined easily per defined section, and is listed in table 4.3 under M_s. It should be noted that the section between the rear plate of the cutter ladder and node 1 is not modeled as a beam, as vibration of this section is less of interest. The mass of this part of the structure is added to the component mass mentioned below and adds up to 22.1 mT.

In [4] a list is given containing the components not included in the CAD model. In table 4.3 the component masses are divided over the sections and listed under M_c.

Mass moment of inertia of the components is taken into account as well and included in the last column of table 4.3. A large amount of components is included within the structure and the distance from the component to the rotational center has to be estimated for every component. It has been decided to take the components into account as point masses using equation 4.4, and only if the mass is more than 5 mT. The components taken into account are listed in table B.11. The mass moment of inertia of the structure is taken into account in section 4.2.3.

$$I_c = M_c d^2 \tag{4.4}$$

Section	M_s [mT]	M_c [mT]	I_c [mTm^2]
1	81.5	78.5	228.6
2	47.3	96.7	501.1
3	71.5	53.1	168.6
4	44.2	39.5	12.5
5	36.9	55.7	11.8
6	31.8	29.8	127.4
7	33.9	38.7	20.6

Table 4.3: *Masses per section taken into account in the cutter ladder schematization, where M_s is the structural mass, M_c is the component mass and I_c is the mass moment of inertia of the components.*

4.1.4 Hoist wire schematization

A schematization of the reeving of the hoist wires is given in figure 4.4. The equivalent stiffness is determined applying general rules of springs in parallel. Equations are defined for the wire elongation ΔL and load F at the cutter ladder.

$$\Delta L = {}^{\Delta L_1}/_{3} + \Delta L_2 \tag{4.5}$$

$$F_1 = {}^{F}/_{3} \qquad F_2 = F \tag{4.6}$$

$$\Delta L_1 = \frac{F_1 L_1}{A_w E_w} \tag{4.7}$$

$$\Delta L_2 = \frac{F_2 L_2}{3 A_w E_w} \tag{4.8}$$

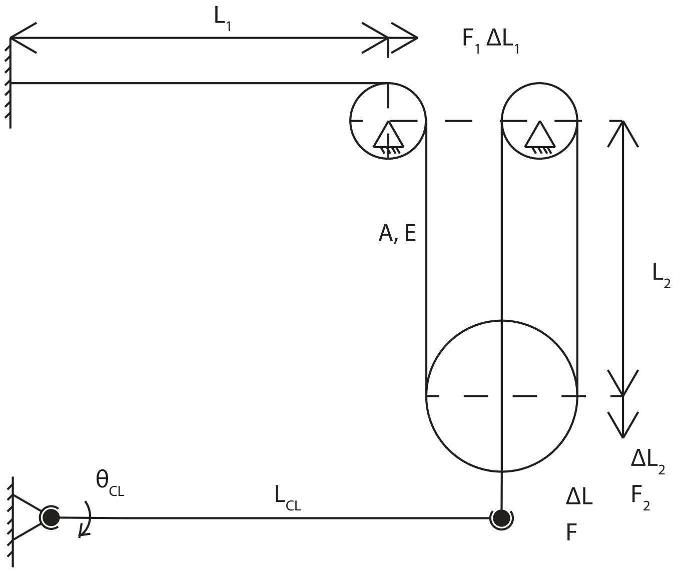

Figure 4.4: *Schematization of hoist wire reeving, with the constants as given in table 4.4.*

Filling in equations 4.6 - 4.8 into 4.5 one obtains the equivalent stiffness as in equation 4.9.

$$k_{eq} = \frac{9A_w E_w}{L_1 + 3L_2} \tag{4.9}$$

The wire lengths are determined based on documentation available at Boskalis. Length L_1 is constant and length L_2 is dependent on the cutter ladder angle θ_{CL} by relation 4.10. Values for the used parameters are found in table 4.4, where θ_c and L_c are correctional parameters for the dimensions of the CSD, these will not be further elaborated here.

$$L_2 = \sqrt{(L_c + L_{CL}\sin(\theta_{CL} - \theta_c))^2 + (L_c\cos(\theta_{CL} - \theta_c) - L_{CL})^2} \tag{4.10}$$

The wire has a cross sectional area of $A_w = 17 \cdot 10^{-3}\,\mathrm{m}^2$ and a Youngs' modulus of $E_w = 105\,\mathrm{GPa}$. The hoist wires stiffness hereby becomes $k_{hw} = 20.7\,{}^{MN}/\mathrm{m}$. The modeled hoist wires have an equivalent length of $L_{eq} = 5\,\mathrm{m}$, this is done for visualization purposes. It should be noted that only one wire is used in the model, while the real cutter ladder is supported by two hoist wires, the stiffness is therefore taken to be $2 \cdot k_{hw}$

L_{CL} [m]	θ_{CL} [°]	L_c [m]	L_1 [m]
25.64	8.3	16	32.2

Table 4.4: *Parameters used in equation 4.10.*

4.1.5 Swing wire schematization

As mentioned in chapter 2 the ladder is constrained by the swing wires in the horizontal plane as shown in figure 2.3. The swing wires provide a stiffness of $k_{sw} = 200\,{}^{kN}/\mathrm{m}$ on both sides of the ladder, as they are kept tensioned during operation to prevent entanglement. The modeled swing wires have an equivalent length of $L_{eq} = 5\,\mathrm{m}$, this is done for visualization purposes. It should be noted that this low stiffness does not have much influence on the behavior of the cutter ladder but is taken into account for completeness of the model.

4.1.6 Suspension at main hinge

Assumptions are made on the stiffness of the boundary condition at the main hinge in both horizontal and vertical direction. A schematization of both the displacement in horizontal and vertical direction is given in figure 4.5.

The total displacement $U_{tip,y}$ of the tip in horizontal direction is dependent on three main parameters, displacement at the model boundary u_y, displacement due to deflection of the beam $u_{d,y}$ and the displacement $\psi_1 \dot{L}_{CL}$ due to rotation at model boundary, hence equation 4.11.

$$U_{tip,y} = u_y + u_{d,y} + \psi_1 L_{CL} \tag{4.11}$$

Displacement of the tip in vertical direction is dependent on vertical displacement at the boundary u_z, the free (but supported by the hoist wires) rotation around the y-axis ϕ_1, and the deflection of the beam due to a load at the tip $u_{d,z}$, Hence equation 4.12. The cutter ladder can rotate freely around the y-axis, hence, $k_{\phi_1} = 0\,{}^{N}/_{m}$.

$$U_{tip,z} = u_z + u_{d,z} + \phi_1 L_{CL} \tag{4.12}$$

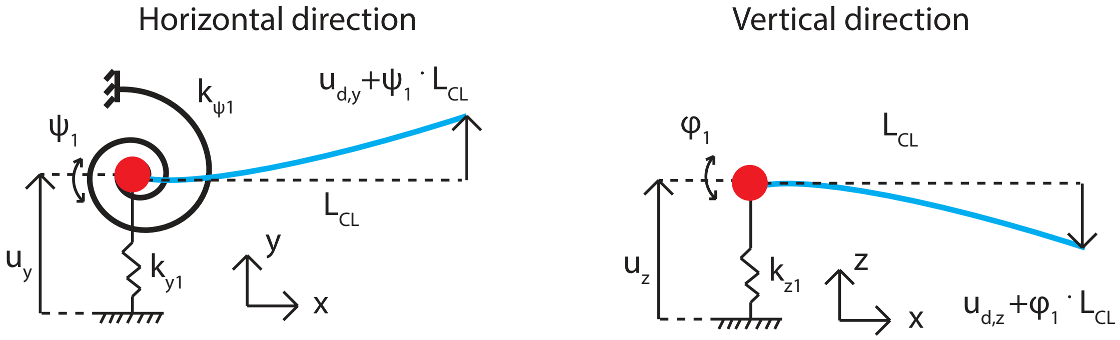

Figure 4.5: *Schematization of the clamping of the cutter ladder in horizontal and vertical direction. The cutter ladder tip can displace in horizontal direction due to rotation around the vertical axis and has a stiffness $k_{\psi 1}$, it can also displace by moving the node at the main hinge in horizontal direction, here it has a stiffness k_{y1}.*

Finding stiffness parameters for the clamping of the cutter ladder is a complex procedure, as it would involve schematization of the hull structure of the cutter suction dredger. The following approach is therefore used. The bending deflections $u_{d,y}$ and $u_{d,z}$ from equations 4.11 and 4.12 are obtained for a fully clamped beam, their values can be found in tables B.9 and B.10. These values are used as reference displacement for their direction. Next it is assumed that each stiffness introduced in figure 4.5 adds 50% of displacement of the tip of the beam. The value of 50% is arbitrarily chosen, but based on the assumption that the displacement caused by the clamping should be in the same ballpark as the ladder deflection. The following stiffness values are hereby determined.

For the rotational stiffness around the z-axis, angle ψ_1 is obtained per equation 4.13 in which $L_{CL} = 35\,\mathrm{m}$ is the cutter ladder length.

$$\psi_1 = \tan \frac{u_{d,y}}{L_{CL}} \tag{4.13}$$

As the displacements from tables B.9 and B.10 are obtained at a unit load of $F = 1\,\mathrm{N}$, the stiffness can be determined easily by taking the inverse values of the displacements, hence equations 4.14 - 4.16, note that the $^1/_2$ accounts for the 50% additional displacement.

$$k_{y1} = (^1/_2 u_{d,y})^{-1} = 1.3 \cdot 10^9\ [^N/_\mathrm{m}] \tag{4.14}$$

$$k_{z1} = (^1/_2 u_{d,z})^{-1} = 1.1 \cdot 10^9\ [^N/_\mathrm{m}] \tag{4.15}$$

$$k_{\psi 1} = (^1/_2 \psi_1)^{-1} = 1.6 \cdot 10^{12}\ [^{Nm}/_\mathrm{rad}] \tag{4.16}$$

Schematization of the suspension of the cutter ladder at its main hinge is shown in figure 4.6 where it can be seen that node one is supported by two clamped beams. The beams both have a length $L_{MH} = 3.4\,\mathrm{m}$ based on the dimensions of the cutter ladder.

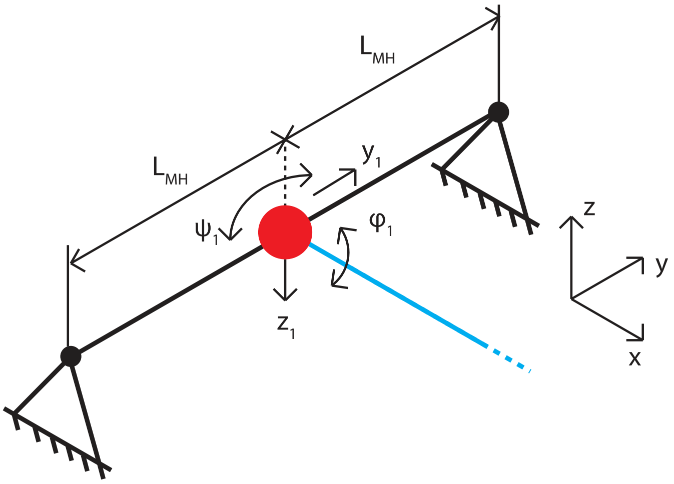

Figure 4.6: *Schematization of the main hinge connection, in which node one of the cutter ladder (blue line) is shown with its degrees of freedom ϕ_1 rotation around the y-axis and ψ_1 rotation around the z-axis.*

Implementation of the stiffness is done using cross-sectional parameters A_{MH}, $I_{y,MH}$ and $I_{z,MH}$ of the modeled main hinge beams. Which are in each case parallel springs, hence, equations 4.17 - 4.19 apply.

$$A_{MH} = \frac{k_{y1} L_{MH}}{2E} \tag{4.17}$$

$$I_{y,MH} = \frac{k_{z1} L_{MH}^3}{6E} \tag{4.18}$$

$$I_{z,MH} = \frac{k_{\psi 1} L_{MH}}{2E} \tag{4.19}$$

As these stiffness parameters are based on assumptions, their values will be evaluated in section 5.1.3.

4.1.7 Ladder shaft connection

The shaft is constrained in the ladder by its bearings, which allow it to rotate freely but constrain it in translation directions. A schematic is given in figure 4.7 where it is shown that the vertical displacement of the shaft is imposed directly onto the ladder. Translation in lateral direction of the shaft introduces both a displacement in lateral direction, and a rotation around the x-axis of the ladder.

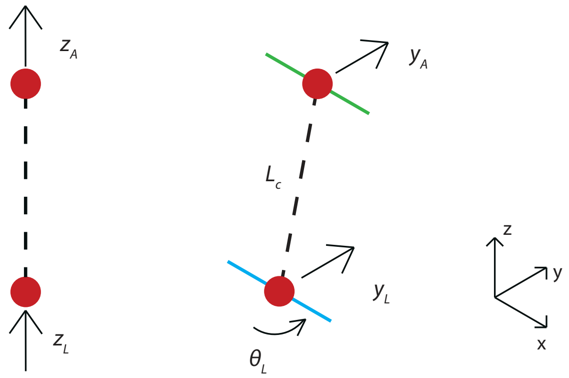

Figure 4.7: *Schematization of constraints applied to the vibration model, Where z_A and z_L are the vertical displacements of the axle and the ladder respectively, y_A and y_L the lateral displacements the axle and the ladder, θ_L is the rotation around the local x-axis and L is the vertical distance between the corresponding ladder and axle nodes.*

4.2 Vibration model cutter ladder

The vibration model is developed using the StaBIL 2.0 finite element toolbox [12], which consists of a set of cooperating Matlab functions used to perform the operations required for FE analysis. The toolbox requires definitions of nodes, sections, elements, materials, degrees of freedom (DOF) and constraints and uses them to assemble the global stiffness and mass matrix. An outline of the performed operations is given below. A graphical representation of the obtained model is given in figure 4.8.

4.2.1 Elements

Assembly of the mass and stiffness matrices is performed by the toolbox. 3D-beam elements are used to model the cutter ladder, each having 12 degrees of freedom, 6 per node. Local stiffness and mass matrices are obtained for each element using equations. The toolbox uses Timoshenko beams as defined in [25]. Local beam convention is given in figure 4.9, note that the z-axis in the vibration model is defined in vertical direction, this is because the schematic is obtained from the manual. The toolbox allows the user to implement a model by defining elements. It therefore requires the definition of the element type, the sectional properties, the used material, and a definition of the nodes it is connected to. In table 4.5 the used elements within the vibration model are given. The hoist and swing wires are modeled as bar elements. The clamping at the main hinge is modeled using two bending beams. The wires and the beams are not listed in table 4.5. The nodes defined can be found in table 4.1.

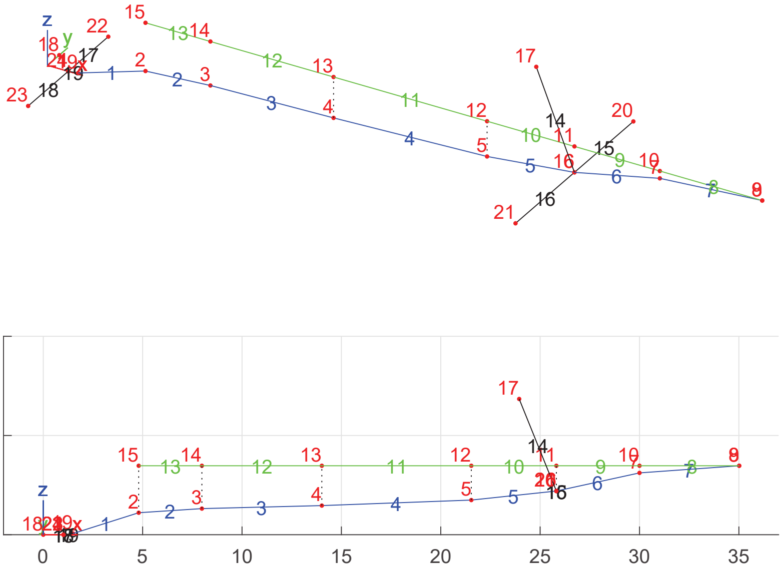

Figure 4.8: *3D and 2D representation of the obtained vibration model. The nodes are represented by red dots, the beams describing the cutter ladder are blue, and the beams describing the axle are green, constraints added between nodes are visualized by the dotted lines black lines. The hoist and swing wires are given by the black lines.*

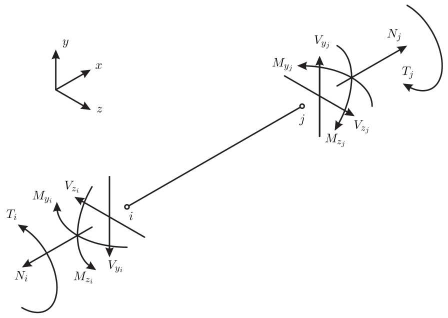

Figure 4.9: *Convention of the beam elements from the used MATLAB toolbox [12]. Note that in the vibration model the z-axis directs in vertical direction.*

Element	Type	Section	Material	Node i	Node j
1	Beam	1	1	1	2
2	Beam	2	1	2	3
3	Beam	3	1	3	4
4	Beam	4	1	4	5
5	Beam	5	1	5	6
6	Beam	6	1	6	7
7	Beam	7	1	7	8
8	Beam	9	1	9	10
9	Beam	8	1	10	11
10	Beam	8	1	11	12
11	Beam	8	1	12	13
12	Beam	8	1	13	14
13	Beam	8	1	14	15

Table 4.5: *Element definitions*

Two material properties are used, Material definition one beholds normal material properties for steel with a density $\rho_s = 7850\,{}^{kg}\!/\!{}_{\mathrm{m}^3}$, a Youngs' modulus of $E = 210\,\mathrm{GPa}$ and a Poissons' ratio of $\nu = 0.3$. material property two is used for the hoist wires, for which only the Youngs' modulus is different, i.e. $E_w = 105\,\mathrm{GPa}$. The sections as defined in table 4.5 are given in table 4.2. The nodal definitions given in table 4.5 are directly related to table 4.1.

4.2.2 Stiffness matrix

The local stiffness matrix used is shown in equation 4.20, for more information and a derivation of this matrix, the reader is referred to Przemieniecki [20] and [14]. The shear deflection coefficients have been taken $k_y, k_z = \infty$ such that the Timoshenko shear coefficient parameters cancel out of the matrices, the beams hereby become Euler-Bernoulli beams. A stiffness matrix as given in equation 4.20 is the result. Due to the size of the mass and stiffness matrices, the reader is referred to Yokoyama [25] or any other literature on Timoshenko beams for a description of the exact content.

$$K = \begin{bmatrix}
\frac{EA}{L} & 0 & 0 & 0 & 0 & 0 & \frac{-EA}{L} & 0 & 0 & 0 & 0 & 0 \\
0 & \frac{12EI_z}{L^3} & 0 & 0 & 0 & \frac{6EI_z}{L^2} & 0 & \frac{-12EI_z}{L^3} & 0 & 0 & 0 & \frac{-6EI_z}{L^2} \\
0 & 0 & \frac{12EI_y}{L^3} & 0 & \frac{-6EI_y}{L^2} & 0 & 0 & 0 & \frac{-12EI_z}{L^3} & 0 & \frac{-6EI_y}{L^2} & 0 \\
0 & 0 & 0 & \frac{GI_x}{L} & 0 & 0 & 0 & 0 & 0 & \frac{GI_x}{L} & 0 & 0 \\
0 & 0 & \frac{-6EI_y}{L^2} & 0 & \frac{4EI_y}{L} & 0 & 0 & 0 & \frac{6EI_y}{L^2} & 0 & \frac{2EI_y}{L} & 0 \\
0 & \frac{6EI_z}{L^2} & 0 & 0 & 0 & \frac{4EI_y}{L} & 0 & \frac{-6EI_z}{L^2} & 0 & 0 & 0 & \frac{2EI_z}{L} \\
\frac{-EA}{L} & 0 & 0 & 0 & 0 & 0 & \frac{EA}{L} & 0 & 0 & 0 & 0 & 0 \\
0 & \frac{-12EI_z}{L^3} & 0 & 0 & 0 & \frac{-6EI_z}{L^2} & 0 & \frac{12EI_z}{L^3} & 0 & 0 & 0 & \frac{-6EI_z}{L^2} \\
0 & 0 & \frac{-12EI_y}{L^3} & 0 & \frac{6EI_y}{L^2} & 0 & 0 & 0 & \frac{12EI_y}{L^3} & 0 & \frac{6EI_y}{L^2} & 0 \\
0 & 0 & 0 & \frac{-GI_x}{L} & 0 & 0 & 0 & 0 & 0 & \frac{GI_x}{L} & 0 & 0 \\
0 & 0 & \frac{-6EI_z}{L^2} & 0 & \frac{2EI_z}{L} & 0 & 0 & 0 & \frac{6EI_y}{L^2} & 0 & \frac{4EI_y}{L} & 0 \\
0 & \frac{6EI_z}{L^2} & 0 & 0 & 0 & \frac{2EI_z}{L} & 0 & \frac{-6EI_z}{L^2} & 0 & 0 & 0 & \frac{4EI_z}{L}
\end{bmatrix} \tag{4.20}$$

4.2.3 Mass matrix

Distributing the mass over the vibration model is performed using two methods. First, a global mass matrix is built up using the local mass matrix from equation 4.22. Information regarding assembly of both local an global mass matrices has been obtained from [9]. As the structure is far from prismatic and quite complex it has been decided to include the sectional mass to the model by using a mass corrected cross sectional area A_m per section as determined using equation 4.21 where M_s is the mass of the structure per section and M_c is the mass of the components per section, ρ_s is the steel density and L_s is the sectional length.

$$A_m = \frac{M_s + M_c}{\rho_s L_s} \tag{4.21}$$

This method is used as it eases the implementation of the mass within the toolbox as one does not have to correct the mass matrix. In case the original cross sections were used, one had to correct for the deviation with the real mass of the structure. It is assumed that this method of implementation is allowed as the cross sectional area only influences the longitudinal stiffness of the beams using the stiffness matrix from equation 4.20, and longitudinal vibrations are considered to be not of interest as their vibration frequency will be high compared to vibrations in the y and z-direction. Implementation of the mass moment of inertia of the structure is performed using the area moment of inertia J as can be seen in equation 4.22.

$$M = \begin{bmatrix}
\frac{\rho_s AL}{3} & 0 & 0 & 0 & 0 & 0 & 0 & 0 & 0 & 0 & 0 & 0 \\
0 & \frac{\rho_s AL}{3} & 0 & 0 & 0 & 0 & 0 & 0 & 0 & 0 & 0 & 0 \\
0 & 0 & \frac{\rho_s AL}{3} & 0 & 0 & 0 & 0 & 0 & 0 & 0 & 0 & 0 \\
0 & 0 & 0 & \frac{\rho_s JL}{2} & 0 & 0 & 0 & 0 & 0 & 0 & 0 & 0 \\
0 & 0 & 0 & 0 & \frac{\rho_s AL^3}{24} & 0 & 0 & 0 & 0 & 0 & 0 & 0 \\
0 & 0 & 0 & 0 & 0 & \frac{\rho_s AL^3}{24} & 0 & 0 & 0 & 0 & 0 & 0 \\
0 & 0 & 0 & 0 & 0 & 0 & \frac{\rho_s AL}{3} & 0 & 0 & 0 & 0 & 0 \\
0 & 0 & 0 & 0 & 0 & 0 & 0 & \frac{\rho_s AL}{3} & 0 & 0 & 0 & 0 \\
0 & 0 & 0 & 0 & 0 & 0 & 0 & 0 & \frac{\rho_s AL}{3} & 0 & 0 & 0 \\
0 & 0 & 0 & 0 & 0 & 0 & 0 & 0 & 0 & \frac{\rho_s JL}{2} & 0 & 0 \\
0 & 0 & 0 & 0 & 0 & 0 & 0 & 0 & 0 & 0 & \frac{\rho_s AL^3}{24} & 0 \\
0 & 0 & 0 & 0 & 0 & 0 & 0 & 0 & 0 & 0 & 0 & \frac{\rho_s AL^3}{24}
\end{bmatrix} \tag{4.22}$$

The second approach uses the definition of point masses and adds them on the main diagonal in the global mass matrix after the global matrix has been built. This is done with various masses, including the mass moment of inertia (MMI) of the components I_c as defined in table 4.3. For ease of implementation, it has been chosen to add the MMI of a section on the subsequent node, hence, the MMI of section 1 is added to node 2. The mass and MMI of the cutter head is implemented applied to node 8. In chapter 5.1, implementation of the water added mass is also performed using this method. The point masses added using this method are listed in table C.3.

4.2.4 Global Matrices

Obtaining the global matrices is performed using the toolbox. First, a list of degrees of freedom is produced, based on the amount of nodes and the definition of the boundary conditions. The vibration model consists of approximately 100 DOF.

Nodal constraints

Constraints are added within the global mass and stiffness matrices. The operation is performed using the toolbox, which removes columns and rows of the slave DOFs and adds them to the defined master DOF as described in Felippa [13]. The constraints as applied to the cutter shaft are listed by constraint $1-16$ in table 4.6, where the slave nodes are listed at the left hand side of the equation and the master nodes are listed on the right hand side of the equation. The constraints applied at the main hinge to node 1 are listed in table 4.6 by constraints $17-21$, where one can read that node 1 is basically pinned to node 24, but can still rotate freely around the y-axis. For a graphical overview the reader is directed to figure 4.8.

	Constraints
1.	$y_9 = y_8$
2.	$z_9 = z_8$
3.	$y_{10} = y_7 - L_{7,10}\theta_7$
4.	$z_{10} = z_7$
5.	$y_{11} = y_6 - L_{6,11}\theta_6$
6.	$z_{11} = z_6$
7.	$y_{12} = y_5 - L_{5,12}\theta_5$
8.	$z_{12} = z_5$
9.	$y_{13} = y_4 - L_{4,13}\theta_4$
10.	$z_{13} = z_4$
11.	$x_{14} = x_3 - L_{3,14}\phi_3$
12.	$y_{14} = y_3 - L_{3,14}\theta_3$
13.	$z_{14} = z_3$
14.	$v_{15} = y_2 - L_{2,15}\theta_2$
15.	$z_{15} = z_2$
16.	$L_{2,15}\theta_{15} = y_2$
17.	$x_1 = x_{24}$
18.	$y_1 = y_{24}$
19.	$z_1 = z_{24}$
20.	$\theta_1 = \theta_{24}$
21.	$\psi_1 = \psi_{24}$

Table 4.6: *Constraints applied in the vibration model based on figures 4.6 and 4.7. Constraints* $1 \rightarrow 16$ *are related to the connection between the cutter ladder and the cutter shaft. Constraints* $17 \rightarrow 21$ *are related to the connection at the main hinge.*

4.3 Model validation using modal analysis

A validation is performed of the obtained vibration model using modal analysis. A comparison is made with the results of the modal analysis performed on the plate-element model, documented in [5] as elaborated in section 4.3.1.

In a quite developed stage of the project it was determined that shear deflection of the cutter ladder is significant compared to the bending deflection. As use is made of Euler-Bernoulli beams, shear deflection is not taken into account in the initial model. A comparison is made of both deflections in horizontal and vertical direction, elaborated in appendix B.4.

As shown in the last columns of both tables B.9 and B.10, shear deflection is quite significant compared to bending deflection, especially in the sections with a large area moment of inertia. Hence, the stiffness of the model is too high when shear deflection is not taken into account. Although the author could start to investigate methods to take shear deflection into account (for example Timoshenko coefficients as in Cowper [6]), it is chosen to leave this untouched due to lack of available time in the project at the moment the influence of the shear deflection was discovered. Instead, it has been chosen to lower the stiffness values of the available parameters

Mode	f [Hz]	Description
1.	0.97	Hoist wires
2.	2.45	Transverse bending
3.	7.81	Vertical Bending
4.	9.41	First torsion mode
5.	10.47	Second order transv. bending

Table 4.7: *Global natural frequencies and mode shapes found with the plate-element model.*

such that the mode shapes and natural frequencies of the vibration model are in agreement with the results of modal analysis performed on the plate-element model.

4.3.1 Modal analysis plate-element model

Modal analysis is performed on the plate-element model developed by Vuyk Engineering. This model is used for strength calculations but due to its high level of detail it was discussed that it would also yield proper results in a modal analysis. Sixteen natural frequencies and mode shapes are found up to 25 Hz, a selection is made to compare with the results of the vibration model. When going through the list, it is noted that quite some of the modeshapes are local plate fields vibrations and are not of interest for this project as the vibration model is only capable of describing global vibrations of the cutter ladder. It has been decided to take into account mode 1 through 5 as these are identified as global vibrations of the cutter ladder. The modes used for comparison are listed in table 4.7.

4.3.2 Vibration model updating using modal analysis

Modal analysis is performed on the vibration model where MATLABs built in eigenvalue and vector algorithm [17] is used to obtain a natural frequency matrix $\mathbf{\Omega}$ and eigen vector matrix $\mathbf{\Phi}$ by solving equation 4.23 where $\mathbf{K}$ and $\mathbf{M}$ are the global stiffness and mass matrices respectively.

$$\mathbf{K\Phi} = \mathbf{M\Phi\Omega}^2 \tag{4.23}$$

Due to the high level of detail of the plate-element model, it is assumed that its results are accurate for the situation where water added mass is not taken into account. Hence, the plate-element model is a good indicator for the stiffness and mass parameters of the vibration model in dry conditions. The results are visualized using an animation tool, a frozen screenshot is given of the first six modes in figure 4.10. A list of the identified modes is given in table 4.8 to provide more insight, as the visualization leaves much to be desired.

Mode	f [Hz]	Description
1.	1.5	Hoist wire
2.	2.2	Transverse bending
3.	4.1	Cutter shaft torsion mode
4.	8.2	Vertical bending
5.	10.7	Transverse bending
6.	13	First torsion mode

Table 4.8: *The first six natural frequencies and mode shapes found using the vibration model.*

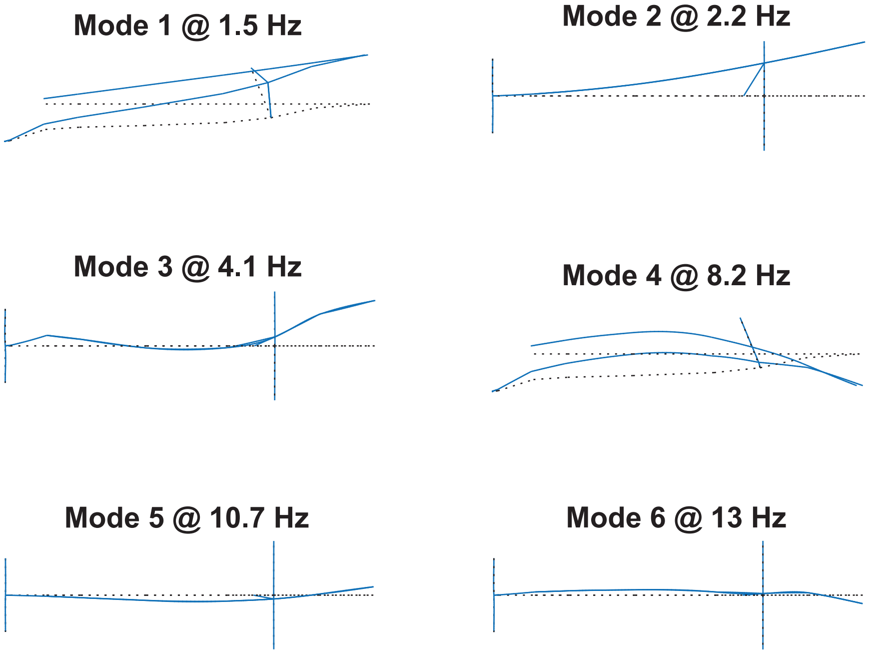

Figure 4.10: *Modal analysis results obtained using the vibration model. A list of the describing the obtained modes is given in table 4.8.*

4.3.3 Comparison of results

A comparison per mode is made between the results of both models below. As mentioned, the stiffness parameters of the cutter ladder beam sections are lowered to obtain more accurate results. In both vertical and horizontal direction the stiffness had to be lowered with 15%.

- The first mode is the motion of the cutter ladder bouncing in the hoist wires. The difference in the results can be explained from the fact that the hoist wire stiffness in the plate-element model does not take into account the reeving of the hoist wires accounted for in section 4.1.4.

- The second mode found with the vibration model is the first transverse bending mode. A slight deviation between the two models, this can be altered by adjusting the rotation stiffness of the main hinge in rotational direction.
- The third mode found with the vibration model is the natural frequency of the cutter shaft which is also found in the measurements of the cutter torque. This natural frequency is not found using the plate-element model as the rotational inertia of the cutter head is not taken into in the plate-element model. This natural frequency is also found in the data from the measurements on the cutter torque, but not presented here.
- The fourth mode found with the vibration model is a vertical bending mode at 8.2 Hz, which is found at 7.8 Hz with the plate element-model.
- The fifth mode found with the vibration model is a second order transverse bending vibration at 10.7 Hz. This mode is found with the plate-element model at 10.5 Hz.
- The sixth mode found with the vibration model is the first torsion vibration mode found at 13 Hz. In the plate-element model this mode is found lower, at 9.4 Hz.

It should be mentioned that when one puts more time into adjusting stiffness parameters, deviations between the models can be reduced further. Due to the time consuming character of this approach it is chosen to keep the values as how they are it this moment.

4.4 Discussion

The comparison of the modal analysis results of both the models show similarity especially in the translation directions. The mode found in the rotational direction is found to be not accurate. Obtaining stiffness and inertia parameters for the rotational motions is found to be more difficult than the parameters in the translation directions.

In general it should be mentioned that the vibration model is a strong simplification of the plate-element model. When going through the plate-element model it is found that the cross sectional parameters vary strongly over the length of the cutter ladder. This combined with its shape makes that simplification may easily introduce errors in modeling.

Besides deviations from the two models, deviations from the real cutter ladder can also still be identified. These deviations mainly come down to the boundary conditions, such as the unknown stiffness of main hinge bearings and the stiffness of the hoist wire support structure.

Chapter 5

Vibration model updating

A vibration model has been obtained in chapter 4 which describes the cutter ladder behavior in dry conditions. The operating environment is however below the water level, which will likely influence the dynamic behavior of the cutter ladder. it is therefore proposed to perform finite element model updating such that the results of the vibration model better reflect the data obtained from the measurements.

Finite element model updating is the process of ensuring that the results of finite element analysis better reflect measured data than the initial model. First, a set of design parameters is chosen based on the measured data, the finite element model should ideally reflect the design parameters. Next, parameters are chosen on which uncertainties exist. These parameters are varied such that the modeled design parameters meet the measured design parameters. This is usually performed by defining an error function between the measured and modeled design parameters, the error function is then to be minimized.

As the initial method, in which it was proposed to verify the vibration model by comparing operational modal analysis results with modal analysis on the model is not yielding desirable results, a different approach is proposed.

In section 5.1 a description is given on how the data obtained with the measurements is presented such that it can be compared to the vibrations the model predicts. As a large quantity of measurements is available, it has been chosen to perform the model updating in the frequency domain, this makes presenting the large quantities of results easier to interpret.

A solution has been found in obtaining transmissibility functions from both the measurements and the model, and use these as the design parameters to update the vibration model. This is elaborated in section 5.1.2.

The water added mass, the damping ratio and the stiffness parameters defined in chapter 4 are used as optimization parameters, a definition is given in section 5.1.3, where also a description is given of the error function.

In section 5.2 this best fit is shown using a multiple input multiple output (MIMO) method to predict the vibrations measured at a certain location using two input signals.

5.1 Transmissibility approach

Within the measurements, data is obtained from thirteen sensors located strategically over the cutter ladder. The sampled accelerations can be combined such that they describe basic motions of the ladder itself. An overview is given in figure 5.1 where it is shown that eleven motions can be obtained, of which four in vertical direction, three in lateral direction and four in rotational

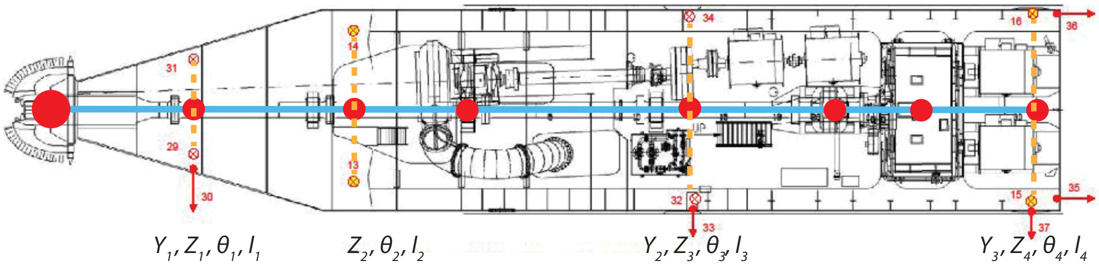

Figure 5.1: *Overview of the schematized accelerations as used in equations 5.1 - 5.3*

l_1 [m]	l_2 [m]	l_3 [m]	l_4 [m]
3	5	6.7	6.7

Table 5.1: *Distance between sensor locations as defined in figure 5.1*

direction. Using equations 5.1 - 5.3 the motions are obtained in the time domain. In table 5.2 the used sensors for each motion are listed. The distance l_n between two sensors as used in equation 5.2 are defined in table 5.1.

$$\ddot{Z}_n(t) = \frac{\ddot{z}_i(t) + \ddot{z}_j(t)}{2} \tag{5.1}$$

$$\ddot{\theta}_n(t) = \frac{\ddot{z}_i(t) - \ddot{z}_j(t)}{l_n} \tag{5.2}$$

$$\ddot{Y}_n(t) = \ddot{y}_i(t) \tag{5.3}$$

The measured vibrations are transposed to the frequency domain and the magnitude is determined. This makes it easier to present a large amount of datasets. To increase the reliability of the method, the frequency responses of the motions from all datasets are added together as per equations 5.4 - 5.6, in which d is the dataset number defined in table A.1. During the project it has been discussed whether it was allowed to add together only the magnitude of the fourier transforms, therefore two other methods of obtaining the motions are presented in appendix C. Based on the presented results in both chapter 5 and appendix C it was chosen to use the method

DOF	Sensor i	Sensor j
$\ddot{Z}_1$	29	31
$\ddot{Z}_2$	13	14
$\ddot{Z}_3$	32	34
$\ddot{Z}_4$	15	16
$\ddot{\theta}_1$	29	31
$\ddot{\theta}_2$	13	14
$\ddot{\theta}_3$	32	34
$\ddot{\theta}_4$	15	16
$\ddot{Y}_1$	30	
$\ddot{Y}_2$	33	
$\ddot{Y}_3$	37	

Table 5.2: *definition of the motions based on the sensor locations as defined in figure 5.1*

following below. It should be noted that the approach of adding together magnitudes of response spectra is only perform to equal out the noise that is shown using the other methods. It has been chosen to use $N = 2^{19}$ datapoints for the Fourier transform, combined with the sample frequency of $f_s = 4.1\,\text{kHz}$ this leads to a sample period per dataset of $T_s = 128\,\text{s}$.

$$\ddot{Z}_n(\omega) = \sum_{d=1}^{22} \mid \mathfrak{F}(\ddot{Z}_n(t))_d \mid \tag{5.4}$$

$$\ddot{Y}_n(\omega) = \sum_{d=1}^{22} \mid \mathfrak{F}(\ddot{Y}_n(t))_d \mid \tag{5.5}$$

$$\ddot{\theta}_n(\omega) = \sum_{d=1}^{22} \mid \mathfrak{F}(\ddot{\theta}_n(t))_d \mid \tag{5.6}$$

All motions as determined using equations 5.4 - 5.6 are shown in figures 5.2 - 5.4. As identified in chapter 3, the response of the cutter ladder is polluted with forced harmonics from the cutting process. However, because the data is obtained at different excitation frequencies, summation of all the datasets makes the forced harmonic vibrations less pronounced and shows the system vibrations more pronounced. This method only works in case a variety of different excitation frequencies is used within the various datasets. The response as visualized in figures 5.4 - 5.4 should not be seen as the vibrations in a cutter ladder during operation, as these are dominated by the forced excitation, this method helps to amplify resonance frequencies in the response spectrum of the cutter ladder.

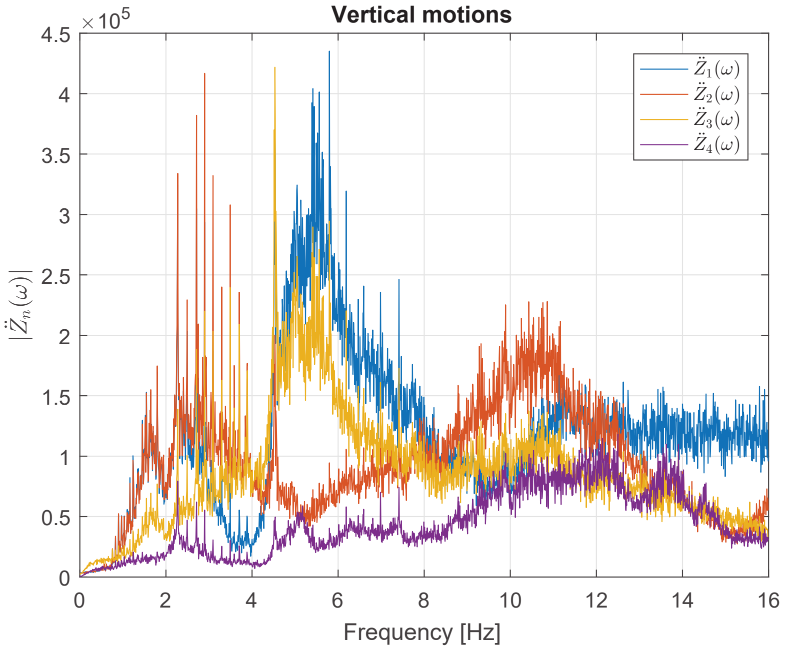

Figure 5.2: *Four vertical motions as obtained using equation 5.4*

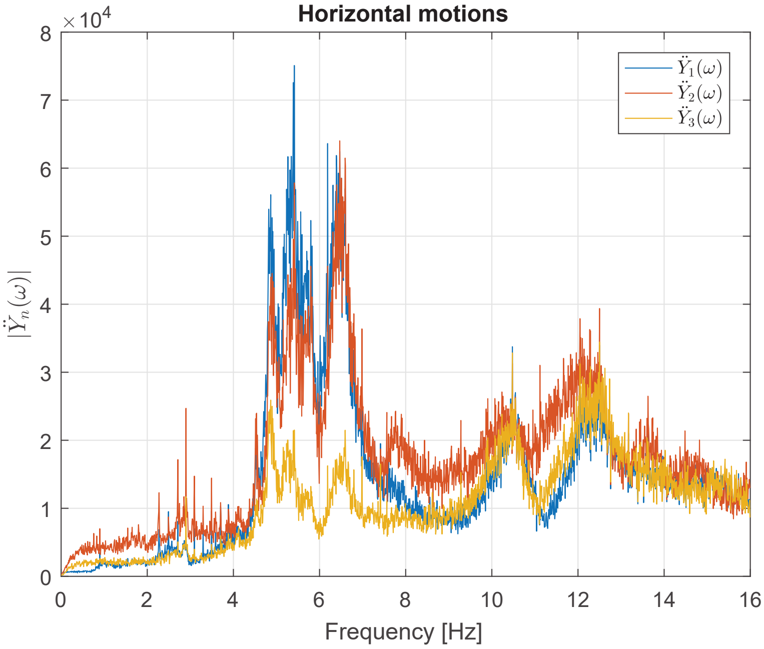

Figure 5.3: *Three horizontal motions as obtained using equation 5.5*

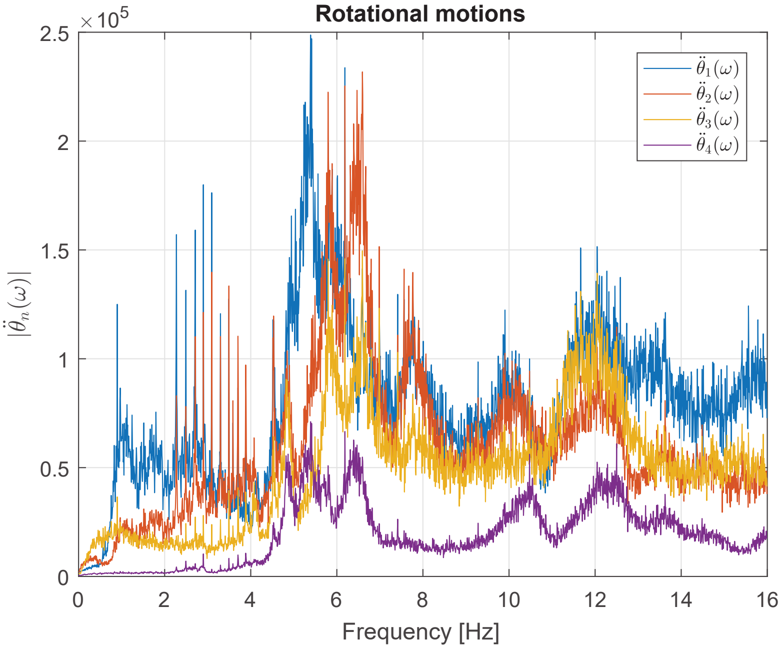

Figure 5.4: *Four rotational motions as obtained using equation 5.6*

5.1.1 Measured transmissibility functions

An approach for validating the model has been found by obtaining the transfer of vibrations between the measured locations on the cutter ladder. Hereby the forced harmonics where found to disappear from the results. The transfer of vibration between two location is in literature known as transmissibility. Transmissibility functions are not that widely used, but several examples can be found in literature on solving dynamic problems. In both Meruane [18] and Steenackers et al. [21] the transmissibility approach is used for updating finite element models, and in Devriendt et al. [11] the transmissibility approach is used for structural health monitoring purposes. The measured transmissibility between the motions is determined using equations 5.7 - 5.9.

$$H_{Zn}(\omega) = \frac{\ddot{Z}_{n+1}(\omega)}{\ddot{Z}_n(\omega)} \tag{5.7}$$

$$H_{Yn}(\omega) = \frac{\ddot{Y}_{n+1}(\omega)}{\ddot{Y}_n(\omega)} \tag{5.8}$$

$$H_{\ddot{\theta}n}(\omega) = \frac{\ddot{\theta}_{n+1}(\omega)}{\ddot{\theta}_n(\omega)} \tag{5.9}$$

The transmissibility functions between the various sensor locations are shown in figures 5.5 - 5.7 for the frequency domain of $f = 0 - 16\,\mathrm{Hz}$. An interpretation of the obtained graphs of the motions and the trainsmissibility functions is given in section **??**.

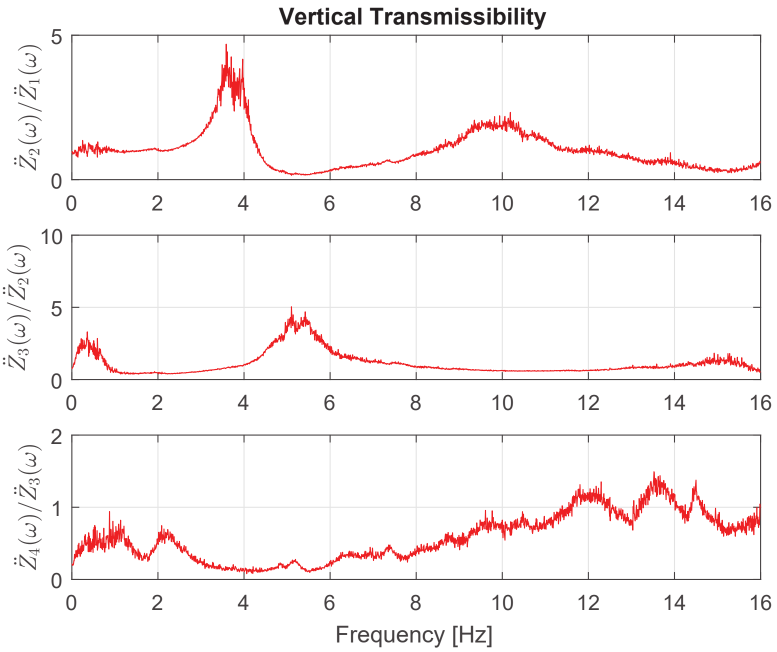

Figure 5.5: *Measured transmissibility functions in vertical direction.*

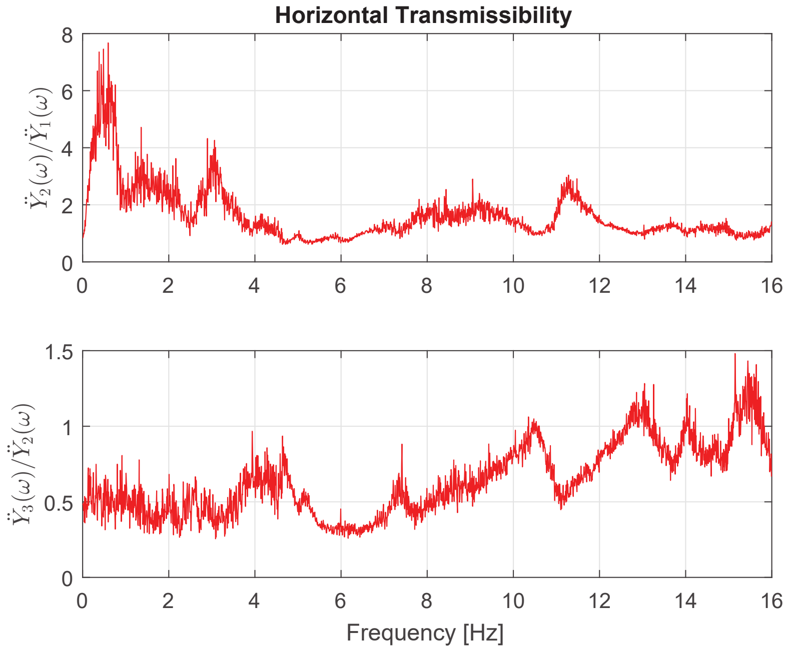

Figure 5.6: *Measured transmissibility functions in horizontal direction.*

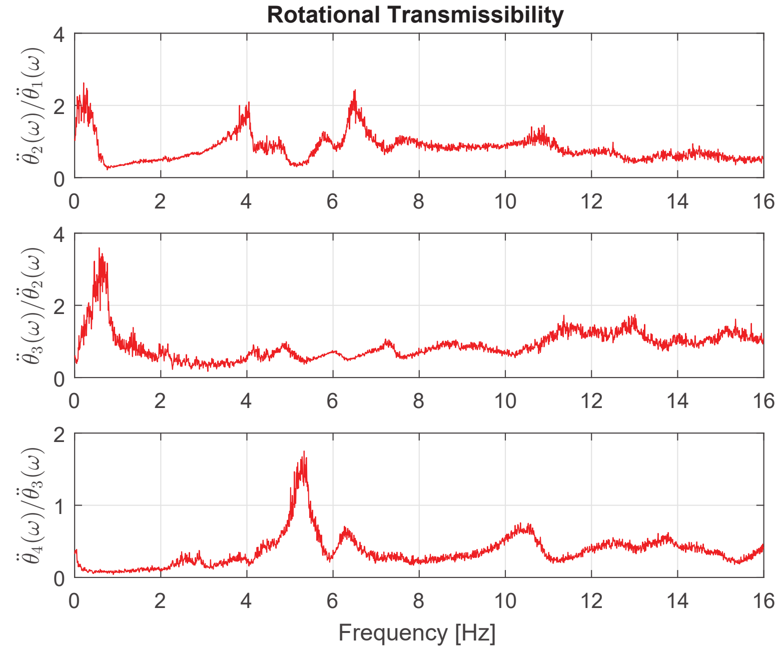

Figure 5.7: *Measured transmissibility functions in torsion direction.*

5.1.2 Modeled transmissibility functions

A method is set up to obtain transmissibility functions from the model, and compare them to the measured transmissibility functions. A comparable approach is found in Wan et al. [24]. The equation of motion (EOM) of the cutter ladder model is determined as in equation 5.10, where a damping matrix **C** and a force vector $\mathbf{F}(t)$ is added. The damping matrix will be discussed in section 5.1.3.

$$\mathbf{M}\ddot{\mathbf{x}}(t) + \mathbf{C}\dot{\mathbf{x}}(\mathbf{t}) + \mathbf{K}\mathbf{x}(t) = \mathbf{F}(t) \tag{5.10}$$

The homogenous EOM is transformed to the frequency domain by using a solution to $\mathbf{x}(t)$ as defined per equation 5.11.

$$\mathbf{x}(t) = \frac{1}{2\pi}\int_{-\infty}^{\infty} \mathbf{X}(\omega)e^{i\omega t}d\omega \tag{5.11}$$

Filling in equation 5.11 into equation 5.10 results in equation 5.12.

$$(-\omega^2\mathbf{M} + i\omega\mathbf{C} + \mathbf{K})\mathbf{X}(\omega) = \mathbf{F}(\omega) \tag{5.12}$$

As the data consists of acceleration measurements, equation 5.12 is derived using equation 5.13.

$$\ddot{\mathbf{X}}(\omega) = -\omega^2\mathbf{X}(\omega) \tag{5.13}$$

It is required for this method to write it in the form $\ddot{\mathbf{X}}(\omega) = \mathbf{T_a}(\omega)\mathbf{F}(\omega)$, hence equation 5.14.

$$-\omega^2(-\omega^2\mathbf{M} + j\omega\mathbf{C} + \mathbf{K})^{-1}\mathbf{F}(\omega) = \ddot{\mathbf{X}}(\omega) \tag{5.14}$$

Matrix $\mathbf{T_a}(\omega)$ is referred to as the transfer matrix. A schematization of the locations of the motions based on the defined measured transmissibility motions is performed. The location of applied forces is given in figure 5.8. Using this schematization it is possible to simulate the measured transmissibility using the vibration model.

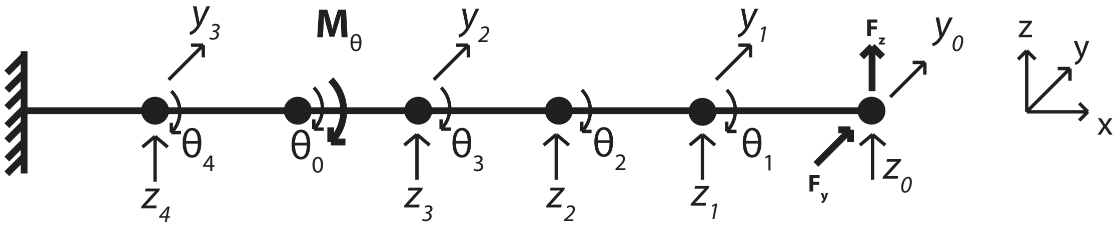

Figure 5.8: *Schematization of the location of the motions and the assumed loads in the vibration model.*

As shown, four vertical, three horizontal and four rotational motions are defined. Besides motions, three locations of applied loads are given. Key to this approach is that the assumption is made that the loading of the structure is applied only at one location per direction. In the schematization this means that the loads acting in vertical and horizontal directions is located at the node defined with z_0, y_0, where the cutter head is located. For the rotational motion, the applied load is located at the gearbox. The assumption is quite accurate in the case of the vertical and torsion motion of the cutter ladder, as in this case the loads are actually only applied at the cutter head and and the gearbox. In the horizontal direction, the assumption is less accurate, as the swing wires is located between motion $\ddot{y}_1$ and $\ddot{y}_2$, introduce a force to swing the CSD around the spud pole. Use is made of transfer matrix $\mathbf{T}_a(\omega)$ which is defined for the fourteen defined motions in equation 5.15. In this equation the relation between the loads F_y, F_z and M_θ with the motions in the directions defined in figure 5.8 are given.

$$\begin{bmatrix} T_{11} & T_{12} & \dots & T_{1-11} & \dots & T_{1-14} \\ T_{21} & T_{22} & \dots & T_{2-11} & \dots & T_{2-14} \\ T_{31} & T_{32} & \dots & T_{3-11} & \dots & T_{3-14} \\ T_{41} & T_{42} & \dots & T_{4-11} & \dots & T_{4-14} \\ T_{51} & T_{52} & \dots & T_{5-11} & \dots & T_{5-14} \\ T_{61} & T_{62} & \dots & T_{6-11} & \dots & T_{6-14} \\ T_{71} & T_{72} & \dots & T_{7-11} & \dots & T_{7-14} \\ T_{81} & T_{82} & \dots & T_{8-11} & \dots & T_{8-14} \\ T_{91} & T_{92} & \dots & T_{9-11} & \dots & T_{9-14} \\ T_{10-1} & T_{10-2} & \dots & T_{10-11} & \dots & T_{10-14} \\ T_{11-1} & T_{11-2} & \dots & T_{11-11} & \dots & T_{11-14} \\ T_{11-1} & T_{11-2} & \dots & T_{12-11} & \dots & T_{12-14} \\ T_{13-1} & T_{13-2} & \dots & T_{13-11} & \dots & T_{13-14} \\ T_{14-1} & T_{14-2} & \dots & T_{14-11} & \dots & T_{14-14} \end{bmatrix} \begin{bmatrix} F_z \\ F_y \\ 0 \\ 0 \\ 0 \\ 0 \\ 0 \\ 0 \\ 0 \\ 0 \\ M_\theta \\ 0 \\ 0 \\ 0 \end{bmatrix} = \begin{bmatrix} \ddot{z}_0 \\ \ddot{y}_0 \\ \ddot{z}_1 \\ \ddot{y}_1 \\ \ddot{\theta}_1 \\ \ddot{z}_2 \\ \ddot{y}_2 \\ \ddot{\theta}_2 \\ \ddot{z}_3 \\ \ddot{\theta}_3 \\ \ddot{\theta}_0 \\ \ddot{z}_4 \\ \ddot{y}_3 \\ \ddot{\theta}_4 \end{bmatrix} \tag{5.15}$$

Matrix 5.15 can be reduced because most of the terms in the force vector are zero as no load is applied at these nodes. To find the transmissibility functions as given in section 5.1, it is assumed that the motions and forces are uncoupled in the various directions. Hereby one obtains the matrices from equations 5.16 - 5.18.

$$\begin{bmatrix} T_{31} \\ T_{61} \\ T_{91} \\ T_{12-1} \end{bmatrix} \begin{bmatrix} F_z \end{bmatrix} \begin{bmatrix} \ddot{z}_1 \\ \ddot{z}_2 \\ \ddot{z}_3 \\ \ddot{z}_4 \end{bmatrix} \tag{5.16}$$

$$\begin{bmatrix} T_{42} \\ T_{92} \\ T_{13-2} \end{bmatrix} \begin{bmatrix} F_y \end{bmatrix} \begin{bmatrix} \ddot{y}_1 \\ \ddot{y}_2 \\ \ddot{y}_3 \end{bmatrix} \tag{5.17}$$

$$\begin{bmatrix} T_{51} \\ T_{81} \\ T_{10-1} \\ T_{14-1} \end{bmatrix} \begin{bmatrix} M_\theta \end{bmatrix} \begin{bmatrix} \ddot{\theta}_1 \\ \ddot{\theta}_2 \\ \ddot{\theta}_3 \\ \ddot{\theta}_4 \end{bmatrix} \tag{5.18}$$

The modeled transmissibility functions can be found by solving the modeled motions for the force vector. An example is given for transmissibility function ${}^{\ddot{z}_2}/{}_{\ddot{z}_1}$ by equation 5.19.

$$T_{31}F_z = \ddot{z}_1, \qquad T_{61}F_z = \ddot{z}_2 \tag{5.19}$$

When performing this for each transmissibility function, equations 5.20 - 5.22 are obtained.

$$\frac{\ddot{z}_2}{\ddot{z}_1} = \frac{T_{61}}{T_{31}}, \qquad \frac{\ddot{z}_3}{\ddot{z}_2} = \frac{T_{91}}{T_{61}}, \qquad \frac{\ddot{z}_4}{\ddot{z}_3} = \frac{T_{12-1}}{T_{91}} \tag{5.20}$$

$$\frac{\ddot{y}_2}{\ddot{y}_1} = \frac{T_{72}}{T_{42}}, \qquad \frac{\ddot{y}_3}{\ddot{y}_2} = \frac{T_{13-2}}{T_{72}} \tag{5.21}$$

$$\frac{\ddot{\theta}_2}{\ddot{\theta}_1} = \frac{T_{8-11}}{T_{5-11}}, \qquad \frac{\ddot{\theta}_3}{\ddot{\theta}_2} = \frac{T_{10-11}}{T_{8-11}}, \qquad \frac{\ddot{\theta}_4}{\ddot{\theta}_3} = \frac{T_{14-11}}{T_{10-11}} \tag{5.22}$$

As the transfer matrix is frequency dependent, an algorithm is set up which calculates the transfer matrix $\mathbf{T_a}(\omega)$ for the frequency range $f = 0 - 16\,\text{Hz}$, with a step size of $\Delta f = {}^{4096}/_{2^{19}}\,\text{Hz}$. Results are hereby obtained with the same range and step size as the measured transmissibility functions. The modeled transmissibility functions can then be obtained from transfer matrix $\mathbf{T_a}(\omega)$.

5.1.3 Updating parameters

Initial results of the modeled transmissibilitiy functions show an offset to the measured transmissibility functions. A selection is made of parameters that can be used to update the model such that the results show more comparable behavior. Use is made of an error function which is to be minimized by varying the chosen parameters. These are the water added mass, the damping ratio and the stiffness parameters at the main hinge. A definition of the error function, and the initial values of the parameters to vary is given in this section.

Water added mass

Water added mass is known to influence dynamic behavior of submerged structures. As mentioned in chapter 2 the cutter ladder is an open structure, it is therefore assumed that water both internal and external should be taken into account. The already defined sections are used for determining the distribution of the water added mass. In figure 5.9 a schematic is given, where the red sections apply to the internal water added mass and the external added mass in horizontal direction. The blue lines show the sections taken into account for external water added mass in vertical direction. Water surrounding the structure is taken into account using a code from DNV [10]. Further specification of the calculations performed is given in appendix C.1. The following assumptions are made:

- Ten volumes are taken into account for the water included in the structure.
- Both sides of the submerged parts of the cutter ladder are taken into account for the external water added mass in both horizontal and vertical direction.
- The water level is located $\sim 1.5\,\text{m}$ below the main hinge.
- The cutter ladder is positioned under an angle of $22\,^{\circ}$.
- A water density of $\rho_w = 1025\,{}^{kg}/_{\text{m}^3}$ is used.
- The amount of water included in section 7 is found to be negligible.
- In horizontal direction, the water added mass at sections 1, 2 and 6 are found negligible as well.
- Water added mass in torsion direction is found to be negligible.

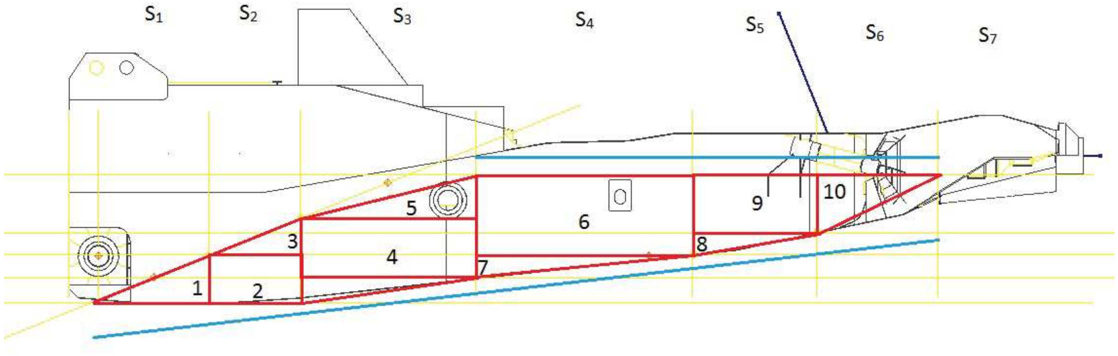

Figure 5.9: *Schematic of water added mass included in the cutter ladder hull (red sections) and the water added mass due to the moving body (blue sections)*

The water added mass per section internal, and external in horizontal and vertical direction can be found in table 5.3.

Section	M_{wi} [mT]	$M_{we,y}$ [mT]	$M_{we,z}$ [mT]
1	21.2	0.0	56.8
2	49.6	0.0	41.7
3	118.1	127.8	122.6
4	165.5	223.3	399.1
5	71.1	51.1	155.1
6	24.2	0.0	109.9
7	0.0	0.0	0.0

Table 5.3: *Water added mass internal M_{wi}, external horizontal $M_{we,y}$ and external vertical $M_{we,z}$.*

As the masses differ in vertical and horizontal direction it is chosen to add them in the global mass matrix. It is therefore required to distribute the sectional mass over the individual nodes. The exact distribution per node is given in the 'Nodal mass' column of table 5.4. The sectional per direction and is found by summation of the internal with the corresponding external mass, hence, $M_{a,s} = M_{wi} + M_{we,y/z}$.

Node	Nodal mass	$M_{a,y}$ [mT]	$M_{a,z}$ [mT]
1	$^1\!/_2 M_{a,s1}$	10.6	39.0
2	$^1\!/_2(M_{a,s1} + M_{a,s2})$	35.4	84.6
3	$^1\!/_2(M_{a,s2} + M_{a,s3})$	147.8	166.0
4	$^1\!/_2(M_{a,s3} + M_{a,s4})$	317.4	402.7
5	$^1\!/_2(M_{a,s4} + M_{a,s5})$	255.5	395.5
6	$^1\!/_2(M_{a,s5} + M_{a,s6})$	73.2	180.2
7	$^1\!/_2(M_{a,s6})$	12.1	67.1

Table 5.4: *Distributing water added mass over the nodes.*

The obtained water added mass should be seen as rough estimate. It is decided to vary the initial values in both horizontal and vertical direction between 10% and 200% to identify the real amount of water added mass. Results are presented in section 5.1.4.

Damping ratio

A modal damping matrix is introduced to add damping to the system,the matrix has been obtained from [8] and [12]. The matrix is defined as in equation 5.23. The most suitable damping is determined by varying the damping factor ξ between 1% and 15% and a step size of 1%, using the error algorithm.

$$\mathbf{C}(\omega) = \mathbf{M^T \Phi} 2\xi \mathbf{diag}[\Omega_n]\mathbf{M \Phi^T} \tag{5.23}$$

Main hinge stiffness

As mentioned in section 4.1.6 the stiffness at the main hinge is based on the assumption that the deflections due to the clamping should be in the same range as the total deflection of the cutter ladder. It has been chosen to vary each of the three boundary stiffness parameters k_{y1}, k_{z1} and $k_{\psi 1}$ between 10% and 200% of their initial value and a step size of 10%, and use the error function to obtain the most accurate results.

Error function

An error function is defined per equation 5.24, where the modeled and measured transmissibility functions are compared and summed over the frequency range $f = 0 \rightarrow 16\,\text{Hz}$. Due to lack of time it has been chosen to only optimize the horizontal and vertical transmissibility functions, hence the equations 5.20 and 5.21 are used for the modeled transmissibility, and are compared to equations 5.7 and 5.8 being the measured transmissibility. By varying the parameters defined above and optimizing for $\epsilon \rightarrow 0$.

$$\epsilon = \sum_{f=0\rightarrow 16\,\text{Hz}} \frac{\mid\mid \mathbf{H}_{ME}(\omega) \mid - \mid \mathbf{H}_{MO}(\omega) \mid\mid}{\mid \mathbf{H}_{MO}(\omega) \mid} \tag{5.24}$$

It should be noted that this function is only used as indicative measure to lower error between the measured and the modeled transmissibility functions. All optimization is performed manually, no automated algorithms or any of such approaches is used here. In section 5.1.4 the results of the error minimization and the obtained values for the parameters are presented.

5.1.4 Results

Results are shown in figures 5.10 and 5.11. Due to lack of time it has been decided to only take into account the horizontal and vertical direction for performing the vibration model. In table 5.5 the obtained parameters to be updated as mentioned in section 5.1.3 are given based on their initial value. A damping factor $\xi = 7\%$ was found, this value is obtained by scaling the peak of transmissibility function $\ddot{z}_2(\omega)/\ddot{z}_1(\omega)$ in figure 5.10 to match the measured transmissibility function.

Parameter	% Init. value
$M_{a,y}$	40
$M_{a,z}$	90
k_{y1}	300
k_{z1}	150
$k_{\psi 1}$	100

Table 5.5: *Obtained optimization parameters*

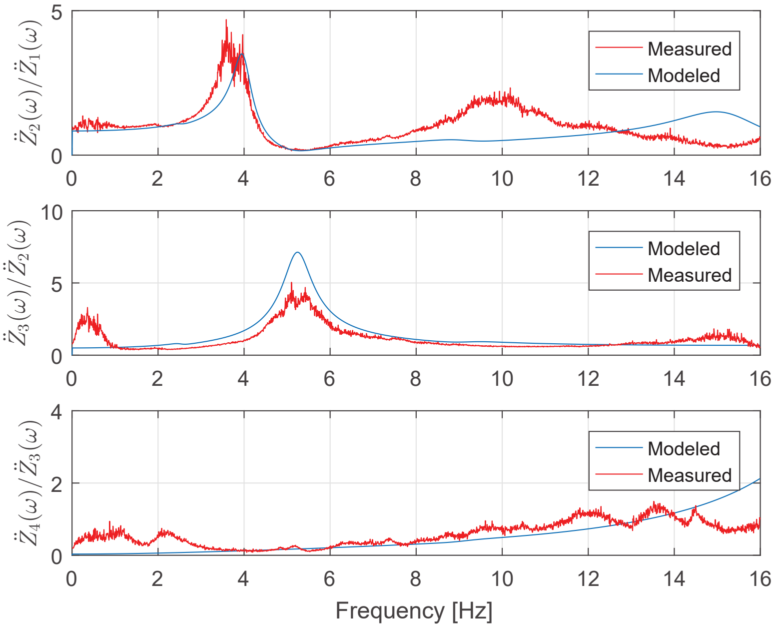

Figure 5.10: *Transmissibility in vertical direction, modeled vs measured*

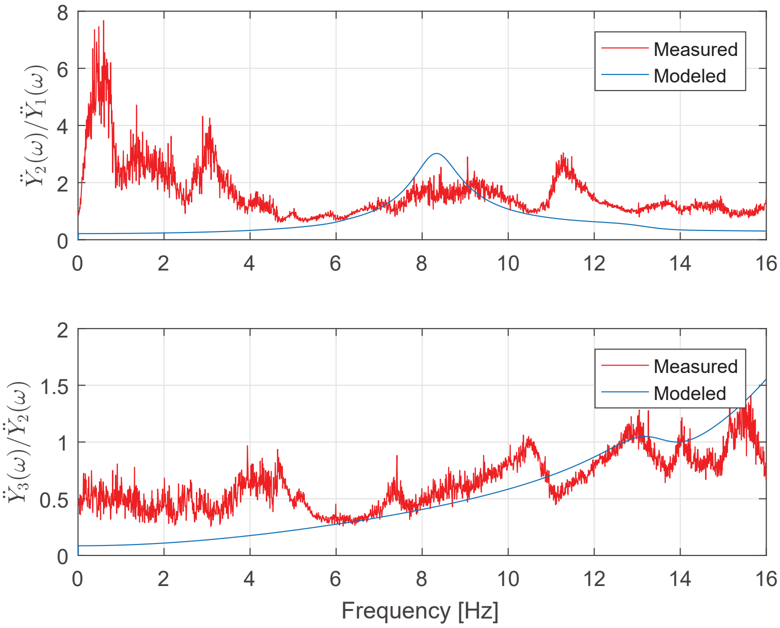

Figure 5.11: *Transmissibility in horizontal direction, modeled vs measured*

5.1.5 Interpretation

An interpretation is given to multiple paragraphs of this section. First an interpretation is given to the measured motions, next the obtained results from the comparison of the transmissibility approach is given.

Measured motions

The results presented in section 5.1 imply that it is possible to identify dynamic characteristics of the cutter ladder structure. This is due to the availability of a variety of datasets which each contain information of both forced vibrations, caused by the cutting process, and free vibrations of the cutter ladder itself. As the forced vibrations are much stronger present in an individual dataset, free vibrations are less easy find as earlier determined in chapter 3. It has been identified that free vibrations can be visualized by performing a summation of all datasets. A schematization of the summation is given in figure 5.12 to clarify what is shown in figures 5.2 - 5.4. As mentioned in chapter 4 the forced vibrations caused by the blade frequency are unique for each two datasets as can found in table A.1; this is visualized by the straight narrow bars. Resonance of the structure however is found in all datasets at the same frequency. By adding all datasets together, the effect shown in figure 5.12 occurs: the forced vibrations are not added together as they are located at not the same frequencies, the resonance frequencies are added together and hereby become more pronounced.

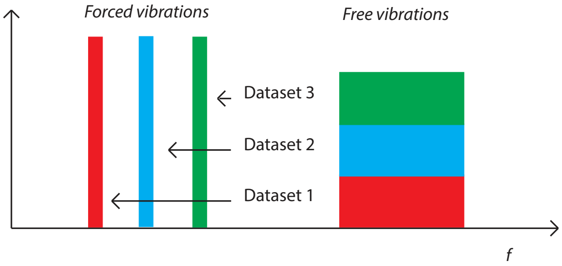

Figure 5.12: *Schematization of the summation technique presented in section 5.1. It is shown that the forced vibrations at different frequencies do not add up, but the free vibrations do add up in the frequency domain.*

Regarding the measured transmissibility functions the following can be noted:

Transmissibillity functions

An interpretation is given to both figures 5.10 and 5.11 and to the obtained parameters of table 5.5.

- The transmissibility functions obtained with the vibration model are considered accurate in vertical direction. In graph $\ddot{Z}_2(\omega)/\ddot{Z}_1(\omega)$ and $\ddot{Z}_3(\omega)/\ddot{Z}_2(\omega)$ clear peaks can be found that have an amplification factor up to 5. In graph $\ddot{Z}_4(\omega)/\ddot{Z}_3(\omega)$ less clear behavior is shown and there is not much amplification occurring, it is assumed that this is because sensor 4 is located close to the main hinge of the cutter ladder, and therefore vibrates less than the other sensors.
- In functions $\ddot{Z}_4(\omega)/\ddot{Z}_3(\omega)$ and $\ddot{Y}_3(\omega)/\ddot{Y}_2(\omega)$ the modeled transmissibility is more of a trend line than accurately predicting the small peaks, it is assumed that the vibration model is not detailed enough to describe these small effects.

- The results of the horizontal transmissibility as shown in figure 5.6, both $\ddot{Y}_2(\omega)/\ddot{Y}_1(\omega)$ and $\ddot{Y}_3(\omega)/\ddot{Y}_2(\omega)$ show not very clear behavior. A strong amplification between motion $\ddot{Y}_1(\omega)$ and $\ddot{Y}_2(\omega)$ in the frequency range of $f = 0 - 2\,\mathrm{Hz}$ seems to occur, when looking into figure 5.3 the total vibration is very low compared to the range of $f = 4 - 8\,\mathrm{Hz}$, and should therefore be seen as not that relevant. It should be mentioned that between sensor $\ddot{Y}_1(\omega)$ and $\ddot{Y}_1(\omega)$ a swing wire is located which introduces forcing to the spectrum which pollutes the transmissibility of the vibrations between these sensors.

- Regarding the values presented in table 5.5, the water added in vertical direction is predicted quite well. By decreasing the water added mass to $\approx 90\,\%$ of the initial estimated amount, the peak shift leftwards to the most accurate value.

- The amount of water added mass in vertical direction had to be reduced to $\approx 40\,\%$ of the estimated amount of water added mass. It is of course questionable whether this value really does mean much, as the modeled functions show quite some deviation from the measured transmissibility functions. It should be mentioned that varying stiffness parameters k_{y1} and $k_{\psi 1}$ had much more influence on reducing the difference between modeled and measured transmissibility functions.

5.2 Motion prediction method

A method is set up to show that the model predicts the cutter ladder behavior accurate. Again use is made of the transfer matrix $\mathbf{T_a}(\omega)$ as defined per equation 5.14. This method predicts the motions of the cutter ladder using motions of the surrounding sensors as input. The method is applied to obtain results in vertical and horizontal directions. The results are given in section 5.2.3.

Used data

For the input motions, the same method as described in section 5.1 is used up to equation 5.3. Because the motions are now used as an input for model, the phase should be taken into account as well. Therefore equations 5.25 and 5.26 apply. It should be noted that it is again chosen to look at the behavior of the model based on all 22 datasets. Reason behind this is that in this case the dynamics of the cutter ladder are more pronounced. In case only one dataset is used, one mainly looks at the response of the cutter ladder to the forced vibrations at one excitation frequency.

$$\ddot{Z}_n(\omega) = \sum_{d=1}^{22} \mathfrak{F}(\ddot{Z}_n(t))_d \tag{5.25}$$

$$\ddot{Y}_n(\omega) = \sum_{d=1}^{22} \mathfrak{F}(\ddot{Y}_n(t))_d \tag{5.26}$$

To show that the model also predict the motions correctly of only one dataset, results are presented of the method are presented for dataset 14 in appendix C.3.

5.2.1 Vertical motion

The method is explained using figure 5.13, where the motions of the cutter in vertical direction and the rotation around the local y-axis of the nodes are given. Each of the vertical motions is predicted using two input motions, this is defined in figure 5.13 where the predicted motion is indicated by the arrow and the used motions are indicated by the two connected dots.

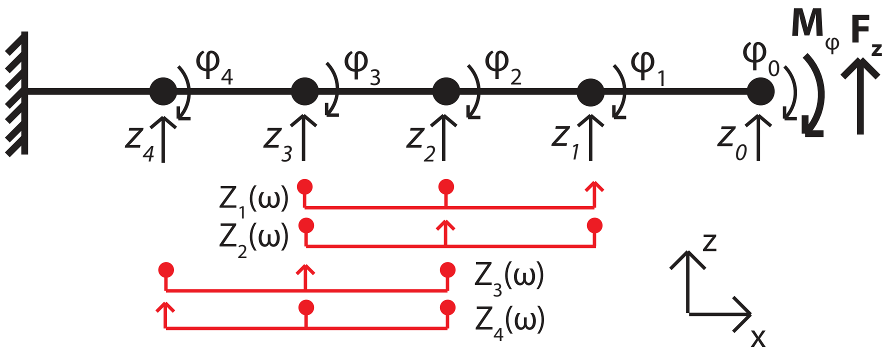

Figure 5.13: *Schematic of the transmissibility approach in vertical direction. The dots of the red indicators represent the inputs used for the output indicated with the arrow as mentioned in equations 5.31 - 5.34*

In equation 5.27 matrix $\mathbf{T_a}(\omega)$ is defined for figure 5.13, Where it is again assumed that loading only occurs at the tip of beam where the cutter head is located.

$$\begin{bmatrix} T_{11} & T_{12} & T_{13} & T_{14} & \dots & T_{1-10} \\ T_{21} & T_{22} & T_{23} & T_{24} & \dots & T_{2-10} \\ T_{31} & T_{32} & T_{33} & T_{34} & \dots & T_{3-10} \\ T_{41} & T_{42} & T_{43} & T_{44} & \dots & T_{4-10} \\ \vdots & \vdots & \vdots & \vdots & \ddots & \vdots \\ T_{10-1} & T_{10-2} & T_{10-3} & T_{10-4} & \dots & T_{10-10} \end{bmatrix} \begin{bmatrix} F_z \\ M_\varphi \\ 0 \\ 0 \\ \vdots \\ 0 \end{bmatrix} = \begin{bmatrix} \ddot{z}_0 \\ \ddot{\varphi}_0 \\ \ddot{z}_1 \\ \ddot{\varphi}_1 \\ \vdots \\ \ddot{\varphi}_4 \end{bmatrix} \tag{5.27}$$

Just as in section 5.1.2, most of the terms in the force vector are zero, hence matrix 5.27 can be reduced to matrix 5.28, for the four vertical motions.

$$\begin{bmatrix} T_{31} & T_{32} \\ T_{51} & T_{52} \\ T_{71} & T_{72} \\ T_{91} & T_{92} \end{bmatrix} \begin{bmatrix} F_z \\ M_\varphi \end{bmatrix} = \begin{bmatrix} \ddot{z}_1 \\ \ddot{z}_2 \\ \ddot{z}_3 \\ \ddot{z}_4 \end{bmatrix} \tag{5.28}$$

Linear combinations can be obtained from equation 5.28 by creating subsets. Equations 5.29 and 5.30 are given as an example.

$$\begin{bmatrix} T_{31} & T_{32} \\ T_{51} & T_{42} \end{bmatrix} \begin{bmatrix} F_z \\ M_\varphi \end{bmatrix} = \begin{bmatrix} \ddot{z}_1 \\ \ddot{z}_2 \end{bmatrix} \tag{5.29}$$

$$\begin{bmatrix} T_{71} & T_{72} \\ T_{91} & T_{92} \end{bmatrix} \begin{bmatrix} F_z \\ M_\varphi \end{bmatrix} = \begin{bmatrix} \ddot{z}_3 \\ \ddot{z}_4 \end{bmatrix} \tag{5.30}$$

By solving the equations for the force vector, a Multiple Input Multiple Output (MIMO) system is created capable of predicting vibrations at two output locations, based on two input locations as in equation 5.31 - 5.34. It is not possible to use for example three inputs to determine one output as it is required to use a square matrix to be able to invert it. An individual equation is obtained for each of the four motions, Hence equations 5.31 - 5.34. It has been chosen to use an individual calculation for each of the motions to be consistent in the approach.

$$\begin{bmatrix} T_{31} & T_{32} \\ T_{91} & T_{92} \end{bmatrix} \begin{bmatrix} T_{51} & T_{52} \\ T_{71} & T_{72} \end{bmatrix}^{-1} \begin{bmatrix} \ddot{z}_2 \\ \ddot{z}_3 \end{bmatrix} = \begin{bmatrix} \ddot{\mathbf{Z}}_\mathbf{1} \\ \ddot{z}_4 \end{bmatrix} \tag{5.31}$$

$$\begin{bmatrix} T_{51} & T_{52} \\ T_{91} & T_{92} \end{bmatrix} \begin{bmatrix} T_{31} & T_{32} \\ T_{71} & T_{72} \end{bmatrix}^{-1} \begin{bmatrix} \ddot{z}_1 \\ \ddot{z}_3 \end{bmatrix} = \begin{bmatrix} \ddot{\mathbf{Z}}_\mathbf{2} \\ \ddot{z}_4 \end{bmatrix} \tag{5.32}$$

$$\begin{bmatrix} T_{71} & T_{72} \\ T_{91} & T_{92} \end{bmatrix} \begin{bmatrix} T_{31} & T_{32} \\ T_{51} & T_{52} \end{bmatrix}^{-1} \begin{bmatrix} \ddot{z}_1 \\ \ddot{z}_2 \end{bmatrix} = \begin{bmatrix} \ddot{\mathbf{Z}}_\mathbf{3} \\ \ddot{z}_4 \end{bmatrix} \tag{5.33}$$

$$\begin{bmatrix} T_{91} & T_{92} \\ T_{31} & T_{32} \end{bmatrix} \begin{bmatrix} T_{71} & T_{72} \\ T_{51} & T_{52} \end{bmatrix}^{-1} \begin{bmatrix} \ddot{z}_3 \\ \ddot{z}_2 \end{bmatrix} = \begin{bmatrix} \ddot{\mathbf{Z}}_\mathbf{4} \\ \ddot{z}_1 \end{bmatrix} \tag{5.34}$$

Results of the obtained motions are given in section 5.2.3.

5.2.2 Horizontal motion

As shown in figure5.1 only three sensors are available for the horizontal motion. The transfer matrix can be written out for the motion in horizontal direction as in equation 5.35 and can be reduced to equation 5.36.

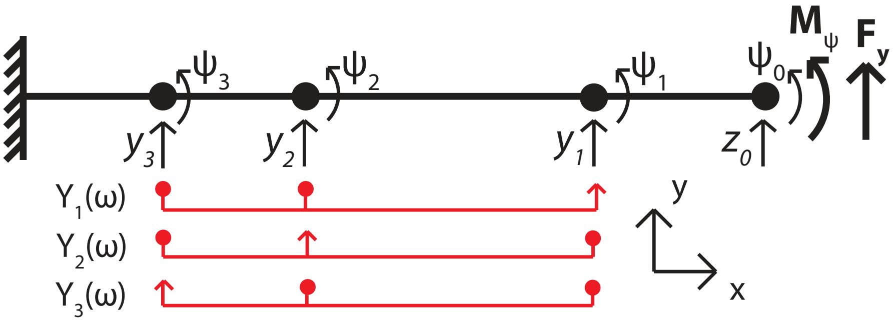

Figure 5.14: *Schematic of the transmissibility approach in vertical direction. The dots of the red indicators represent the inputs used for the output indicated with the arrow as mentioned in equations 5.31 - 5.34*

$$\begin{bmatrix} T_{11} & T_{12} & T_{13} & T_{14} & \dots & T_{18} \\ T_{21} & T_{22} & T_{23} & T_{24} & \dots & T_{28} \\ T_{31} & T_{32} & T_{33} & T_{34} & \dots & T_{38} \\ T_{41} & T_{42} & T_{43} & T_{44} & \dots & T_{48} \\ \vdots & \vdots & \vdots & \vdots & \ddots & \vdots \\ T_{81} & T_{82} & T_{83} & T_{84} & \dots & T_{88} \end{bmatrix} \begin{bmatrix} F_y \\ M_\psi \\ 0 \\ 0 \\ \vdots \\ 0 \end{bmatrix} = \begin{bmatrix} \ddot{y}_0 \\ \ddot{\psi}_0 \\ \ddot{y}_1 \\ \ddot{\psi}_1 \\ \vdots \\ \ddot{\psi}_3 \end{bmatrix} \tag{5.35}$$

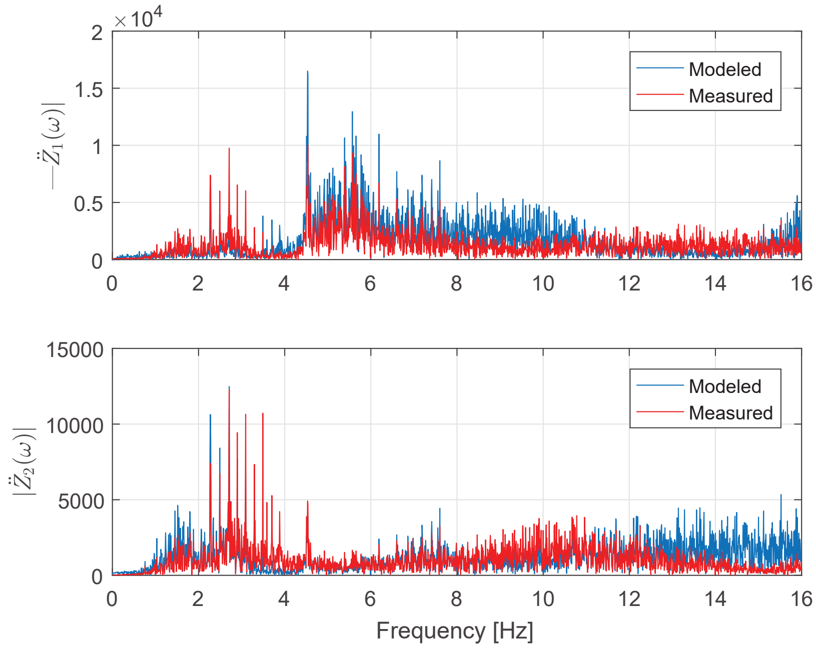

Figure 5.15: *Motions in vertical direction $\ddot{Z}_1(\omega)$ and $\ddot{Z}_2(\omega)$ predicted using the MIMO method.*

$$\begin{bmatrix} T_{31} & T_{32} \\ T_{51} & T_{52} \\ T_{71} & T_{72} \end{bmatrix} \begin{bmatrix} F_y \\ M_\psi \end{bmatrix} = \begin{bmatrix} \ddot{y}_1 \\ \ddot{y}_2 \\ \ddot{y}_3 \end{bmatrix} \tag{5.36}$$

The three combinations for obtaining the horizontal motions as shown in figure are obtained in the same manner as in section 5.2.1, Hence equations 5.37 - 5.39.

$$\begin{bmatrix} T_{31} & T_{32} \end{bmatrix} \begin{bmatrix} T_{71} & T_{72} \\ T_{91} & T_{92} \end{bmatrix}^{-1} \begin{bmatrix} \ddot{y}_2 \\ \ddot{y}_3 \end{bmatrix} = \begin{bmatrix} \ddot{\mathbf{Y}}_1 \end{bmatrix} \tag{5.37}$$

$$\begin{bmatrix} T_{51} & T_{52} \end{bmatrix} \begin{bmatrix} T_{31} & T_{32} \\ T_{71} & T_{72} \end{bmatrix}^{-1} \begin{bmatrix} \ddot{y}_1 \\ \ddot{y}_3 \end{bmatrix} = \begin{bmatrix} \ddot{\mathbf{Y}}_2 \end{bmatrix} \tag{5.38}$$

$$\begin{bmatrix} T_{71} & T_{72} \end{bmatrix} \begin{bmatrix} T_{31} & T_{32} \\ T_{51} & T_{52} \end{bmatrix}^{-1} \begin{bmatrix} \ddot{y}_1 \\ \ddot{y}_2 \end{bmatrix} = \begin{bmatrix} \ddot{\mathbf{Y}}_3 \end{bmatrix} \tag{5.39}$$

5.2.3 Results

Results of the motion prediction method in both horizontal and vertical direction are given in figures 5.15 - 5.17, where the magnitudes are shown.

5.2.4 Interpretation

Results of the motion prediction method are found to be accurate for most of the shown motions. It should be mentioned that in an earlier stage of the project some resonance peaks used to show

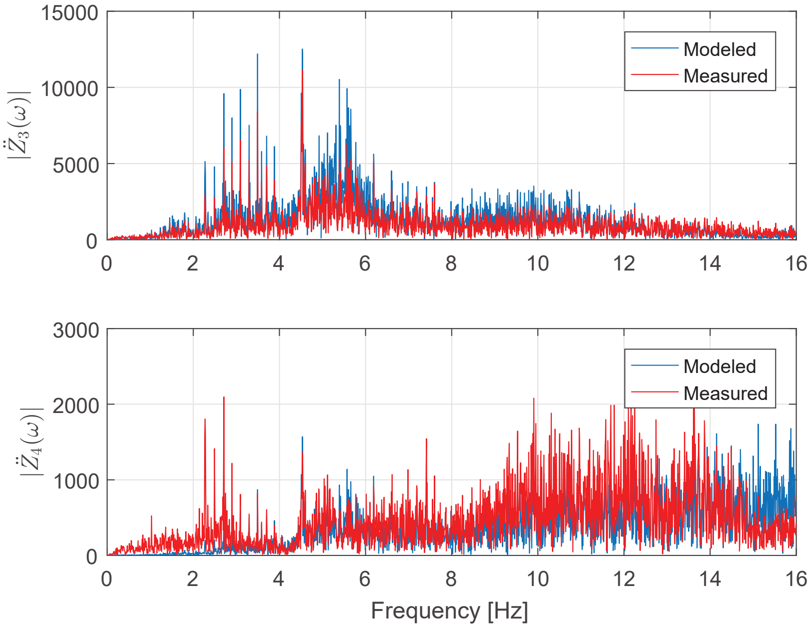

Figure 5.16: *Motions in vertical direction $\ddot{Z}_3(\omega)$ and $\ddot{Z}_4(\omega)$ predicted using the MIMO method.*

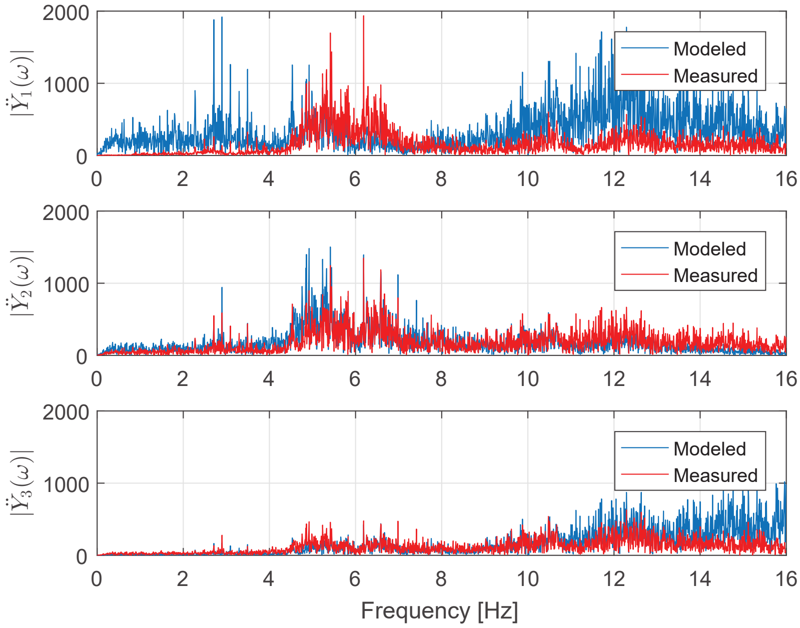

Figure 5.17: *Motions predicted in horizontal direction using the MIMO method.*

up in the graphs. After updating the model these became less pronounced. Of course deviations are still shown in all graphs. Reasons for these deviations can in most cases be sought for in the errors between the modeled and measured transmissibility functions. Once these are even further reduced, a higher accuracy in the motions can be obtained. It should be mentioned that multiple methods have been investigated, but using the sensors most closely to the predicted motions was found to give the most accurate result.

5.3 Discussion

A method is presented in this chapter to compare the characteristics of the vibration model to the data obtained during measurements on the cutter ladder. While performing this approach, the interpretation as given in section 5.1.5 was discovered. As shown in figure 5.2, twenty-two datasets had to be added together to be able to find free vibrations at the same magnitude as the forced vibrations of one dataset (the spikes of the forced vibrations are in the same range as the summation the free vibrations as schematized in figure 5.12). It is therefore assumed that the free vibrations of the cutter ladder are relatively low compared to the forced vibrations. The relatively high damping caused by the surrounding water found in section 5.1.4 is assumed to be the cause for the low free vibrations of the cutter ladder. The question is hereby raised whether free vibrations could add significantly to the occurring damage of the structure. The reasoning above hereby approximates answering the main question: could resonance of the global cutter ladder structure be a cause for damage to the cutter ladder? The answer to this question is: probably not because the free vibrations are not substantial compared to the forced vibrations.

The consequence of the discovery is quite positive for Royal Boskalis as it suggests that additional material stresses due to vibration amplification at resonance frequencies is probably small. This would mean that the current quasi-static approach of determining the structural strength of the cutter ladders is probably accurate. The author is still a bit hesitant to put this insight in the conclusions as full disclosure can not be given. It is therefore necessary to identify material stresses and compare these to finite element modeling.

Chapter 6

Conclusion and recommendations

An identification of the dynamic behavior of the CSD Taurus II cutter ladder is performed within this thesis. Both the investigation on the data from the measurements and the development of the vibration model led to new insights. Within this chapter, conclusions regarding the followed methods and the obtained results are drawn. Recommendations are given for further development.

6.1 Conclusions

The Operational Modal Analysis did not yield the results initially preferred, but it did give insight into the dynamic behavior of the cutter ladder in operating conditions. Using the OMA, it was discovered that the vibrations of the cutter ladder are dominated by the forced vibrations caused by the cutting process. The results presented show that the dominant vibration frequency of the cutter ladder can be easily determined using the rotational speed of the cutter head, and number of blades on the cutter head. The frequency domain decomposition method is therefore concluded to be a useful approach for identification of dynamic behavior of a structure as it allows one to combine the frequency responses of a large amount of data. It should however be mentioned that the method asks for quite an understanding of signal analysis and linear algebra, the interpretation of the results can therefore be tricky.

A vibration model has been developed using finite beam elements and a MATLAB finite element toolbox. A Detailed finite element model has been simplified to a beam element model that describes only global vibrations of the cutter ladder. The simplified model is compared to the detailed finite element model by comparing modal analysis results, which showed that the simplification of the detailed finite element model is performed correctly.

In a quite late stage of the project it was discovered that shear deflection has a relatively high influence on the total ladder deflection. Reason behind this is the open hull structure which gives the cutter ladder a high bending stiffness. It has was therefore chosen to lower the stiffness of the cutter ladder elements such the vibration model gave better results in modal analysis comparison.

It should be mentioned that quite some time has been spent in developing a simplified model by first identifying all stiffness, mass and dimensional parameters, as this was required for the implementation into MATLAB. This would have probably been easier when a more graphical finite element package would have been used. MATLAB on the other hand is easy to handle at the boundary of data analysis and modeling.

While progressing with the project, a solution had to be found to be able to verify the vibration model with the data from the measurements. The methods presented in chapter 5 was found to produce the most viable approach. By comparison of transmissibility functions it was possible to both validate the vibration model using using only information obtained the measurements, and obtain knowledge about the influence of water surrounding the structure. It was chosen to use the transmissibility functions as design parameters, because these showed the actual dynamic behavior of the cutter ladder without the forced vibrations. This made it possible to easily update the model by varying dynamic parameters such as added mass, damping and stiffness. The motion prediction method was set up as a more easy to interpret method to show that the vibration model is capable of predicting the vibrations measured in the cutter ladder. It is concluded that the transmissibility function approach is capable of obtaining accurate results in case the no external loads are applied in the real life structure, as this seems to introduce inaccuracies, as can be found in transmissibility function $\ddot{Y}_2(\omega)/\ddot{Y}_1(\omega)$.
based on the obtained model and the identification of the updating parameters, it can be concluded that the added mass significantly influences the behavior of the structure, as a large amount of water had to be accounted for to correct the dry dynamic behavior of the cutter ladder to a submerged condition. The percentage of damping introduced is also found to be significant. The water included and surrounding the structure is found to be responsible for both the added mass and damping. Usually $\approx 2-3\,\%$ of damping within a structure comes from material damping. The other $\approx 4-5\,\%$ of the damping is therefore identified as being caused by the water in and outside of the cutter ladder. The high damping is assumed to be the cause for the low resonance of the structure.

6.2 Recommendations

Having a new cutter suction dredger of even greater dimensions put to work in 2017, new opportunities for investigating cutter ladders arise. For various topics identified within this thesis there was no time available anymore or the investigation was out of the scope of this project, some of them are elaborated below.

Based on the discussion of section 5.3 it is suggested to perform a comparable measurement campaign on the new cutter ladder. It is then suggested to include more sensors in the measurements, including strain gages such that material stresses can be determined. Material stresses can be verified using finite element modeling. In case the theory presented in section 5.3 holds, finite element modeling in a quasi static approach should yield accurate results.

Because a real cause for the cracks found in the structure has not been presented, next topic to look at could be fatigue. It should first be mentioned that the structure of interest has been built in 1983 and has been operated ever since. After such a long period, combined with the identified harmonic forcing, it is reasonable that damage due to fatigue occurs. One of the locations where cracks were found was between plates of the hull and the girders. It is suggested that the harmonic forces in combination with the water surrounding the hull plates might cause high fatigue loads on its welds. Investigation of fatigue on a local level can probably give insight in failure mechanisms of the cutter ladder.

As mentioned in the introduction, it was initially proposed to develop a load model, which would be used to apply loads to the cutter ladder model, with which the vibrations could be created in the cutter ladder. This approach was eventually canceled as it unnecessarily introduced uncertainties to the modeling. Now that a validated vibration model has been obtained it could be possible to use the model to identify the loads occurring at the cutter head. Identification of loads at a cutter head has already been performed by modeling the cutter teeth - soil interaction in an earlier study Boorsma [1] in which still a deviation was found between measured and modeled loads. Identifying loads in a dynamic manner might close this gap.

Bibliography

[1] [redacted] Internal reporting royal boskalis. Master's thesis, 2013.

[2] R. Brincker, L. Zhang, and P. Andersen. Modal identification of output-only systems using frequency domain decomposition. *Smart Materials and structures*, 10:441–445, 2001.

[3] Techno Fysica B.V. Vibration investigation - cutting rock measurement report, note: Internal reporting royal boskalis. Technical Report 70195, 2015.

[4] [redacted] Internal reporting royal boskalis. Technical Report 14147 R01, 2015.

[5] [redacted] Internal reporting royal boskalis. Technical Report 51580RKe15413, 2015.

[6] G.R. Cowper. The shear coefficient in timoshenko's beam theory. *Transactions of the American Society of Mechanical Engieeers, Journal of Applied Mechanics*, 33:335–340, 1966.

[7] F.M. Dekking, C. Kraaikamp, H.P. Lopuhaa, and L.E. Meester. *A Modern Introduction to Probability and Statistics.* Springer Science, 2005.

[8] *Introduction to Aerospace Structures, ASEN 3112, Course material.* Department of Aerospace Engineering Sciences, University of Colorado at Boulder, `http://www.colorado.edu/engineering/CAS/courses.d/Structures.d/Home.html`, . Chapter 22.

[9] *Matrix Finite Element Method in Dynamics Course material.* Department of Aerospace Engineering Sciences, University of Colorado at Boulder, `http://www.colorado.edu/engineering/CAS/courses.d/MFEMD.d/Home.html`, . Chapter 4, 16, 18.

[10] *DNV-RP-H103 Modeling and Analysis of Marine Operations.* Det Norske Veritas, april 2011.

[11] Christof Devriendt, Flavio Presezniak, Gert De Sitter, Katy Vanbrabant, Tim De Troyer, Steve Vanlanduit, and Patrick Guillaume. Structural health monitoring in changing operational conditions using tranmissibility measurements. *Shock and Vibration*, 17(4-5):651–675, 2010.

[12] D. Dooms, M. Jansen, G. De Roeck, G. Degrande, G. Lombaert, M. Schevenels, and S. Francois. *StaBIL: A finite element toolbox for Matlab.* Katholieke Universiteit Leuven, 2.0 edition, 2010.

[13] Carlos A. Felippa. *Introduction to Finite Element Methods.* University of Colorado at Boulder, 2004.

[14] H. Gavin. *Geometric StiffnessEffects in 2D and 3D Frames*. Departement of Civil and Environmental Engineering, Duke University, 2012. Lecture notes Matrix Structural Analysis.

[15] R. C. Hibbeler. *Mechanics of Materials*, volume 6. Pearson Prentice Hall, 2005.

[16] E. Kamen and B. Heck. *Fundamentals of signals and systems Using the web and matlab*. Pearson Prentice Hall, 2007.

[17] D. Lay. *Linear Algebra and Its Applications*, volume 3. Pearson Prentice Hall, 2006.

[18] V. Meruane. Model updating using antiresonant frequencies identified from transmissibility functions. *Journal of Sound and Vibration*, 332(4):807–820, 2013.

[19] Royal Boskalis Westminster N.V. *Equipment sheet Taurus II self-propelled seagoing cutter suction dredger*. `http://www.boskalis.nl/uploads/media/TaurusII_02.pdf`.

[20] Przemieniecki. *Theory of Matrix Structural Analysis*. McGraw-Hill, 1968.

[21] G. Steenackers, C. Devriendt, and P. Guillaume. On the use of transmissibility measurements for finite element model updating. *Journal of Sound and Vibration*, 303(3-5):707–722, 2007.

[22] [redacted] Internal reporting royal boskalis. Technical report, Royal Boskalis Westminster N.V., 2015.

[23] W.J. Vlasblom. *Introduction to Dredging Equipment*. Delft University of Technology, 2003. Lecture notes Dredging Equipment.

[24] Zhimin Wan, Shande Li, Qibai Huang, and Ting Wang. Structural response reconstruction based on the modal superposition method in the presence of closely spaced modes. *Mechanical Systems and Signal Processing*, 42(1-2):14–30, 2014.

[25] T. Yokoyama. Vibrations of a hanging timoshenko beam under gravity. *Journal of Sound and Vibration*, 141:245–258, 1990.

[26] W. C. Young and Richard G. Budynas. *Roark's Formulas for Stress and Strain*. McGraw-Hill, seventh edition edition, 2002.

Part II

Appendix

Appendix A

Appendix OMA

A.1 Sensor locations

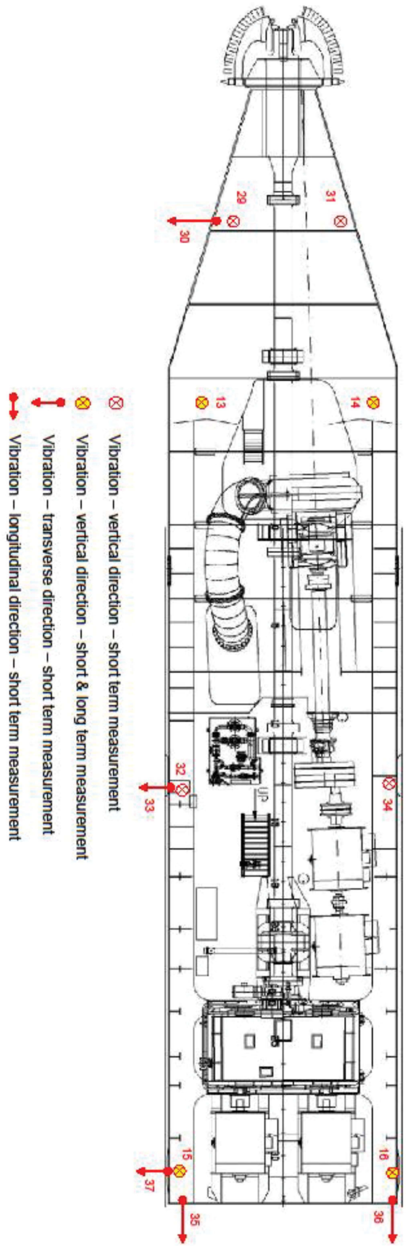

Figure A.1: *Sensor locations as mounted on the cutter ladder*

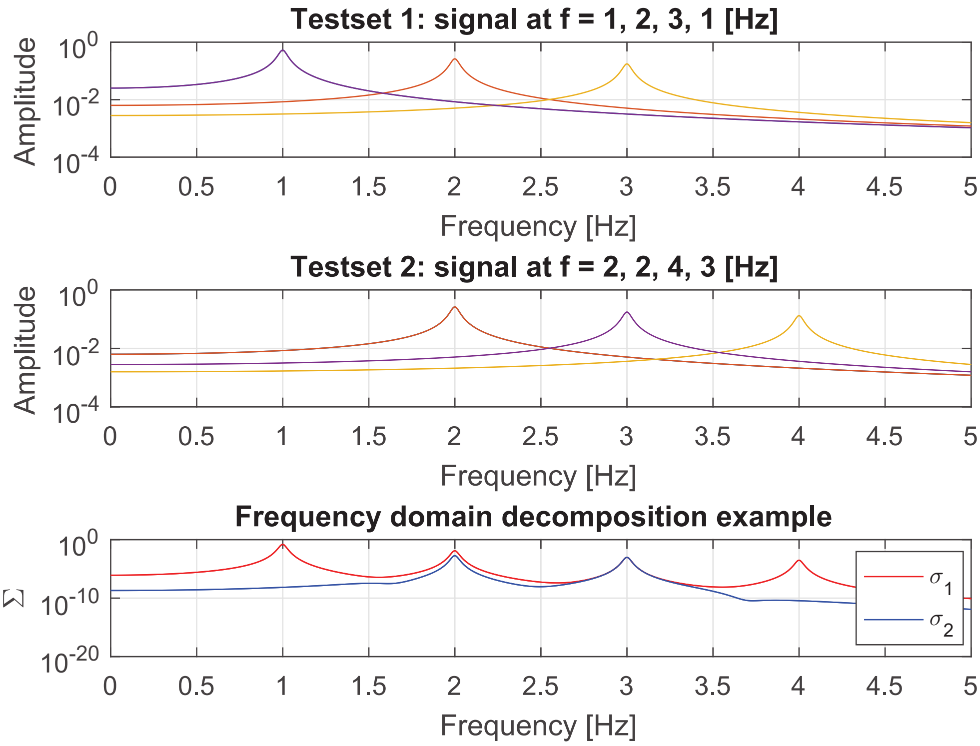

Figure A.2: *Results of the FDD example using resonance peaks instead of time domain signals*

A.2 FDD example using resonance peaks

In a quite late stage of the project it was discussed that presenting the FDD example is probably more insightful by presenting the method using resonance peaks. However, implementing this in the report would mess up the structure introduced in chapter 3, it has therefore been chosen to present these results in the appendix. The resonance frequencies from table 3.1 are implemented using equation A.1, which is an equation for a basic resonance peak.

$$d_m(\omega) = \frac{1}{-m\omega^2 + j\omega c + k} \tag{A.1}$$

A mass of $m = 1\,\mathrm{kg}$ and a damping factor of $m = 0.3\,\frac{\mathrm{s}}{\mathrm{m}}$ are chosen arbitrarily. The frequencies f_m of the table 3.1 are implemented by determining a value for k of equation A.1 using equation A.2.

$$k_m = m \cdot (2\pi f_m)^2 \tag{A.2}$$

Results are presented in figure A.2, where in the two upper graphs the input datasets are shown and in the lower graph the result of the FDD method.

A.3 Properties measurement sets

Dataset	Measurement	N_B	Speed [RPM]	f_b [Hz]
1	14	8	34	4.53
2	15	8	34	4.53
3	16	8	29	3.87
4	17	8	29	3.87
5	18	8	27	3.60
6	19	8	27	3.60
7	24	6	37	3.70
8	25	6	37	3.70
9	26	6	35	3.50
10	27	6	35	3.50
11	28	6	33	3.30
12	29	6	33	3.30
13	30	6	31	3.10
14	31	6	31	3.10
15	32	6	29	2.90
16	33	6	29	2.90
17	34	6	27	2.70
18	35	6	27	2.70
19	36	6	25	2.50
20	37	6	25	2.50
21	38	6	23	2.30
22	39	6	23	2.30

Table A.1: *Properties of all measurement sets used within this thesis report.*

A.4 Power corrected FDD

An investigation is performed identifying whether correction of the frequency domain decomposition results by a power input yields better results regarding natural frequencies of the cutter ladder. The results are corrected by the measured cutter torque multiplied by its rotational speed as in equation A.3, note that the rotational speed is kept constant within a dataset. A fourier transform is performed and the correction is determined as in equation A.5, results are given in figure A.3.

$$P(t) = T(t) \cdot \dot{\phi}_c \tag{A.3}$$

$$P(\omega) = \mathfrak{F}(P(t)) \tag{A.4}$$

$$R(\omega) = \frac{|S(\omega)|}{|P(\omega)|} \tag{A.5}$$

As shown in figure A.3, the result is almost flat, only with two anti-resonance peaks around $f \approx 4$ and 4.8 Hz. It is assumed that these peaks are caused by the two resonance peaks shown in top graph where the torque is shown. The two natural frequencies are caused by the different rotational inertia of the 6- and 8-blade cutter heads.

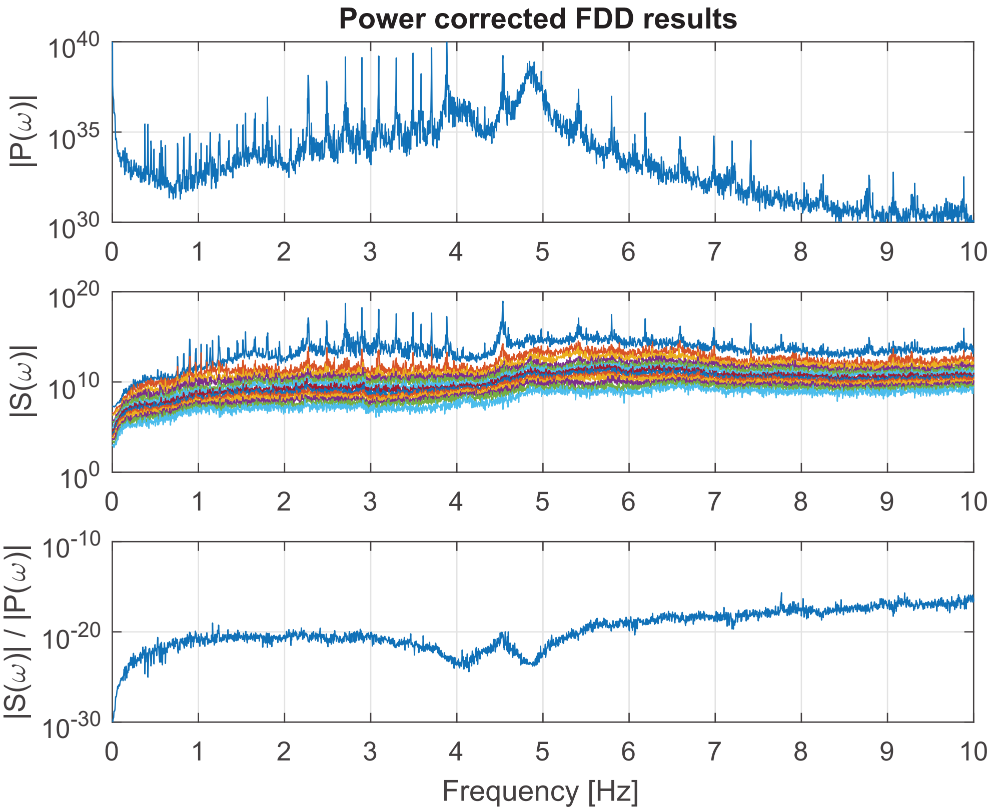

Figure A.3: *Frequency domain decomposition as performed in chapter 3.4 corrected by a power input obtained from the cutter torque and cutter speed.*

Appendix B

Vibration model properties

B.1 Cross-sectional parameters

Cross-sectional parameters are obtained using Autodesk Inventors' Regional properties tool. The tool is capable of supplying the area moment of inertia for the horizontal and vertical direction and determines the corresponding principal axes locations. The tool also supplies a value for the rotational stiffness I_{xx}, this value should neglected as it should only be used in case of a solid cross section.

B.2 Parameters obtained using CAD

The cross-sectional parameters for each of the seven sections obtained using CAD are listed below in tables B.1 - B.7. An overview of the cross sections is given by the yellow outlines in figures B.1 - B.7. It should be noted that the blue lines given in the figures are not of relevance within this thesis.

B.2.1 Section 1

Section 1 @ 2.9 [m]	
Area	$1.183m^2$
Perimeter	$127.674m$
Centroid wrt Sketch origin [m]	
X	-0.007
Y	-0.96
Inertia wrt Sketch origin[m^4]	
I_{xx}	5.131
I_{xy}	0.045
I_{yx}	0.045
I_{yy}	7.1
I_{zz}	12.231
Area moment inertia wrt principal axes [m^4]	
I_x	4.042
I_y	7.101
I_z	12.143

Table B.1: *Cross sectional parameters of section 1*

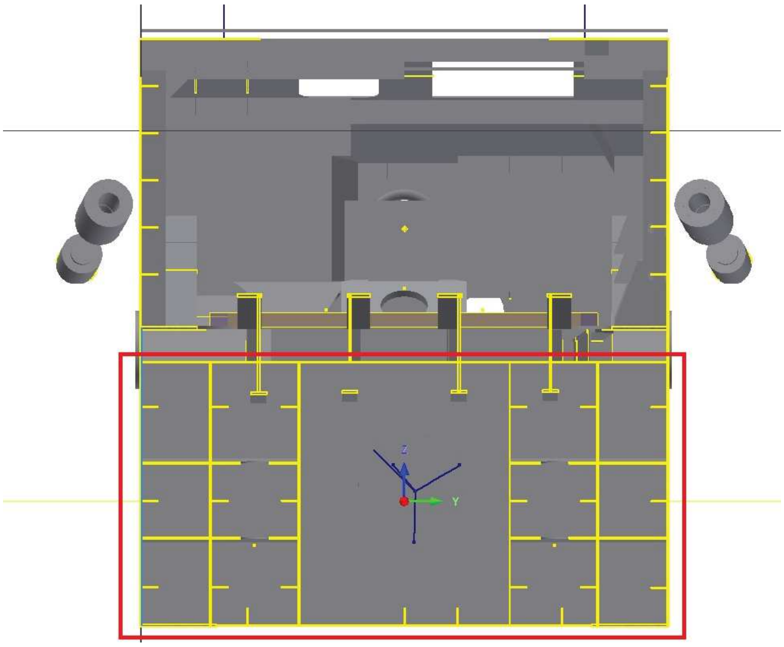

Figure B.1: *Snapshot of cross section 1 obtained using Autocad Inventor*

B.2.2 Section 2

Section 2 @ 6.83 [m]	
Area	$1.09m^2$
Perimeter	$103.257m$
Centroid wrt Sketch origin [m]	
X	1.265
Y	-0.022
Inertia wrt Sketch origin[m^4]	
I_{xx}	6.288
I_{xy}	-0.058
I_{yx}	-0.058
I_{yy}	5.332
I_{zz}	11.62
Area moment inertia wrt principal axes [m^4]	
I_x	6.288
I_y	3.587
I_z	9.875

Table B.2: *Cross sectional parameters of section 2*

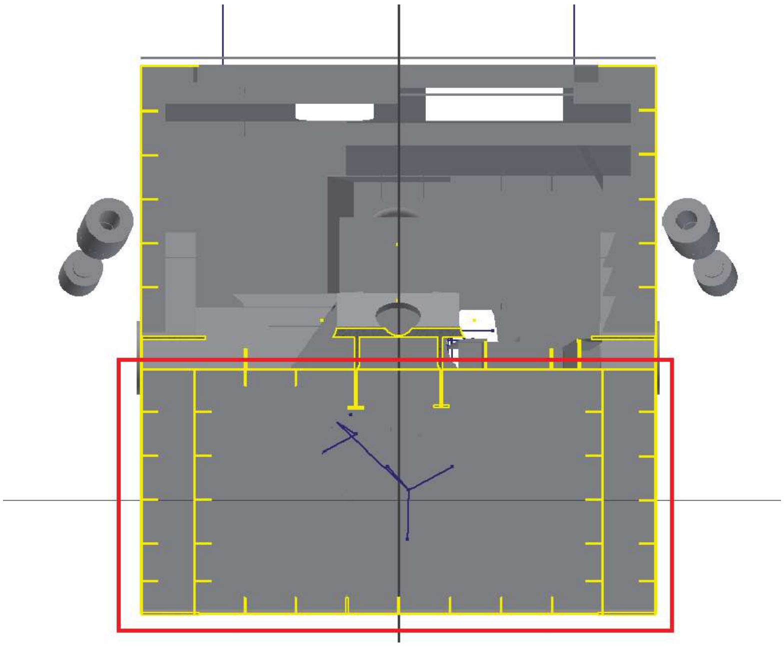

Figure B.2: *Snapshot of cross section 2 obtained using Autocad Inventor*

B.2.3 Section 3

Section 3 @ 11 [m]	
Area	$0.892m^2$
Perimeter	$99.566m$
Centroid wrt Sketch origin [m]	
X	1.346
Y	-0.103
Inertia wrt Sketch origin$[m^4]$	
I_{xx}	6.083
I_{xy}	0.117
I_{yx}	0.117
I_{yy}	4.729
I_{zz}	10.812
Area moment inertia wrt principal axes $[m^4]$	
I_x	6.093
I_y	3.093
I_y	9.186

Table B.3: *Cross sectional parameters of section 3*

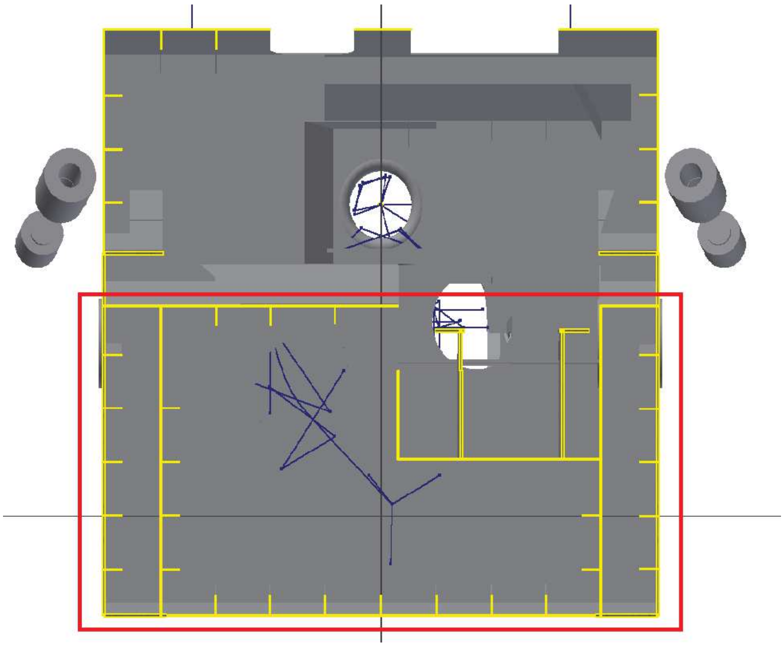

Figure B.3: *Snapshot of cross section 3 obtained using Autocad Inventor*

B.2.4 Section 4

Section 4 @ 17.528 [m]	
Area	$0.542m^2$
Perimeter	$52.708m$
Centroid wrt Sketch origin [m]	
X	-1.584
Y	0.245
Inertia wrt Sketch origin$[m^4]$	
I_{xx} 3.951	
I_{xy}	-0.114
I_{yx}	-0.114
I_{yy}	2.659
I_{zz}	6.61
Area moment inertia wrt principal axes $[m^4]$	
I_x	3.922
I_y	1.295
I_z	5.216

Table B.4: *Cross sectional parameters of section 4*

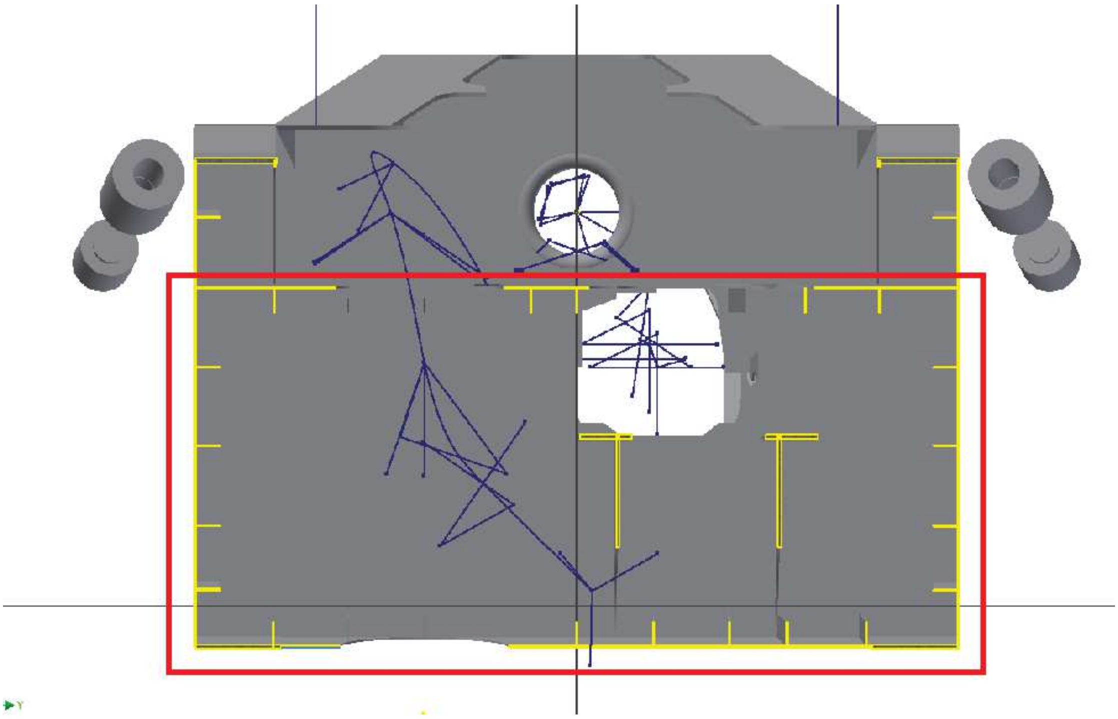

Figure B.4: *Snapshot of cross section 4 obtained using Autocad Inventor*

B.2.5 Section 5

Section 5 @ 23.158[m]	
Area	$0.505m^2$
Perimeter	$49.896m$
Centroid wrt Sketch origin [m]	
X	
Y	
Inertia wrt Sketch origin$[m^4]$	
I_{xx}	3.799
I_{xy}	0.026
I_{yx}	0.026
I_{yy}	2.858
I_{zz}	6.657
Area moment inertia wrt principal axes $[m^4]$	
I_x	3.8
I_y	1.157
I_z	4.957

Table B.5: *Cross sectional parameters of section 5*

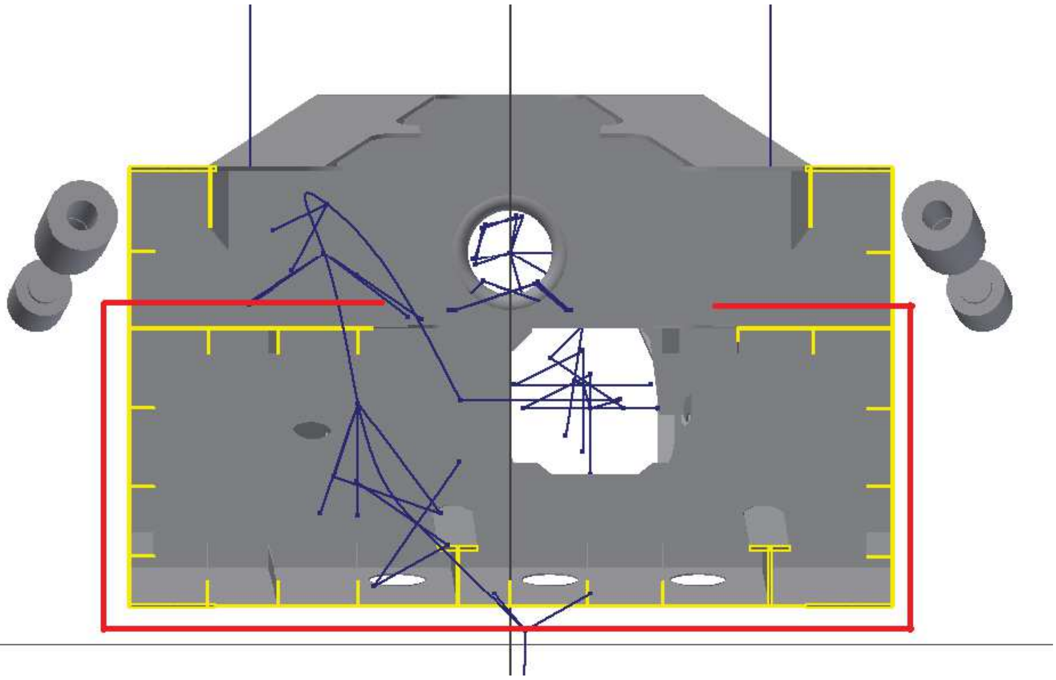

Figure B.5: *Snapshot of cross section 5 obtained using Autocad Inventor*

B.2.6 Section 6

Section 6 @ 27.9 [m]	
Area	$0.777 m^2$
Perimeter	$52.191 m$
Centroid wrt Sketch origin [m]	
X	-2.48
Y	-0.02
Inertia wrt Sketch origin[m^4]	
I_{xx}	3.5
I_{xy}	0.034
I_{yx}	0.034
I_{yy}	5.691
I_{zz}	9.195
Area moment inertia wrt principal axes [m^4]	
I_x	3.504
I_y	0.9
I_z	4.405

Table B.6: *Cross sectional parameters of section 6*

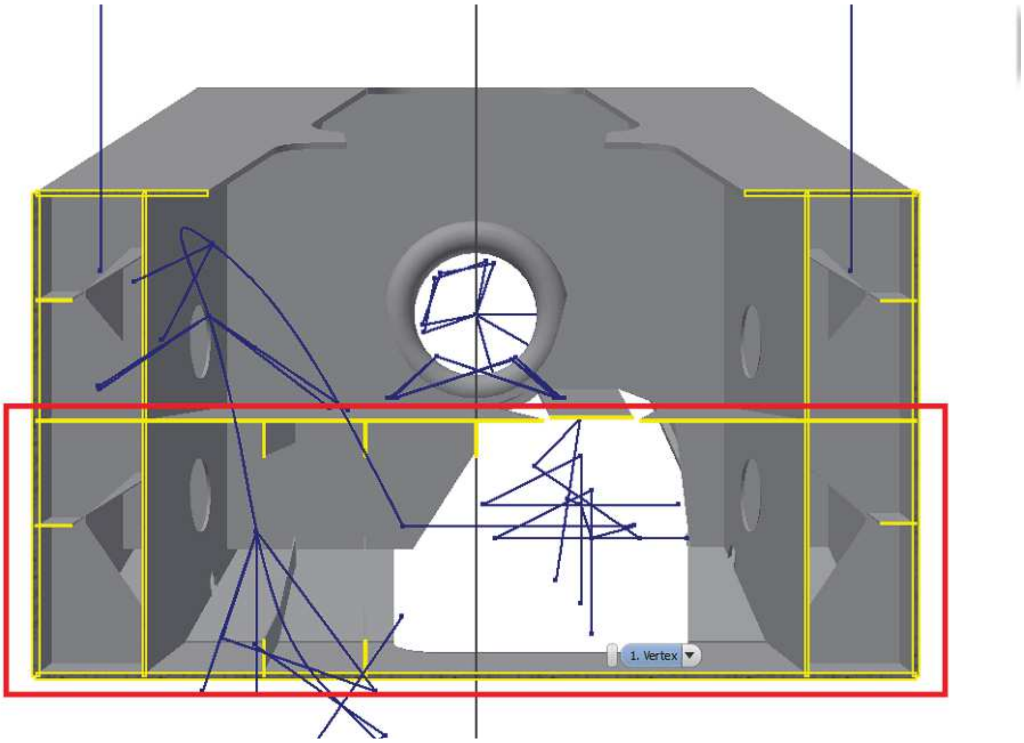

Figure B.6: *Snapshot of cross section 6 obtained using Autocad Inventor*

B.2.7 Section 7

Section 7 @ 32.5 [m]	
Area	$0.867m^2$
Perimeter	$28.8m$
Centroid wrt Sketch origin [m]	
X	-3.768
Y	-0.067
Inertia wrt Sketch origin[m^4]	
I_{xx}	0.505
I_{xy}	0.173
I_{yx}	0.173
I_{yy}	12.62
I_{zz}	13.125
Area moment inertia wrt principal axes [m^4]	
I_x	0.512
I_y	0.308
I_z	0.82

Table B.7: *Cross sectional parameters of section 7*

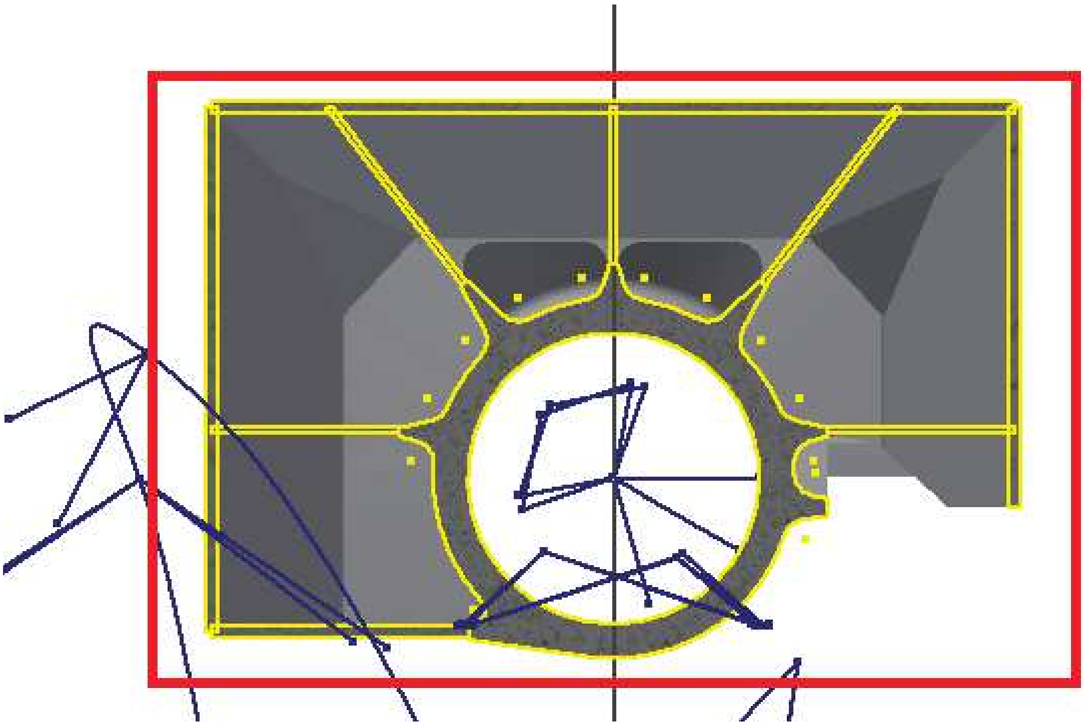

Figure B.7: *Snapshot of cross section 7 obtained using Autocad Inventor*

B.3 Rotational stiffness

Section	t [m]	t_1 [m]	a [m]	b [m]	J [m^4]
1	0.02	0.016	6.75	3.37	1.73
2	0.02	0.016	6.75	3.35	1.71
3	0.02	0.016	6.75	3.45	1.80
4	0.02	0.016	6.75	3.18	1.57
5	0.02	0.016	6.7	2.45	0.98
6	0.042	0.042	5.44	1.6	0.85
7	0.042	0.042	2.8	1.86	0.46

Table B.8: *Rotational stiffness per section, with used parameters as defined in figure 4.3*

B.4 Shear deflection calculation

An investigation is performed into the influence of the shear deflection in comparson to the bending deflection. A schematization is given in figure B.8 where the total deflection is determined per equation B.1.

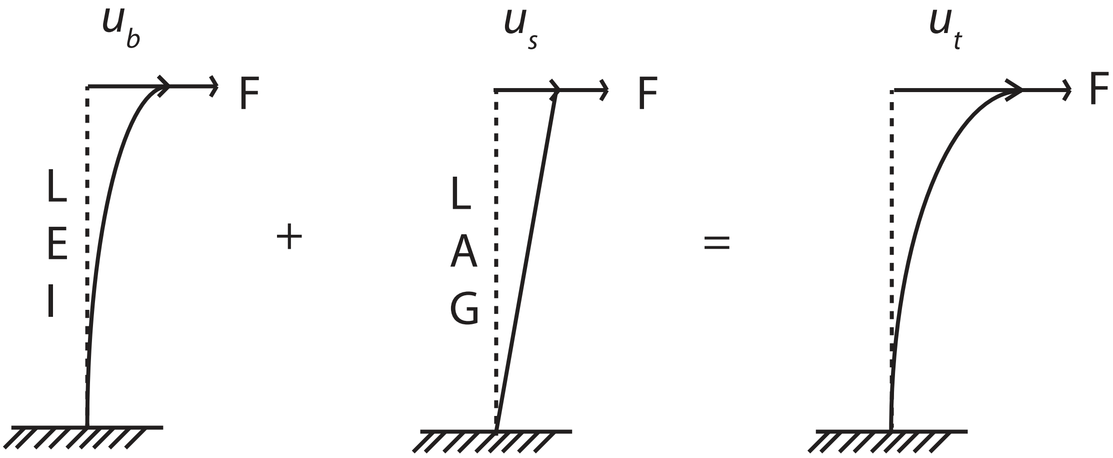

Figure B.8: *Schematization of comparison made between shear and bending deflection due to a generalized load, where u_b is the deflection due to bending,u_s is the deflection due to shear and u_t is the total deflection.*

$$u_d = u_b + u_s \tag{B.1}$$

Filling in the correct terms for u_b and u_s one obtains equation B.2.

$$u_t = \frac{FL^3}{3EI} + \frac{FL}{AG} \tag{B.2}$$

A generalized load $F = 1\,\text{N}$, a Youngs' modulus of $E = 210\,\text{GPa}$ and a shear modulus $G = 80\,\text{GPa}$ are used. Next, the deflections for u_b, u_s, u_t and ratio $^{u_b}/_{u_t}$ are obtained in tables B.9 and B.10.

Section	L [m]	A [m^2]	I_z [m^4]	u_b [m]	u_s [m]	u_d, y [m]	$^{u_b}/_{u_t}$ [m]
1	3.785	1.18	7.154	1.20E-11	3.97E-11	5.17E-11	0.23
2	3.2	1.09	6.288	8.27E-12	3.63E-11	4.46E-11	0.19
3	6	0.89	6.15	5.57E-11	8.35E-11	1.39E-10	0.40
4	7.5	0.542	3.905	1.71E-10	1.71E-10	3.43E-10	0.50
5	4.3	0.505	3.861	3.27E-11	1.05E-10	1.38E-10	0.24
6	4.2	0.777	3.5	3.36E-11	6.69E-11	1.01E-10	0.33
7	5	0.867	0.303	6.55E-10	7.14E-11	7.26E-10	0.90

Table B.10: *Used parameters and deflections per section in horizontal direction*

Section	L [m]	A [m^2]	I_y [m^4]	u_b [m]	u_s [m]	u_d, z [m]	$^{u_b}/_{u_t}$ [m]
1	3.785	1.18	4	2.15E-11	3.97E-11	6.12E-11	0.35
2	3.2	1.09	3.587	1.45E-11	3.63E-11	5.08E-11	0.29
3	6	0.89	3.152	1.09E-10	8.35E-11	1.92E-10	0.57
4	7.5	0.542	1.238	5.41E-10	1.71E-10	7.12E-10	0.76
5	4.3	0.505	1.129	1.12E-10	1.05E-10	2.17E-10	0.51
6	4.2	0.777	0.9	1.31E-10	6.69E-11	1.98E-10	0.66
7	5	0.867	0.512	3.88E-10	7.14E-11	4.59E-10	0.84

Table B.9: *Used parameters and deflections per section in vertical direction*

B.5 Component Mass moment of inertia

Component	Mass M_c [mT]	Distance d [m]	I_c [mTm^2]
Section 1			
E-motor 2x	25.4	3	228.6
Total	25.4		228.6
Section 2			
Gear box	87.0	2.4	501.1
Total	87.0		501.1
Section 3			
E-motor Pmp	12.7	2	50.8
Extra E-motor+ foundation	14.7	2	58.8
Stuwblok	13.4	2.1	59.0
Total	40.8		168.6
Section 4			
pomp twk	12.5	1	12.5
Total	12.5		12.5
Section 5			
Onderwaterpomp	37.3	0.5	9.3
Persleiding	10.0	0.5	2.5
Total	47.3		11.8
Section 6			
Side wire sheaves	9.0	3.5	110.3
Suction piping	12.3	0.3	1.1
Ladder hoist connection	4.0	2	16.0
Total	25.3		127.4
Section 7			
Suction mouth correction	7.0	0.3	0.6
Ballast plates	20.0	1	20.0
Total	27.0		20.6

Table B.11: *Mass moment of inertia due to components.*

Appendix C

Model Updating

In section **??** measured vibrations are presented by first obtaining the magnitude of the fourier-transforms, and then adding them toghether. This approach has been followed as it gives the best visualization. During meetings it was discussed whether other approaches would yield better results. Two approaches where discussed, including first adding all complex results, and then taking the magnitude this is presented in section C.0.1. The other method was to use only one dataset this is presented in section C.0.2. By comparing results from chapter 5 and section C.0.2 it is noted that more clear behavior can be identified using the stacking method, than by using only one dataset or the other method. It should also be noted that in comparison to the FDD as used in chapter the results do show behavior that cannot be directly linked to the forced harmonic loading.

C.0.1 Motions stacked data including phase shift

In this section obtaining the transmissibility functions is performed slightly different than in chapter 5. fourier transforms are obtained from all motions. Next they are added together and the magnitude is obtained as in equation C.1.

$$\ddot{Z}_n(\omega) = \mid \sum_{d=1}^{22} \mathfrak{F}(\ddot{Z}_n(t))_d \mid \tag{C.1}$$

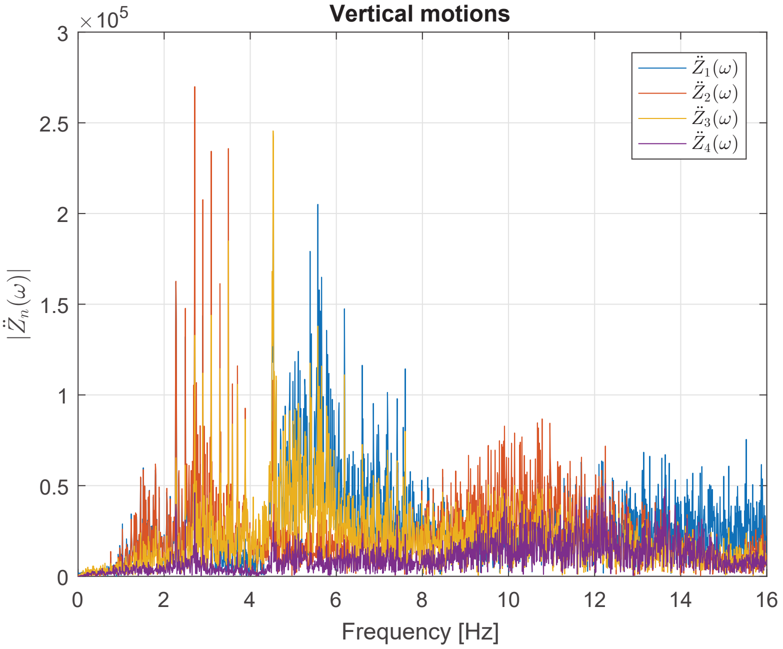

Figure C.1: *Four vertical motions obtained only for dataset 14 using equation 5.4*

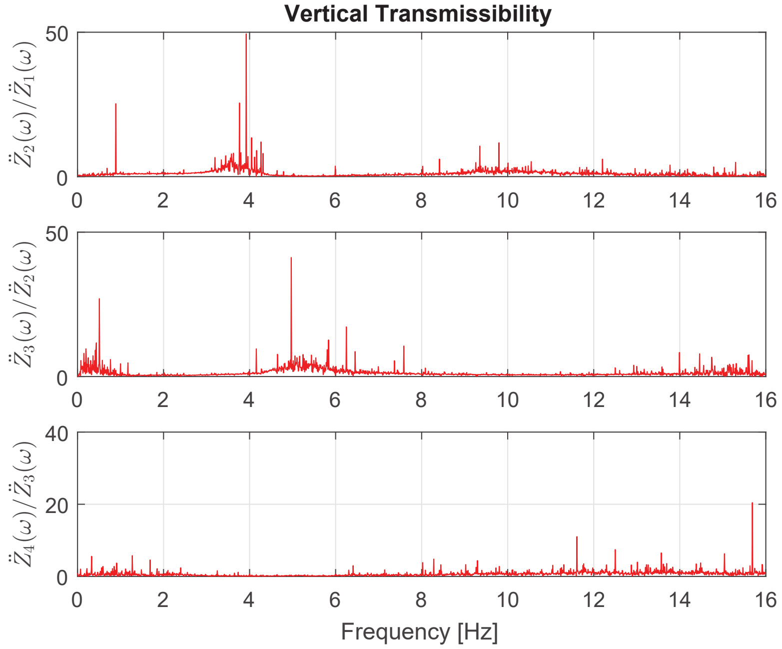

Figure C.2: *Transmissibility function in vertical direction for all datasets*

As shown in the results more clear behavior can be found with the method presented in chapter 5.

C.0.2 Motions and transmissibility function dataset 14

Besides the method mentoined above, it was also suggested to use only one dataset, in the figures below, this is shown for the vertical motion of dataset 14. As can be seen, the motions shows mainly the excitation peak at blade frequency. The transmissibility functions show spiky behavior, and can therefore be matched more difficult than with the proposed method from chapter 5.

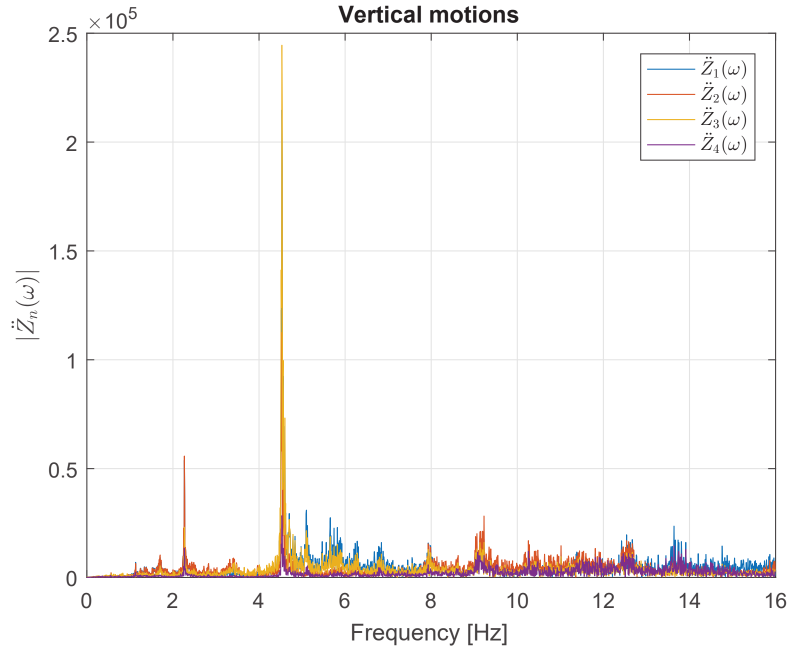

Figure C.3: *Four vertical motions as obtained using equation 5.4*

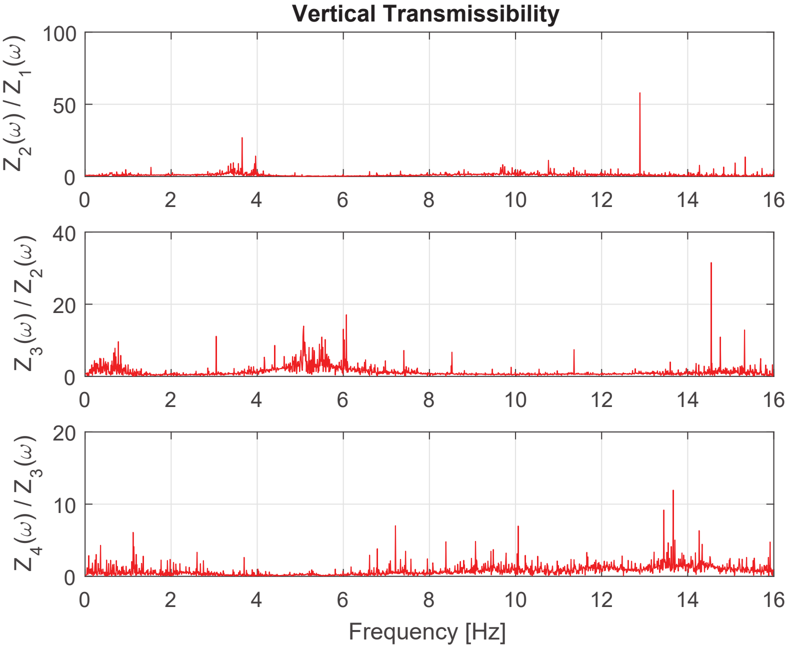

Figure C.4: *Four vertical motions as obtained using equation 5.4*

C.1 Water added mass calculation

In table C.1 the internal water added mass is determined based on the sectioning as given in figure 5.9. The factor F used in the table defines whether the shape of the section is rectangular or triangular. the water added mass is determined using equation C.2 where a water density of $\rho_w = 1025\,\frac{\mathrm{kg}}{\mathrm{m}^3}$ is used.

$$M_{wi} = FHLD\rho_w \tag{C.2}$$

Sect.	Vol nr.	$F[-]$	H[m]	L[m]	D[m]	Vol. [m^3]	Mass[mT]	Mass[mT]
1	1	0.5	1.6	3.785	6.7	41.4	42.4	42.4
2	2	1	1.6	3.2	6.7	34.8	35.6	49.6
2	3	0.5	1.2	3.2	6.7	13.6	13.9	
3	4	1	2.0	6.0	6.7	84.5	86.6	118.1
3	5	0.5	1.5	6.0	6.7	30.8	31.5	
4	6	1	2.7	7.5	6.7	141.0	144.6	165.5
4	7	0.5	0.8	7.5	6.7	20.5	21.0	
5	8	0.5	0.7	4.3	6.7	11.0	11.2	71.1
5	9	1	2.0	4.3	6.7	58.4	59.9	
6	10	0.5	2.0	4.2	5.6	23.6	24.2	24.2

Table C.1: *Determination of the water added*

Calculation of the water added mass due to the moving body is performed using [10] the reader is referred to this document for the full calculations and parameters used. The external water added mass is can be found in table C.2

Section	L [m]	L [m]	n_p	A [m^2]	b/a	C_A	V_r [m^3]	A_{ij} [mT]
1	3.8	6.7	1	25.5	1.78	0.73	75.9	56.8
2	3.2	6.7	1	21.4	2.12	0.76	53.6	41.7
3	6.0	6.7	1	40.7	1.12	0.62	192.9	122.6
4	7.5	6.7	2	101.4	0.90	0.65	299.5	399.1
5	4.3	6.7	2	57.7	1.58	0.78	97.0	155.1
6	4.2	5.6	2	46.6	1.33	0.7	76.6	109.9

Table C.2: *Table for calculating the water added mass using [10].*

Add water added mas
table for vertical moti

C.2 Mass distribution table

Node	m_x [kg]	m_y [kg]	m_z [kg]	J [kgm^2]	J_y [kgm^2]	J_z [kgm^2]
1	0	10603.04	38992.42	228600	0	0
2	0	35393.32	84645.33	501120	0	0
3	0	147755.88	166002.27	168584	0	0
4	0	317365.27	402682.04	13600	0	0
5	0	255487.09	395468.48	11813	0	0
6	0	73178.85	180194.75	127355	0	0
7	0	12091.42	67058.95	20630	0	0
8	0	30000	30000	0	0	0
9	0	0	0	28600	0	0

Table C.3: *Point masses added to the model, including water added mass and inertial component mass.*

C.3 Motion prediction method on dataset 14

The motion prediction method is also shown for only dataset 14, to show that it also predicts the behavior for one dataset. These figures are not presented within the report as this

C.4 Motion prediction method on the data as used in section 5.1

Initially results of the motion prediction method were presented for the data used in section 5.1 as this resulted in more clear behavior. However, as the data was used as an input to the model, it would not be accurate to exclude the phase shifts from the data. Results without the phase shift do show more clear behavior than the other approach, it has been chosen to include these in the Appendix, hence the figures below.

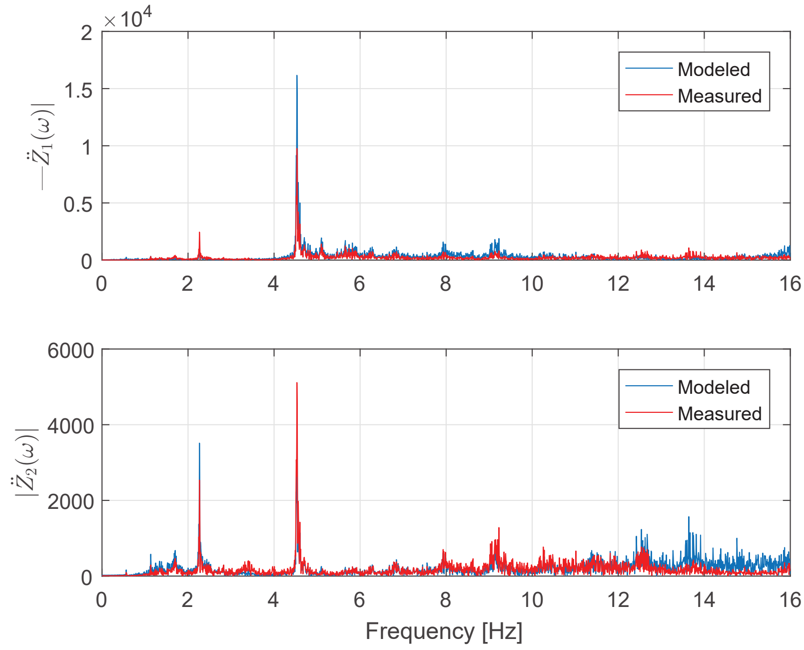

Figure C.5: *Results of the motion prediction method for dataset 14 in vertical direction.*

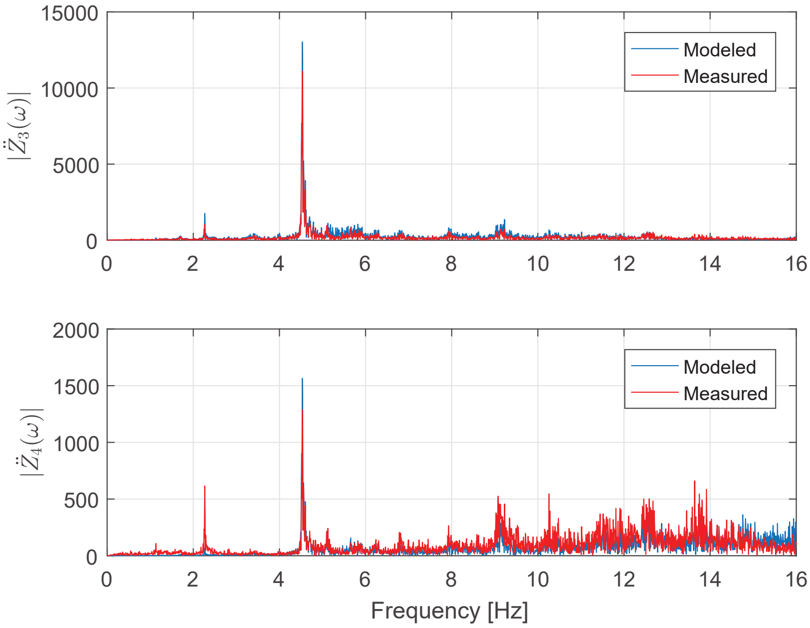

Figure C.6: *Results of the motion prediction method for dataset 14 in vertical direction.*

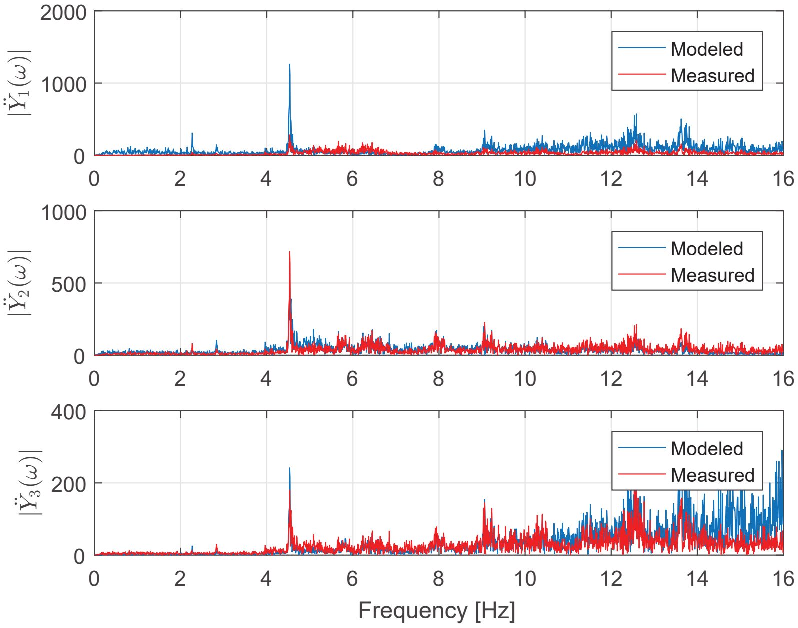

Figure C.7: *Results of the motion prediction method for dataset 14 in horizontal direction.*

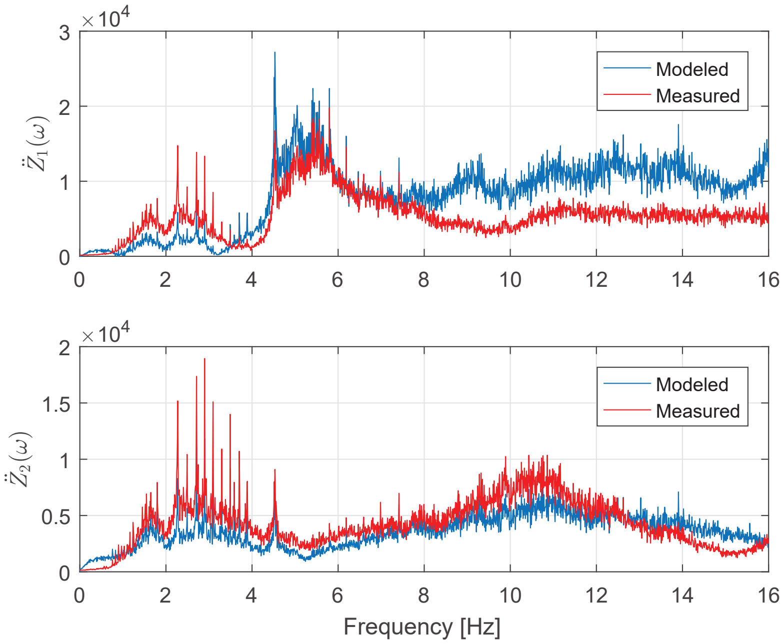

Figure C.8: *Motions in vertical direction $\ddot{Z}_1(\omega)$ and $\ddot{Z}_2(\omega)$*

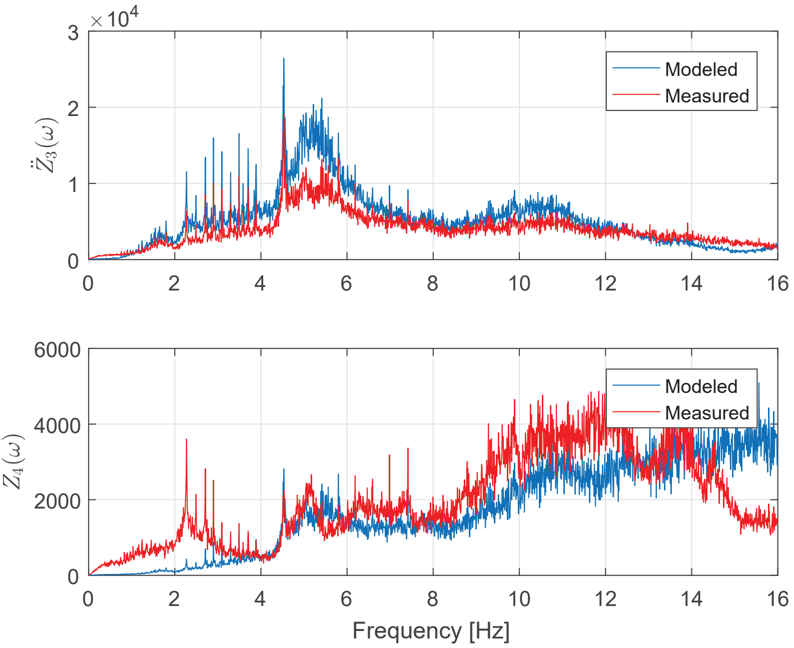

Figure C.9: *Motions in vertical direction* $\ddot{Z}_3(\omega)$ *and* $\ddot{Z}_4(\omega)$

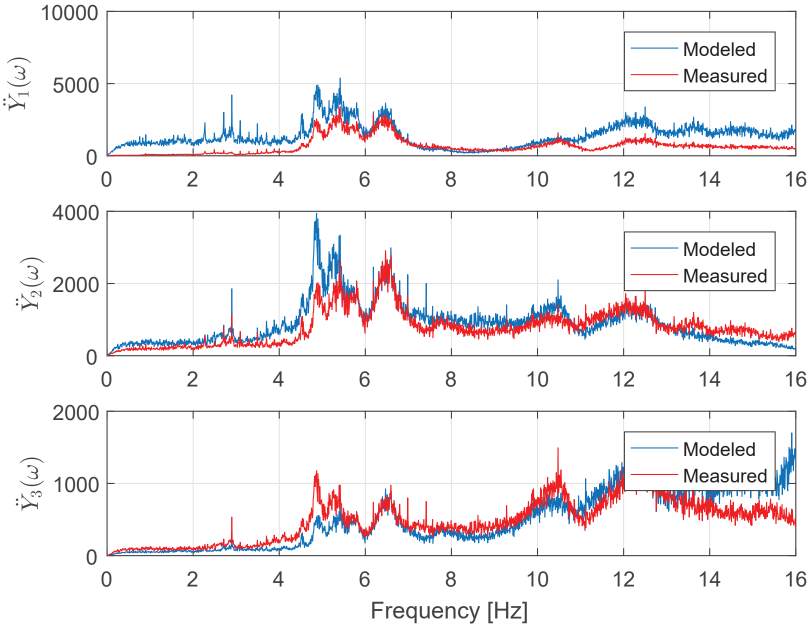

Figure C.10: *Motions in horizontal direction*

Appendix D

Cutter ladder damage

Figure D.1: *Picture of the damage to the bottom of cutter ladder, employee for scale*

(a) *Picture of the cracks in the gearbox foundation of the cutter ladder.*

(b) *Picture of the cracks in the thrust bearing foundation.*